

Search for exotic massive long-lived particles decaying semileptonically in the LHCb detector

THÈSE N° 6618 (2015)

PRÉSENTÉE LE 3 JUILLET 2015
À LA FACULTÉ DES SCIENCES DE BASE
LABORATOIRE DE PHYSIQUE DES HAUTES ÉNERGIES 1
PROGRAMME DOCTORAL EN PHYSIQUE

ÉCOLE POLYTECHNIQUE FÉDÉRALE DE LAUSANNE

POUR L'OBTENTION DU GRADE DE DOCTEUR ÈS SCIENCES

PAR

Bastien Luca MUSTER

acceptée sur proposition du jury:

Prof. V. Savona, président du jury
Prof. A. Bay, directeur de thèse
Dr W. Hulsbergen, rapporteur
Dr P. Koppenburg, rapporteur
Prof. M. Q. Tran, rapporteur



ÉCOLE POLYTECHNIQUE
FÉDÉRALE DE LAUSANNE

Suisse
2015

Acknowledgements

Dans un premier temps, je tiens à remercier chaleureusement le Professeur Aurelio Bay qui a dirigé ce travail. “Cher Aurelio, je te remercie pour ton soutien et la confiance que tu m’as accordée. Durant ces quatre années, j’ai eu beaucoup de plaisir à travailler dans ton équipe ! J’ai eu la chance d’apprendre énormément et d’évoluer dans un environnement de travail chaleureux et motivant grâce à toi !” J’aimerais ensuite remercier vivement Wouter Hulsbergen, Patrick Koppenburg et Minh Quang Tran qui m’ont fait l’honneur d’accepter d’être les rapporteurs de ce travail. Je remercie également le Professeur Vincenzo Savona pour avoir accepté de présider le jury de cette thèse.

J’aimerais dire un grand merci à mes amis et collègues Pierre Jatton, Julien Rouvinet et Chitsanu Khurewathanakul pour le plaisir que j’ai eu à travailler à leur côté. Je voudrais particulièrement remercier Julien qui, depuis le début de ma thèse, m’a apporté énormément, que ce soit au travail ou en dehors. “Merci Julien pour ton précieux soutien et ton amitié !” J’aimerais remercier également mon ami physicien-astrologue du 6ème étage, F. Rérat, avec qui j’ai eu la chance de faire toutes mes études, du gymnase au doctorat ! “Tu as été un ami inestimable durant toutes ces années !”

Je remercie chaleureusement Frédéric Blanc et Stéphane Tourneur avec qui j’ai toujours eu beaucoup de plaisir à échanger. Merci pour ces discussions qui m’ont constamment aidé à avancer dans mon travail et à trouver des solutions !

Je tiens à remercier toutes les personnes du laboratoire de physique des hautes énergies, avec une attention particulière aux secrétaires Esther Hoffmann et Erika Luthi pour leur disponibilité et la patience qu’elles ont eue avec mes compétences administratives ! Un grand merci à Tatsuya Nakada et Olivier Schneider qui m’ont permis de développer mon intérêt pour la physique des particules et qui ont guidé mon choix de faire un doctorat. Merci également à Minh Tâm Tran ! J’ai aimé assister tes cours et j’ai toujours apprécié nos discussions !

Un énorme merci à mes amis qui me sont chers et qui m’ont beaucoup soutenu et m’ont permis de me changer les idées ! Un grand merci particulier à Miguel, Amaury, Mike, Raph, David et Valentin ! Vous êtes les meilleurs !

Enfin, j’aimerais remercier mes parents et ma marraine pour leur incroyable soutien durant ces quatre années ! Je vous dois beaucoup ! Merci Maman de m’avoir inculqué un esprit scientifique grâce aux cahiers de vacances !

Lausanne, 15 Février 2015

B. M.

Abstract

Long-lived particles are predicted by numerous theories beyond the Standard Model. This thesis work is dedicated to the search for long-lived neutralinos decaying semileptonically into standard model particles. This decay channel is allowed by R-parity violation in the Minimal Supersymmetric Standard Model (MSSM) framework. A displaced vertex reconstructed with several tracks and an isolated high- p_T muon is the expected typical signature. This search is motivated by the ability of the LHCb detector to reconstruct displaced vertices and by the low p_T threshold of the muon trigger system that allow to study yet unexplored region of the theoretical parameter space. The analysis has been performed for neutralino masses between 38 and 198 GeV/ c^2 with a lifetime of 5, 10 and 50 ps on data collected from pp collisions at center-of-mass energy of $\sqrt{s} = 7$ TeV and 8 TeV during 2011 and 2012 at LHCb. The signal determination techniques has been validated with Z and W events with a topology similar to the signal.

No evidence of these long-lived states has been observed, and upper limits on production cross-sections have been set.

Key words: CERN, LHCb, Supersymmetry (SUSY), Displaced Vertices, Long-Lived Particles, Neutralinos, Physics beyond the Standard Model

Résumé

Les particules à long temps de vie sont prédites par un grand nombre de théories modélisant la physique au-delà du modèle standard des particules. Cette thèse est dédiée à l'étude de neutralinos à long temps de vie se désintégrant en particules du modèle standard dont le canal de désintégration semileptonique est permis par la violation de la parité R dans le cadre du modèle MSSM. Un vertex déplacé reconstruit à l'aide de plusieurs traces dont un muon isolé de haut p_T est la signature typique attendue. Cette recherche est motivée par la capacité du détecteur LHCb à reconstruire des vertex déplacés et par le seuil relativement bas en p_T du muon dans le système de déclenchement qui permet d'étudier des régions inexplorées dans l'espace des paramètres du modèle. Cette analyse a été effectuée pour des modèles avec des neutralinos de masses se situant entre 38 et 198 GeV/c² pour des temps de vie allant de 5 à 50 ps. Les données collectées à partir des collisions pp à une énergie dans le centre de masse de $\sqrt{s} = 7$ TeV et 8 TeV pour les années 2011 et 2012 ont été analysées. Deux techniques d'extraction du signal qui modélisent le bruit de fonds de nature Quantum chromodynamics (QCD) ont été utilisées et testées avec des modes de désintégration du Z et du W . Aucune évidence de ces états à long temps de vie n'a été observée. Des limites supérieures sur les sections efficaces de production entre 0.06 à 0.46 pb ont été posées pour une efficacité totale de sélection allant de 1.9 à 6.0 %.

Mots clefs : CERN, LHCb, SUSY, Vertex Déplacés, Particules à long temps de vie, Neutralinos, Physique au-delà du modèle standard

Contents

Acknowledgements	i
Abstract	iii
Résumé	v
List of figures	xi
List of tables	xix
Introduction	1
1 Theoretical Introduction	3
1.1 The Standard Model	3
1.2 Supersymmetry : A natural extension of the Standard Model	6
1.2.1 Minimal Supergravity (mSUGRA) with Lepton Number violation with bilinear R-parity violation	8
1.3 Status of Long-Lived Particles (LLP) searches at CMS and ATLAS	9
2 CERN and the LHCb experiment	11
2.1 CERN and the LHC	11
2.2 Overview of three experiments : ATLAS, CMS and ALICE	13
2.2.1 ATLAS	13
2.2.2 CMS	13
2.2.3 ALICE	14
2.3 The LHCb experiment	15
2.3.1 The Magnet	16
2.3.2 The tracking system	17
2.3.2.a The VERTex LOCator	17
2.3.2.b The Silicon Tracker (ST): The Tracker Turicensis and The Inner Tracker	19
2.3.2.c The Outer Tracker	20
2.3.2.d Track reconstruction	21
2.3.3 Ring Imaging CHerenkov RICH 1 and 2	22
2.3.4 Electromagnetic and Hadronic CALorimeters	24
	vii

2.3.5	Muon chambers	25
2.3.6	The trigger systems	25
2.3.7	LHCb Software	27
3	Search for long-lived particles decaying semileptonically	29
3.1	Events samples considered in this study	29
3.1.1	Signal samples	30
3.1.2	Background samples	31
3.1.2.a	Special $b\bar{b}$ production	32
3.2	Characteristics of the signal from Monte Carlo (MC) truth (generator-level studies)	33
3.3	Data selection	37
3.3.1	Trigger and Stripping algorithms	37
3.3.2	Preliminary event selection (preselection)	40
3.3.2.a	Muon preselection	40
3.3.2.b	The reconstruction of primary and secondary vertices	42
3.3.2.c	Displaced vertex preselection	43
3.3.3	Properties of the selected vertices, the matter veto	43
3.3.4	Situation after the preselection, background studies	47
3.3.5	Neural Network	57
3.4	Signal determination	61
3.4.1	LLP mass fit	61
3.4.1.a	Fit of Lepton Violation (LV) models to the 2011 and 2012 dataset	63
3.4.1.b	Fit method applied to W and Z decays	69
3.4.2	The ABCD method	76
3.4.2.a	Definition of boundaries and estimate of the correlation bias	78
3.4.2.b	Determination of the signal for the 2011 and 2012 datasets	80
3.4.2.c	Validation with $Z \rightarrow \mu\mu$ as a control channel	80
3.5	Detection efficiency and systematic effects	82
3.5.1	Muon reconstruction	83
3.5.1.a	Muon Trigger study by tag and probe	84
3.5.1.b	Muon identification efficiency	85
3.5.1.c	Muon track Reconstruction efficiency	86
3.5.1.d	Muon impact parameter	87
3.5.1.e	Muon transverse momentum	87
3.5.2	Displaced vertex reconstruction	89
3.5.2.a	Radial dependency	92
3.5.3	Neural Network Classifier	93
3.5.4	Muon isolation and LLP reconstructed mass	95
3.5.5	Beam line position	97
3.5.6	Luminosity	98
3.6	Upper limit on production cross-section	98
4	Conclusion and Perspectives	105

A Appendix	107
A.1 Results of the fitting procedure with W and Z events as signal events for 2012 data	107
A.2 Simultaneous fit parameters	108
A.3 Multilayer Perceptron response	110
A.4 Neural Network classifier polluted by signal events	112
A.5 Effects of the MLP on m_{LLP} and $1/Isolation$	114
A.6 Estimation of the effects from for each signal models and datasets	115
A.7 Test of the ABCD method with $b\bar{b}$ MC events at the intermediate selections stage	116
Bibliography	122
Acronyms	123
Curriculum Vitae	125

List of Figures

1.1	Standard Model elementary particles and fundamental interactions : the charges of the particles are specified in green and the spin in orange. The measured mass or the mass limit (in electron volt eV) of each particles are indicated (gluons and photons are massless). It has been found that neutrinos are massive by the measurement of the oscillation between its different flavor states [1].	4
1.2	Illustration of the three coupling matching at the Grand Unified Theory (GUT) scale : (left) Standard Model prediction, (right) Standard Model extended with the supersymmetry lead to a perfect match. α_1, α_2 and α_3 are respectively the strong, the electromagnetic and the weak couplings.	7
1.3	Particles spectrum of the different new sparticles generated in the MSSM.	8
1.4	Feynman diagram for the channel of interest. The long-lived particle ($\tau_{\tilde{\chi}_1^0}$) is decaying into a muon and a smuon which is decaying into two standard model quarks. A displaced vertex reconstructed with a high transverse momentum muon and several tracks (jets) is the typical signature.	9
1.5	Exclusion graph from a combination of ATLAS and CMS results for the decay $\tilde{\chi}_1^0 \rightarrow \mu q_i q_j$ [2]. Left: exclusion in the squark mass versus gluino mass plane for a fixed $\tilde{\chi}_1^0$ mass of 100 GeV/c ² . Right: exclusion in the squark mass versus $\tilde{\chi}_1^0$ mass plane for a fixed gluino mass of 2 TeV/c ² as well as the different "LV" (Lepton Violation) fully simulated signal models considered in this study.	10
2.1	The LHC with the four main experiments : ATLAS, CMS, LHCb and ALICE.	12
2.2	The LHC hadron injector complex.	12
2.3	The ATLAS detector.	13
2.4	The CMS detector.	14
2.5	The ALICE experiment.	15
2.6	The LHCb spectrometer in the non-bending plane with its different components. . . .	16
2.7	The LHCb dipole and its cooling system and power supplies in a transverse view. . . .	17
2.8	The VERtEx LOCator (VELO) dimensions represented in the plane (x,z) at y=0 illustrations of the open and closed position.	18
2.9	Geometry of the VELO sensors in ϕr and picture of sensors position on one of the two retractable halves.	18
2.10	The four detection layers (x-u-v-x) with illustrations of the silicon microstrips. . . .	19

List of Figures

2.11 Representation of the four boxes of an IT station build around the LHC beam pipe with its dimension in the (x, y) plane.	20
2.12 Representation of the tracking system composed of the TT and of the three IT stations (magenta) and of the OT (green) in addition with a picture of an OT station in the geometrical configuration "u".	21
2.13 Definition of the different types of tracks considered by the reconstruction algorithms together with the amplitude of the magnetic field B as a function of the z coordinate. The VELO and T tracks used as "seeds" for the tracks reconstruction software are located in regions with low magnetic field.	22
2.14 Left : Cherenkov angle for isolated tracks (Cherenkov ring does not overlap with others) as a function of the track momentum from the C_4F_{10} radiator. Right : Example of Cherenkov rings at LHCb. [3]	23
2.15 Representation of RICH1 and RICH2 with the different sets of mirrors and the HPD detecting the light emitted from particles passing through the medium (Aerogel, C_4F_{10} and CF_4).	23
2.16 Cells dimensions given for SPD/PS and Electromagnetic Calorimeter (ECAL) (left) and for Hadronic Calorimeter (HCAL) (right) presented on one quarter of the detector in the (x, y) plane.	24
2.17 Side view of the LHCb Muon Detector (left) with the different stations M1-M5. Each station is divided in four regions $R1 - R4$ (right) where the size of their logical pads are scaled by the ratio 1:2:4:8. [4]	25
2.18 Architecture of the LHCb trigger : scheme of the Level-0 trigger (left) and diagram of the three trigger stages with their corresponding reduction rate (right).	26
3.1 Pythia \hat{p}_T distribution for $b\bar{b}$ generation.	32
3.2 Cross-section times the fraction of events ϵ_{gen} with a muon of $p_T > 12$ GeV/c and a b-hadron in the LHCb enlarged geometrical acceptance $\eta \in [1.5, 5]$, as a function of the \hat{p}_T^{min}	33
3.3 Properties of the muon coming from the LLP. Top: transverse momentum of the muon in the LHCb acceptance. Bottom left: isolation variable of the muon. Bottom right: impact parameter of the muon with respect to the associated primary vertex.	34
3.4 Flight distance of the LLP for several masses (left) and different lifetime for LV38 (right).	35
3.5 Geometrical properties of the LLP decay vertex for several masses (left) and different lifetime for LV38 (right): Top: radial distance to the Z axis, bottom: Z decay position of the LLP.	35
3.6 Transverse momentum of the LLP (top). Mass of the LLP reconstructed with the stable charged daughters in the LHCb acceptance (bottom left). Number of stable charged daughters in the LHCb acceptance (bottom right).	36

3.7	Distributions of the muon variables for the 2011 dataset, compared to simulated $b\bar{b}$ and to the MC signal $LV38\ 10ps$, for events after trigger and stripping. Top left: Muon impact parameter with respect to the best primary vertex. Top right : $E(Ecal)/P^\mu + E(Hcal)/P^\mu$. Bottom left : Muon isolation. Bottom right : muon transverse momentum. The distributions are normalized to unity.	41
3.8	Like Figure 3.7, comparison between 2011 and 2012 data.	41
3.9	x and y positions of the reconstructed primary vertices obtained after the $R < 0.3\ mm$ cut for 2011 data.	43
3.10	From preselected 2011 data, the longitudinal (left plot) and radial (right plot) coordinates (lab frame) of the reconstructed secondary vertices with at least four forward tracks including the preselected muon, no backward tracks, and an invariant mass larger than $4.5\ GeV/c^2$ without Matter Veto (MV).	44
3.11	Like Figure 3.10, for preselected 2012 data.	44
3.12	Like Figure 3.10, position of the reconstructed vertices in coordinates (x,z) (lab frame). The data are presented by categorizing events kept after the MV procedure (in red) and events removed by the MV (in blue). Left: from the 2011 dataset. Right: from the 2012 dataset.	44
3.13	Distribution of $\ D_\phi\ $ in simulated events (black) and 2011 data selected for the displaced vertex analysis (red and blue). The vertical line corresponds to the cut applied in the analysis.	45
3.14	Like Figure 3.12 but for events selected after the MV procedure. Left: 2011 dataset. Right: 2012 dataset.	46
3.15	Distributions from 2011 data compared to simulated events, after preselection. Top left: muon transverse momentum Top right: the muon impact parameter with respect to the best primary vertex. Bottom left: the reconstructed mass of the displaced vertex computed with the outgoing tracks. Bottom right: muon isolation. The distribution are normalized to unity.	48
3.16	Distributions from 2011 data compared to simulated events, after preselection. Top left: the number of tracks that have been used to reconstruct the vertex including the muon. Top right: the radial distance R to the beam line of the reconstructed vertex. Bottom left: the longitudinal vertex fit error. Bottom right: the radial vertex fit error. The distribution are normalized to unity.	49
3.17	Same as Figure 3.15 but for the comparison of the 2011 and 2012 datasets. $LV38\ 10\ ps$ is also show for comparison.	53
3.18	Same as Figure 3.16 but for the comparison of the 2011 and 2012 datasets. $LV38\ 10\ ps$ is also show for comparison.	54
3.19	2011 data compared to simulated $b\bar{b}$ events after the requirement of a minimal distance R to the beam axis of $0.55\ mm$. Top left: muon transverse momentum. Top right: muon impact parameter with respect to the best primary vertex. Bottom left: reconstructed mass of the displaced vertex. Bottom right: muon isolation. The distribution are normalized to unity.	55

List of Figures

3.20	2011 data compared to simulated $b\bar{b}$ events after the requirement of a minimal distance R to the beam axis of 0.55 mm . Top left: number of tracks used to reconstruct the vertex including the muon. Top right: radial distance R to the beam line of reconstructed vertex. Bottom left: longitudinal vertex fit error. Bottom right: radial vertex fit error. The distribution are normalized to unity.	56
3.21	Input variables distributions of the multi-layer perceptron (Multilayer Perceptron (MLP)) neural network for the signal (LV38 ($\tau = 10\text{ ps}$)) and the background model (2011 data).	58
3.22	Distributions of the MLP input variables for the signal (LV38 ($\tau = 10\text{ ps}$)) and the background transformed into gaussian distributions after the decorrelation phase that take into account the linear correlation between each variables.	58
3.23	Linear correlation coefficient matrix for signal events (LV38 ($\tau = 10\text{ ps}$)) and background events computed by TMVA for the input and spectator variables. Note the low correlation between muon isolation and the LLP reconstructed mass.	59
3.24	Convergence and overtraining tests : (left) error on the estimator as a function of the number of epochs (cycles) and (right) MLP response distributions of the trained and test sample for signal (LV38 ($\tau = 10\text{ ps}$)) and background (2011 data).	59
3.25	Signal significance, signal efficiency and background rejection as a function of the MLP cut for LV38 ($\tau = 10\text{ ps}$).	60
3.26	Signal (LV38 ($\tau = 10\text{ ps}$)) efficiency as a function of the MLP response for different fraction of signal event added to the background model (2011 data) at the training stage.	60
3.27	Muon isolation for 2011 data compared to LV38 10 ps signal model after the MLP cut with the definition of the signal-free sideband region used to model the background LLP mass shape in the signal region.	61
3.28	Distribution from the 2011 dataset. In black the candidates from the signal region, in dashed blue from the sideband. The predicted LV38 10 ps distribution is in red. Top right: the LLP reconstructed mass. Bottom left: the transverse momentum of the muon. Bottom right: the muon impact parameter with respect to the best primary vertex. The distributions are normalized to unity.	62
3.29	Same as figure 3.28 for other variables. Top left: the number of tracks used to reconstruct the LLP. Top right: LLP radial distance R to the beam line. Bottom left and right: the longitudinal and the radial errors on the LLP vertex fit. The distributions are normalized to unity.	63
3.30	Fit results of the different signal model in the signal region with a single side <i>RooDecay</i> function ($\tau = 10\text{ ps}$) : LV38 (top), LV98 (bottom left) and LV198 (bottom right).	65
3.31	Results of the fit performed on 2011 data for LV38 10 ps . The results of the simultaneous fit in the sideband region (right) and in the signal region (left) are shown. The green dashed function is the background component. The blue curve represents the total function (background + signal) in the signal region.	65
3.32	Same as Figure 3.31 for the 2012 dataset.	66

3.33	Pull distribution of the number of extracted signal events for different number of injected of signal events injected for LV38 ($\tau = 10$ ps). μ_{pull} and σ_{pull} are the mean and the standard deviation of the gaussian fit. The pull distribution is defined as: $Pull = \frac{N_s^{fit} - N_s}{\sigma_{N_s^{fit}}}$.	69
3.34	LLP reconstructed mass versus the muon isolation. Top Left: 2011 data. Bottom left: $b\bar{b}$ simulated events. Top Right: W and Z MC events. Bottom Right: LV38 10ps signal events for comparison.	70
3.35	$W \rightarrow \mu\nu$ and $Z \rightarrow \mu\mu$ Monte Carlo sample mass fit for 2011 conditions. Left: $W \rightarrow \mu\nu$ mass fit with $F_W(m)$, in red and green the two exponential convoluted with the same gaussian resolution function. $\chi^2/nDoF = 1.6$. Right: $Z \rightarrow \mu\mu$ mass fit $F_Z(m)$, in red the Breit-Wigner function and in green the sum of the exponential and the Gaussian function. $\chi^2/nDoF = 2.2$.	71
3.36	Mass fit for the determination of the W and Z signal in the 2011 dataset. Left: the fit for candidates from the sideband region; in green and red the two exponential, in blue the total fitted function. Right: the fit for candidates from the signal region; in blue the total fitted function, in magenta, the W component modeled with $F_W(m)$, and, in green, the Z component modeled with $F_Z(m)$. The fit gives $\chi^2/nDoF = 1.8$.	72
3.37	Same as Figure 3.36. Top: fit of events with a positive charged preselected muon. $\chi^2/nDoF = 1.4$. Bottom: fit of events with a negative charged preselected muon. $\chi^2/nDoF = 2.3$.	73
3.38	Example of the significance values for 200 background events and 5 signal events as a function of the cuts on the LLP mass and the muon isolation. The significance is multiplied by a factor 100. The blue circle denotes the boundaries with the best significance.	77
3.39	Example of toy experiment with 200 background events (red) and 5 signal events based on LV38 ($\tau = 10$ ps) (blue boxes). A, B, and C are the sidebands used to estimate the background in D.	78
3.40	The A,B,C and D regions defined in the plane $(m_{LLP}, 1/Isolation)$. The 2011 data preselected events are plotted in red for masses of the LLP greater than 40 GeV/c ² . The contours are obtained from $Z \rightarrow \mu\mu$ simulated decays.	81
3.41	Left, transverse momentum of the probed muon and, right, dimuon mass for data and simulated events.	85
3.42	Trigger efficiency as a function of the muon transverse momentum determined by the tag and probe technique for data and simulated events.	85
3.43	Muon identification efficiency as a function of the muon transverse momentum determined by the tag and probe technique, for data and simulated events.	86
3.44	Left: muon impact parameter distribution in Monte Carlo and data for $Z \rightarrow \mu\mu$ events. Right: ratio Data/MC.	87
3.45	Data/MC ratio of the muon p_T distributions for $Z \rightarrow \mu\mu$ events.	88
3.46	Top, mass fit of B^0 exclusive candidates and, bottom, inclusive candidates reconstructed with the displaced vertex algorithm. At the left, the 2011 data, at right the simulation. In green, the exponential shape which models the combinatorial background. In red, the signal peak modelled by two gaussian. In blue, the total fitted function.	90

List of Figures

3.47	Like Figure 3.46, for the analysis of 2012 data.	90
3.48	Comparison of the vertex finding efficiency for data and simulated events, from the analysis of B^0 candidates as a function of η (top left), p_T (top right), R distance to the beam axis (bottom left) and the number of primary vertices (bottom right). A reweighting procedure is performed to match the signal kinematics.	91
3.49	Like Figure 3.48 for the 2012 data analysis.	91
3.50	Data/MC ratio of the vertex finding efficiency as a function of the distance to the beam axis. 2011 data at left, and 2012 data at right.	92
3.51	MC/data ratio of the reconstruction efficiency for kaon tracks reconstructed using the online (left plot) and offline (right plot) algorithms as a function of the radial distance R	92
3.52	Biases introduced at the testing stage of the MLP, corresponding to each input variables. 10000 toy experiments have been generated.	94
3.53	Difference between efficiency measured in the toy study and the efficiency obtained without any bias.	94
3.54	For each MLP input, the abscissa of the corresponding scatter plot is the difference between efficiency measured in the toy study with and without bias, for the bias factor given in the ordinate of the plot.	95
3.55	Left: Muon isolation distribution for 2011 data and $b\bar{b}$ simulated events. Right: ratio of the two distributions fitted by a constant.	96
3.56	Left: LLP reconstructed mass distribution for 2011 data and the special $b\bar{b}$ Monte-Carlo sample. Right: ratio of the two distributions with a constant fit.	97
3.57	Illustration of the first steps of the CL_s algorithm. In blue: the profile likelihood ratio for background only hypothesis ($\sigma = 0$). In red: the profile likelihood ratio for signal plus background hypothesis for a given value of σ . In black: the observed profile likelihood ratio. Each bins contain the results from pseudo-datasets generated from the background model.	100
3.58	Frequentist scan of the CL_s algorithm for 2011 data analysis, and the LV38 ($\tau = 10$ ps) signal model. cx refers to the production cross-section in pb	100
4.1	Graphs from models considered from the CMS results with the LV models studied in this analysis together with the region of the parameter space targeted by the the fast simulation.	106
A.1	Same as figure 3.37 for 2012 data.	107
A.2	Overtraining check of the MLP classifier for 2011 data and LV38 signal models together with the MLP response selection applied for the signal extraction techniques : $\tau = 5$ (left), 10 (center) and 50 ps (right).	110
A.3	Like Figure A.2 for LV98 models.	110
A.4	Like Figure A.2 for LV198 models.	110
A.5	Overtraining check of the MLP classifier for 2012 data and LV38 signal models together with the MLP response selection applied for the signal extraction techniques : $\tau = 5$ (left), 10 (center) and 50 ps (right).	110
A.6	Like Figure A.5 for LV98 models.	111

A.7	Like Figure A.5 for $LV198$ models.	111
A.8	Signal efficiency as a function of the MLP response selection for different fraction of signal events added to the background for 2011 data and $LV38$ signal models : $\tau = 5$ (left), 10 (center) and 50 ps (right).	112
A.9	Like Figure A.8 for $LV98$ models.	112
A.10	Like Figure A.8 for $LV198$ models.	112
A.11	Signal efficiency as a function of the MLP response selection for different fraction of signal events added to the background for 2012 data and $LV38$ signal models : $\tau = 5$ (left), 10 (center) and 50 ps (right).	112
A.12	Like Figure A.11 for $LV98$ models.	113
A.13	Like Figure A.11 for $LV198$ models.	113
A.14	Effect of NN_{cut} (MLP) on the bi-parametric distribution. The contour define 2011 data distribution in comparison with the signal $LV38$ ($\tau = 10$ ps) as an example (black dots).	114
A.15	Effect of NN_{cut} (MLP) on the distribution of the bi-parametric projections for 2011 data and $LV38$ ($\tau = 10$ ps) as an example . Inverse of the isolation (left) and reconstructed mass of the long-lived particle candidate (right).	114
A.16	Example of toy experiment with 200 background events (red) and 5 signal events based on $LV38$ ($\tau = 10$ ps) (blue boxes). Most of the signal is in the D regions. A, B, and C are the sidebands used to estimate the background in D.	117

List of Tables

3.1	Summary of data and full simulation MC (2011 and 2012) sets of events used in this study. $N(year)$ is the number of generated events with the simulations conditions for the given year. Mass units are in GeV/c^2 . The number of collisions per bunch in the beam settings of the full simulated samples is $\nu = 2$ for 2011 and $\nu = 2.5$ for 2012. The geometrical acceptance is defined as $1.5 \leq \eta_\mu \leq 5$	30
3.2	SUSY parameters of the models considered. The LLP of the LV model is the lightest super-partner, the neutralino : $\tilde{\chi}_1^0$. M1 and M2 are the Pythia parameters RMSS(1) and RMSS(2), $m_{\tilde{g}}$ is RMSS(3), μ is RMSS(4), $\tan\beta$ RMSS(5) and $m_{\tilde{q}}$ is RMSS(8-12). Samples with lifetime of 5,10 and 50 ps have been generated for each mass. The lifetime of the LLP is fixed by hand.	31
3.3	Generator efficiency, ϵ_{Gen} , (in percent) for events with at least one LLP and one muon in the LHCb acceptance at $\sqrt{s} = 7$ TeV (2011) and $\sqrt{s} = 8$ TeV (2012) of the different models and the corresponding lifetime.	31
3.4	Summary of the selection criteria applied on the muon at the Hlt1SingleMuonHighPTDecision, Hlt2SingleMuonHighPTDecision and StrippingLLP2MuXHighPTHHighIPMuonLine level.	37
3.5	Trigger and stripping efficiencies in percent for signal models with a mass of $38 \text{ GeV}/c^2$ at $\sqrt{s} = 7$ TeV. The uncertainties are statistical. Hlt1, Hlt2 and Stripping is referring to Hlt1SingleMuonHighPTDecision, Hlt2SingleMuonHighPTDecision and StrippingLLP2MuXHighPTHHighIPMuonLine.	37
3.6	Same as Table 3.5 for signal models with a mass of $98 \text{ GeV}/c^2$	38
3.7	Same as Table 3.5 for signal models with a mass of $198 \text{ GeV}/c^2$	38
3.8	Trigger and stripping efficiencies in percent for signal models with a mass of $38 \text{ GeV}/c^2$ at $\sqrt{s} = 8$ TeV. The uncertainties are statistical. Hlt1, Hlt2 and Stripping is referring to Hlt1SingleMuonHighPTDecision, Hlt2SingleMuonHighPTDecision and StrippingLLP2MuXHighPTHHighIPMuonLine.	38
3.9	Same as Table 3.8 for signal models with a mass of $98 \text{ GeV}/c^2$	38
3.10	Same as Table 3.8 for signal models with a mass of $198 \text{ GeV}/c^2$	39
3.11	Number of preselected events for each background MC sample, $\sqrt{s} = 7$ TeV, $\sqrt{s} = 8$ TeV, and the number of expected background events in 2011. The values for LV38 10 ps are also reported. The last line is for the 2012 dataset.	47
3.12	Fraction of events with more than one candidate.	47

List of Tables

3.13	Number of events after the radial cut ($R > 0.55 \text{ mm}$) in data and in the simulated sets, for 2011. The results from the 2012 dataset are also given.	50
3.14	Summary of the preselection criteria.	50
3.15	Summary of the selection efficiencies (in percent) at the the different stage of the analysis for model with a LV model with a neutralino mass of $38 \text{ GeV}/c^2$ at $\sqrt{s} = 7 \text{ TeV}$ (2011).	51
3.16	Summary of the selection efficiencies (in percent) at different stage of the analysis for signal models with a neutralino mass of $98 \text{ GeV}/c^2$ at $\sqrt{s} = 7 \text{ TeV}$ (2011).	51
3.17	Like 3.16, for a neutralino mass of $198 \text{ GeV}/c^2$ at $\sqrt{s} = 7 \text{ TeV}$ (2011).	51
3.18	Like 3.16, for a neutralino mass of $38 \text{ GeV}/c^2$ at $\sqrt{s} = 8 \text{ TeV}$ (2012).	52
3.19	Like 3.16, for a neutralino mass of $98 \text{ GeV}/c^2$ at $\sqrt{s} = 8 \text{ TeV}$ (2012).	52
3.20	Like 3.16, for a neutralino mass of $198 \text{ GeV}/c^2$ at $\sqrt{s} = 8 \text{ TeV}$ (2012).	52
3.21	Number of events selected at each selection stages, for the 2011 and 2012 datasets. . .	53
3.22	$\chi^2/nDoF$ between the distributions from the sideband and the signal region for each variable.	63
3.23	Fit parameters of the <i>RooDecay</i> function for the different signal model considered ($\tau = 10 \text{ ps}$, $\sqrt{s} = 7 \text{ TeV}$).	64
3.24	Parameters from fit performed on the 2011 data sample for LV38 10 ps . See formulas 3.2 and 3.2. N_{sig} and N_{bkg} represent the number of signal events and background events respectively.	66
3.25	Results of the fitting procedure for each model performed on 2011 data: MLP min is the threshold value on the Neural Network response, $N_{sideband}$ the number of events in the sideband region, N_{signal} the number of events in the signal region. $N_{sig,fit}$ and $N_{bkg,fit}$ are the fitted numbers of signal and background events in the signal region.	67
3.26	Like Table 3.25 for 2012 data ($\sqrt{s} = 8 \text{ TeV}$).	67
3.27	Number of signal events extracted from the fit of the Monte Carlo toy experiments for different models with a fixed lifetime of $\tau = 10 \text{ ps}$ and a number N_s of signal events. The number of background has been fixed to respectively 126, 88 and 114 for LV38, LV98 and LV198, as it is the case in the 2011 data analysis.	68
3.28	Parameters of the simultaneous fit procedure of 2011 data with W and Z decay channel playing the role of signal. Total denotes no distinction in the muons charge.	74
3.29	Optimized boundaries for the ABCD analysis of the 2011 (left table) and 2012 (right table) dataset. The MLP cut used is also indicated.	79
3.30	Results of 1000 toy experiments for LV38 10 ps signal events and 2011 data with the boundaries placed at $m_{LLP} = 16 \text{ GeV}/c^2$ and $Iso^{-1} = 0.9$, for 200 background and 5 signal events. "Total" defines the average of the sum of background and signal events in each region and "signal" correspond to the number of signal events. "2D" and "Proj" are referring to the toys based on the bi-parametric $PDF(m_{LLP}, 1/Isolation)$ and on the projections $PDF(m_{LLP}) \times PDF(1/Isolation)$, respectively. The uncertainties are the Root Mean Square (RMS).	79
3.31	Results of the ABCD method applied to the 2011 dataset, for each signal model. The number of estimated signal events \bar{S}_D is corrected for the correlation effects.	80

3.32	Same as Table 3.31 for the 2012 dataset.	80
3.33	From the ABCD method applied to the measurement of the number of Z events in the 2011 dataset. number of events in the four regions and estimates for the signal and background in D. The average number of W and Z decays predicted from the simulation have been subtracted from N_C	81
3.34	Contributions to the efficiency in percent at the different stages of the event selection at $\sqrt{s} = 7$ TeV. The range is for the LV models with lifetime of $\tau = 5, 10$ and 50 ps. . . .	82
3.35	Same as table 3.34 for $\sqrt{s} = 8$ TeV	82
3.36	Summary of the systematic uncertainties, in %, on the selection efficiency for the 2011 dataset analysis.	83
3.37	Same as table 3.36 for the analysis of the 2012 dataset.	83
3.38	Systematic contributions from the different step of the muon reconstruction efficiency.	84
3.39	Muon selections criteria for the tag and probe procedure.	85
3.40	Selections criteria for the determination of the muon identification efficiency.	86
3.41	Systematic contributions in percent associated to the impact parameter selection. . . .	87
3.42	Contribution to the systematic uncertainty in percent due to the MLP for the different signal models.	95
3.43	Systematic contributions in percent to the muon isolation selection for the different signal models computed by taking the difference in efficiencies induced by a cut variation of ± 0.1 for 2011 and 2012 analysis.	96
3.44	Systematic contributions in percent on signal efficiency in percent caused by the LLP reconstructed mass cut for the different signal model estimated by taking the difference in efficiency induced by a mass cut variation of $1 \text{ GeV}/c^2$	97
3.45	Systematic contributions on signal efficiency in percent caused by the beam line position by taking the difference in efficiency induced by a radial cut variation of $10 \mu\text{m}$	98
3.46	Detection efficiency and upper limit on the production cross-section, σ_{up} , from the 2011 dataset and for each signal model, computed from the LLP mass fit results. The uncertainties on the efficiency are statistical only.	101
3.47	Like table 3.46, for the 2012 dataset.	101
3.48	Detection efficiency and upper limits on the production cross-section, σ_{up} , from the 2011 dataset and for each signal model computed from the ABCD results. The errors on the efficiency are statistical only.	102
3.49	Like table 3.48 for the 2012 dataset	103
A.1	Fit parameters of the signal and background model for the analysis of 2011 data and LV38 models together with the $\chi^2/nDoF$	108
A.2	Same as Table A.1 for LV98 models.	108
A.3	Same as Table A.1 for LV198 models.	108
A.4	Fit parameters of the signal and background model for the analysis of 2012 data and LV38 models together with the $\chi^2/nDoF$	109
A.5	Same as Table A.4 for LV98 models.	109

List of Tables

A.6	Same as Table A.4 for $LV198$ models.	109
A.7	Results of 1000 toy experiments for the 2011 dataset. 200 events of background and 5 events of signal has been generated in the bi-parametric distributions and its projections. "Total" defines the average of the background plus signal events in each region, "signal" correspond to the average of the number of signal events.	115
A.8	Same as table A.7 for the 2012 dataset.	116
A.9	Results of 1000 toy experiments for MC events and 2011 data with $m_{LLP} = 12.5 \text{ GeV}/c^2$ and $Iso^{-1} = 0.9$ for 200 events of background and 5 events of signal. "Total" defines the mean of the sum of background and signal events in each region and "signal" correspond to the mean of the number of signal only. "2D" and "Proj" are referring to the toys based on the bi-parametric $PDF(m_{LLP}, 1/Isolation)$ and the two projections $PDF(m_{LLP}) \times PDF(1/Isolation)$ respectively. The errors are RMS.	118

Introduction

Supersymmetry (SUSY) is one of the most popular extension of the Standard Model of particle physics (SM). It helps solving the hierarchy problem, unifying the gauge couplings at the Planck scale in addition SUSY has dark matter candidates. Some of the SUSY models predict the existence of exotic long-lived particles which could decay and be measured in the LHCb experiment. In this analysis we focus on the search for massive long-lived particles (LLP) decaying semi-leptonically to Standard Model particles via R-parity violation (R-parity violation (RPV)) in the mSUGRA framework. A displaced vertex reconstructed from several charged particles along with a well isolated high- p_T muon is the studied signature. This study performed with the LHCb experiment is motivated by the high precision of the vertex reconstruction provided by the VERtex LOCator (VELO) which allows to observe particles with a macroscopic distance of flight and by the low p_T threshold of the muon trigger. Despite its reduced geometrical acceptance, these properties of the LHCb detector allow to be competitive with similar analyses performed by ATLAS and CMS and even explore regions of the parameter space where these two experiments are limited by their low efficiency to reconstruct highly boosted light LLPs.

The aim of this analysis is to set upper limits on the production cross-section for a specific region of the parameter space of mSUGRA with RPV.

The main sources of background are $b\bar{b}$ events and muons originating from Z or W decays combined with other tracks close to the interaction points which are easily removed by asking for a minimal displacement inside the VELO. Displaced vertices reconstructed with muons from Z and W bosons have been exploited to validate two data-driven analysis methods.

This study extends the direct search of new physics at LHCb. Two studies are dedicated to the search for long-lived particles decaying hadronically with R-parity violation in mSUGRA and in Hidden Valleys models : a search for single exotic massive long-lived particles is presented in [5] and a search for Higgs-like bosons decaying into a pair of exotic particles is described in [6]. In the context of Minimal Gauge-Mediated Supersymmetry Breaking (mGMSB), a direct search for long-lived staus pair production has been presented in [7].

1 Theoretical Introduction

1.1 The Standard Model

The Standard Model (Standard Model (SM)) is a relativistic quantum field theory which describes the fundamental interactions and the known elementary particles. This gauge theory is based on the $SU(3)_c \otimes SU(2)_L \otimes U(1)_Y$ non-abelian symmetry group which brings together the forces present in Nature with the exception of the gravitational force described by General Relativity [8, 9, 10]:

- The $SU(3)_c$ group constructed from the quantum chromodynamics (QCD) describes the strong nuclear interactions between the color charged particles: the quarks. This force is carried by 8 massless gauge bosons: the gluons g .
- The electro-weak interaction regroups the electromagnetic force between the charged particles mediated by the photons γ and the weak nuclear force carried by the Z^0 and $W^{+/-}$ bosons and is based on the $SU(2)_L \otimes U(1)_Y$ group. The weak force is responsible for the decay processes which follow from the flavor changing and mixing between the different families of fermions described by the CKM (Cabibbo-Kobayashi-Maskawa) matrix [11] [12].

The gauge bosons of spin 0, 1 and 2 follow the Bose-Einstein statistics while the fermions of spin 1/2 obey to the Fermi-Dirac statistics. The Standard Model includes 12 fermions:

- 3 families of pairs of quarks: u (up), d (down); c (charm), s (strange); t (top) and b (bottom),
- 3 families of couples of leptons: electron (e^-), electron neutrino (ν_e); muon (μ^-), muon neutrino (ν_μ); tau (τ^-), tau neutrino (ν_τ),

Due to the properties of the strong interaction, the quarks are presents in nature in bound states as baryons (made of three quarks as for the proton) or mesons (made of a quark and an

Chapter 1. Theoretical Introduction

antiquark as for the pion) while the leptons are observed as free states. Each fermion has a corresponding anti-particle.

The Standard Model of particles and the three fundamental interactions are illustrated on Figure 1.1. The masses of the electro-weak bosons (the Z^0 and $W^{+/-}$) are generated by the mechanism of spontaneous electro-weak symmetry breaking (Electro-Weak Symmetry Breaking (EWSB)) induced by the Higgs field [13]. This mechanism is also responsible for the generation of the lepton masses. A potential candidate for the Higgs boson has been discovered in July 2012 by the ATLAS and CMS collaborations at CERN [14]. At present, all studies suggest that this candidate is compatible with the Higgs boson predicted by the Standard Model.

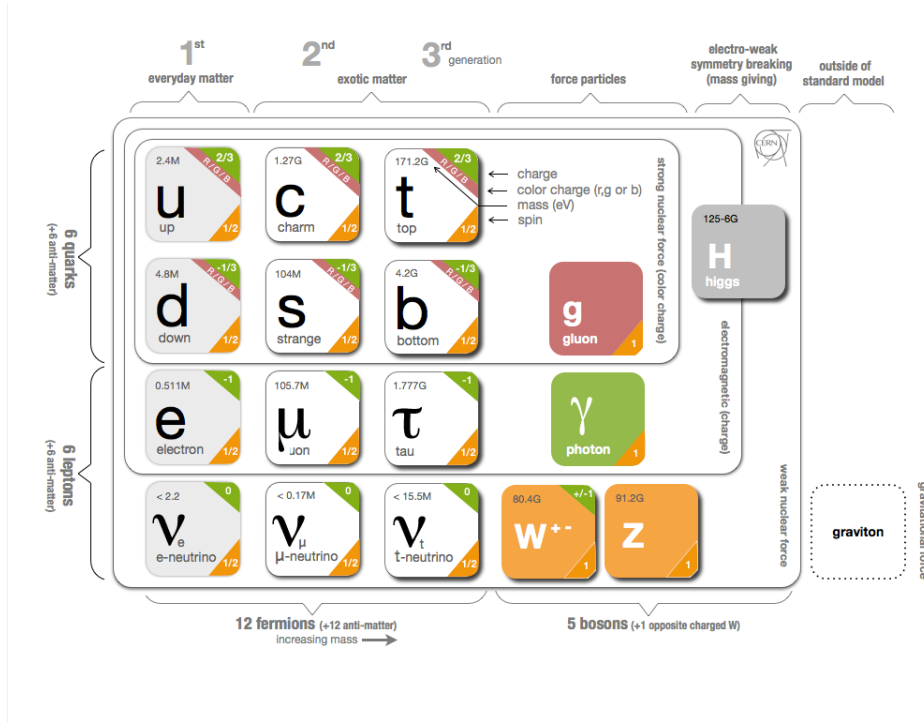


Figure 1.1: Standard Model elementary particles and fundamental interactions : the charges of the particles are specified in green and the spin in orange. The measured mass or the mass limit (in electron volt eV) of each particles are indicated (gluons and photons are massless). It has been found that neutrinos are massive by the measurement of the oscillation between its different flavor states [1].

The Standard Model is not a complete theory although all the observations are so far consistent with the model. Nevertheless SM leaves several problems unsolved:

- There exists no complete quantum fields theory that incorporates General Relativity in the Standard Model. Gravity is the weakest force in Nature (32 orders of magnitude weaker than the weak nuclear force) and is extremely difficult to test at the quantum level in particle experiments. Furthermore, the Standard Model does not provide answers to physical observations of phenomena dominated by the gravity as black holes or

gravitational waves and does not describe Nature just after the Big-Bang in particular the inflation phase of the early Universe. A Higgs-like boson could be the "inflaton" which is needed to clarify this question. The supergravity (mSUGRA) models introduced in section 1.2.1 are field theories combining Supersymmetry and General Relativity and could provide some answers to these unsolved problems of cosmological origin.

- The several orders of magnitude between the particles masses and the coupling constants of the different forces are known as the hierarchy problem [15]. Why is the weak force 32 order of magnitude stronger than gravity ? Why is the Planck scale 16 orders of magnitudes above the weak scale ? Why is the Higgs bosons mass much lower than the Planck scale despite the large quantum corrections requiring to adjust the parameters of the model very precisely to be consistent with observations ? The high-level of fine-tuning of the 25 Standard Model free parameters makes the theory "unnatural". The supersymmetry (SUSY) theory presented in section 1.2 offers solution to the hierarchy problem as well.
- Many astrophysical observations as the measurement of the spiral galaxy rotation curves, the fluctuations in the cosmic microwave background, the gravitational lensing of galaxy clusters or the behaviour of the large scale structure in the Universe have highlighted the existence of a matter interacting with the "luminous" matter by gravitational force only [16]. Cosmological considerations lead to an abundance of about 27% of this so-called dark-matter in the Universe for less than 5% of Standard Model particles. Several experiments are in progress to detect directly or indirectly dark-matter candidates. SUSY theories provide some of these potential dark-matter candidates.
- The Charge Parity violation (known as Charge Parity (CP) violation) sources of the SM are too small to explain the matter-antimatter asymmetry presents in the Universe. Moreover no CP violation have been observed so far in the QCD sector while nothing constraints the strong nuclear interaction to be CP invariant [17].
- The dark energy ($\sim 68\%$ of the universe composition) which induces the accelerated expansion of the Universe is not included in the SM [18].

1.2 Supersymmetry : A natural extension of the Standard Model

Supersymmetry (SUSY) is a space-time symmetry of quantum field theory that relates fermions to bosons. A brief overview of SUSY properties and consequences are presented in this section, a detailed introduction can be found in [19]. This theory based on the super-Poincaré algebra is one of the most popular extension of the Standard Model. A new generator Q is introduced with the following action:

$$Q|Fermion\rangle = |Boson\rangle$$

and vice-versa. In other words, it relates half-integer spin particles with integer spin particles. The resulting associated particles of this transformation are called superpartners and have the same physical properties as mass and quantum numbers except for the spin which differs from a half integer. Each particle from the same supermultiplet has at least one superpartner which is called with the prefix "s" for spin-0 partners (selectron, smuon, squark,...) and with the suffix "ino" for spin- $\frac{1}{2}$ partners (gluino, higgsino, zino,...). SUSY is not an exact symmetry of Nature otherwise the particles and their sparticles are degenerated in mass and should have been observed at a low energy scale. Thus, if Nature obeys to this framework, supersymmetry should be broken. This theory provides solutions to the main unsolved problems of the Standard Model:

- Adding superpartners to the quarks and leptons cancels the contributions of their scalar couplings with the Higgs and then stabilizes the Higgs mass at tree level. Therefore, the hierarchy problem can be solved and the Higgs mass becomes "natural". In general, in a SUSY theory, the radiative corrections are partially canceled.
- The supersymmetric extension of the SM spectrum leads to a perfect matching between the three gauge coupling and unifies the three fundamental interactions at the mass scale $M_{GUT} \sim 10^{16}$ GeV. This Grand Unified Theory (GUT) is illustrated in Figure 1.2.
- In several SUSY models, the lightest superpartner (Lightest Superpartner (LSP)) is a dark matter candidate. This so-called "neutralino" is the eigenstate of the linear superposition of the SUSY partners of the neutral Higgs and the gauge bosons:

$$\chi_i = \alpha_{i1} \tilde{B}^0 + \alpha_{i2} \tilde{W}^0 + \alpha_{i3} \tilde{H}_u^0 + \alpha_{i4} \tilde{H}_d^0$$

However, in the model considered for this thesis work, the neutralino is not a dark matter candidate because it has a too short lifetime and decays into Standard Model particles.

1.2. Supersymmetry : A natural extension of the Standard Model

The minimal supersymmetric extension of the Standard Model is called the MSSM. Two Higgs doublet fields are simply added to the different superpartners. The different MSSM fields are illustrated on Figure 1.3. The charged and the neutral doublets of the Higgs field are needed for the consistency of the theory. As the mass eigenstates are not necessarily the gauge eigenstates, several mixing states are expected. In particular, the \tilde{B}^0 and the \tilde{W}^0 mix to form the \tilde{Z}^0 and the $\tilde{\gamma}$ after the electro-weak symmetry breaking. The baryon number and lepton number conservation implies that the MSSM is at least approximately invariant under the R-parity defined as follow:

$$R_p = (-1)^{3(B-L)+2S}$$

where B and L are respectively the baryon and lepton numbers and S the spin.

Several versions of the MSSM and SUSY models exist. This thesis work is based on the framework of the minimal Supergravity (mSUGRA), a constrained MSSM model with R-parity violation which allows lepton and baryon numbers violation [20], [21]. The stability of the proton is then provided by other *ad hoc* symmetries in the Lagrangian. This is motivated by the fact that as the C and CP violation, the lepton number and the baryon number violation are necessary conditions for a viable baryogenesis [22]. The next sections are dedicated to the presentation of this model.

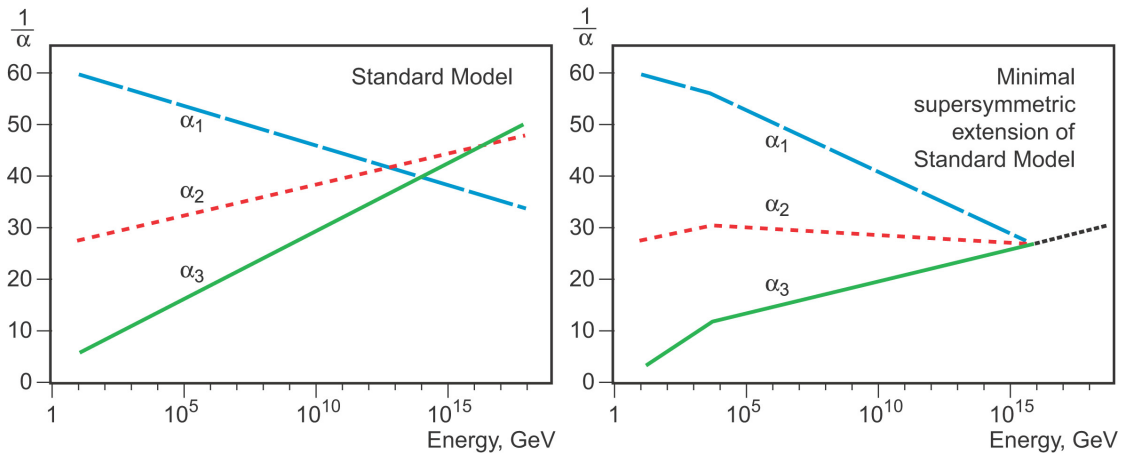


Figure 1.2: Illustration of the three coupling matching at the GUT scale : (left) Standard Model prediction, (right) Standard Model extended with the supersymmetry lead to a perfect match. α_1 , α_2 and α_3 are respectively the strong, the electromagnetic and the weak couplings.

Names	Spin	P_R	Gauge Eigenstates	Mass Eigenstates
Higgs bosons	0	+1	$H_u^0 \ H_d^0 \ H_u^+ \ H_d^-$	$h^0 \ H^0 \ A^0 \ H^\pm$
squarks	0	-1	$\tilde{u}_L \ \tilde{u}_R \ \tilde{d}_L \ \tilde{d}_R$	(same)
			$\tilde{s}_L \ \tilde{s}_R \ \tilde{c}_L \ \tilde{c}_R$	(same)
			$\tilde{t}_L \ \tilde{t}_R \ \tilde{b}_L \ \tilde{b}_R$	$\tilde{t}_1 \ \tilde{t}_2 \ \tilde{b}_1 \ \tilde{b}_2$
sleptons	0	-1	$\tilde{e}_L \ \tilde{e}_R \ \tilde{\nu}_e$	(same)
			$\tilde{\mu}_L \ \tilde{\mu}_R \ \tilde{\nu}_\mu$	(same)
			$\tilde{\tau}_L \ \tilde{\tau}_R \ \tilde{\nu}_\tau$	$\tilde{\tau}_1 \ \tilde{\tau}_2 \ \tilde{\nu}_\tau$
neutralinos	1/2	-1	$\tilde{B}^0 \ \tilde{W}^0 \ \tilde{H}_u^0 \ \tilde{H}_d^0$	$\tilde{N}_1 \ \tilde{N}_2 \ \tilde{N}_3 \ \tilde{N}_4$
charginos	1/2	-1	$\tilde{W}^\pm \ \tilde{H}_u^\pm \ \tilde{H}_d^\pm$	$\tilde{C}_1^\pm \ \tilde{C}_2^\pm$
gluino	1/2	-1	\tilde{g}	(same)
goldstino (gravitino)	1/2 (3/2)	-1	\tilde{G}	(same)

Figure 1.3: Particles spectrum of the different new sparticles generated in the MSSM.

1.2.1 mSUGRA with Lepton Number violation with bilinear R-parity violation

The mSUGRA (minimal Super GRAvity) is a restricted framework of the MSSM which is reducing the 124 SUSY free parameters to only 5:

$$m_0, m_{1/2}, A_0, \tan(\beta), \text{sign}(\mu);$$

where m_0 and $m_{1/2}$ are respectively the gaugino mass and the scalar soft SUSY breaking masses at the unification scale, A_0 is the universal trilinear term at the GUT scale and $\tan(\beta), \text{sign}(\mu)$ are the ratio of the two vacuum expectation values and μ the Higgs mixing parameter. This extended theory combines General Relativity and the principle of Supersymmetry which requires the existence of a graviton field of spin 3/2. In this model, gravity mediates the breaking of SUSY through a hidden sector at the GUT scale. A theoretical description of this model can be found in [23].

The stability of the proton and the lightest supersymmetric particle (the neutralino) are provided by the R-parity conservation in the MSSM. In mSUGRA, the neutralino is no longer stable, violating the lepton or the baryon conserving part of the super potential by the following terms:

$$W \supset \underbrace{\mu_i L_i H_u + \lambda_{ijk} L_i L_j E_k + \lambda'_{ijk} L_i Q_j D_k}_{\text{Violate L Number}} + \underbrace{\lambda''_{ijk} U_i D_j D_k}_{\text{Violate B Number}}$$

where L is the lepton doublet, H the Higgs doublet, E the lepton singlet, Q the quark doublet, D the down quark singlet, U the up quark singlet and $\Lambda \in (\lambda_{ijk}, \lambda'_{ijk}, \lambda''_{ijk})$ the trilinear coupling constants. The indices ijk denote the sum over the three fermion generations.

This R-parity violation (RPV) allows the neutralino to decay into visible standard model particles and generates the observed neutrino mass mixing. To prevent the proton decay, either the lepton number or the baryon number can be violated, but not both. A theoretical scenario of RPV is the bilinear R-parity violation (BRPV) which predict long-lived particles [24]. In the lepton number violation framework, the neutralino ($\tilde{\chi}_1^0$) may decay leptonically or semileptonically. The second being the case studied in this work [25, 2]:

$$\tilde{\chi}_1^0 \rightarrow \mu q_i q_j$$

The neutralino from squark-pair production ($pp \rightarrow \tilde{q}\tilde{q}(\tilde{q} \rightarrow q\tilde{\chi}_1^0)$) decays into two jets and an isolated muon as depicted in Figure 1.4. The decay time of the $\tilde{\chi}_1^0$ is fixed by the lepton number violating coupling (λ'_{ijk}). In this study, it has been tuned to obtain neutralino lifetimes of the order of 10 ps for a decay well inside the VELO. The topology of the decay and therefore the detection efficiency depends on the neutralino mass and lifetime, and the squark masses. Here $\tilde{\chi}_1^0$ with lifetime ($\tau_{\tilde{\chi}_1^0}$) from 5 to 50 ps and masses from 38 up to 198 GeV/c^2 have been considered. The gluino mass is fixed at 2 TeV/c^2 and squark masses at $m_{\tilde{q}} = 1.3$ TeV/c^2 . These parameters have been chosen to cover a so far unexplored region of the theoretical parameter space, as discussed in the next section.

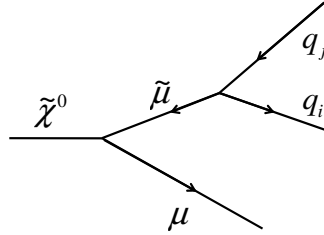


Figure 1.4: Feynman diagram for the channel of interest. The long-lived particle ($\tau_{\tilde{\chi}_1^0}$) is decaying into a muon and a smuon which is decaying into two standard model quarks. A displaced vertex reconstructed with a high transverse momentum muon and several tracks (jets) is the typical signature.

1.3 Status of LLP searches at CMS and ATLAS

Several analyses are dedicated to the search of new physics signatures of the SUSY type. In this section, the last results of CMS and ATLAS constraining the benchmark model considered in this analysis are summarized.

ATLAS has performed a search for long-lived particles in final states with a muon and a multi-track displaced vertex [26]. The collaboration has studied the sets of neutralino and squark masses of $494(m_{\tilde{q}} = 700 \text{ GeV}/c^2)$, $108 \text{ GeV}/c^2(m_{\tilde{q}} = 700 \text{ GeV}/c^2)$ and $108 \text{ GeV}/c^2(m_{\tilde{q}} = 1000 \text{ GeV}/c^2)$ for lifetimes of $1 < c\tau < 1000 \text{ mm}$. The dataset collected in 2012 at $\sqrt{s} = 8 \text{ TeV}$ corresponds to an integrated luminosity of 20.3 fb^{-1} . In the ATLAS experiment, the muons have a transverse momentum greater than $50 \text{ GeV}/c$ which limits the lowest neutralino mass. The CMS collaboration has performed a search for heavy resonances decaying to two long-lived massive neutral particles decaying to leptons: $H^0 \rightarrow XX(X \rightarrow l^+ l^-)$ [27]. H^0 masses of 125 to $1000 \text{ GeV}/c^2$ and X bosons masses of 20 to $350 \text{ GeV}/c^2$ with a decay length of about 20 cm in the laboratory frame have been explored. The $D0$ collaboration has made a search for neutral long-lived particles decaying into two muons in pp collisions at $\sqrt{s} = 1.96 \text{ TeV}$ [28]. They have studied neutrino masses of 3 to $40 \text{ GeV}/c^2$ for a lifetime of 40 ps .

The results of CMS and ATLAS have been combined in [2] to constrain the SUSY parameters for several models. The paper claims that long-lived particles decaying into charged lepton and quarks are only weakly constrained by the existing searches. In particular, the analyses performed by ATLAS and CMS have a very low efficiency to high boosted long-lived particles with a neutralinos mass below $150 \text{ GeV}/c^2$. Indeed, in addition to the small transverse momentum of the muon, the jets and the muons tend to merge for very low mass neutralino. On Figure 1.5, the exclusion graphs shows a quite large unexplored region for light neutralinos. In the plot we also indicate the 3 signal models used in this study.

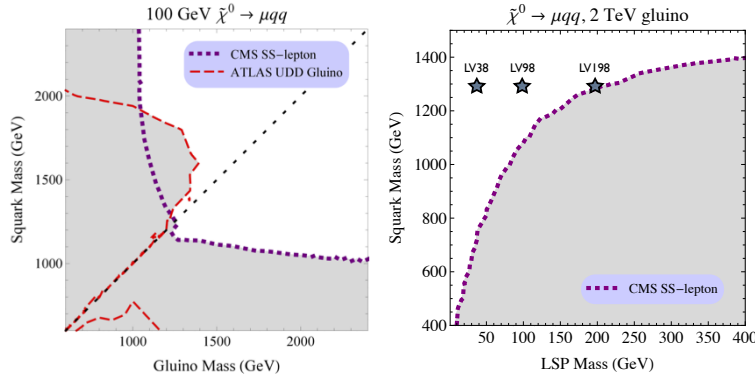


Figure 1.5: Exclusion graph from a combination of ATLAS and CMS results for the decay $\tilde{\chi}_1^0 \rightarrow \mu q_i q_j$ [2]. Left: exclusion in the squark mass versus gluino mass plane for a fixed $\tilde{\chi}_1^0$ mass of $100 \text{ GeV}/c^2$. Right: exclusion in the squark mass versus $\tilde{\chi}_1^0$ mass plane for a fixed gluino mass of $2 \text{ TeV}/c^2$ as well as the different "LV" (Lepton Violation) fully simulated signal models considered in this study.

2 CERN and the LHCb experiment

This chapter aims to present the CERN, the Large Hadron Collider (LHC) and the four main experiments. The description on the LHCb experiment is given in Section 2.3 in more details.

2.1 CERN and the LHC

The European Organization for Nuclear Research (CERN) is an organization based in Geneva and founded in 1954. CERN is dedicated to the exploration of the fundamental constituents of matter and to the improvement of our understanding of the physical laws that govern our Universe. 608 universities and 113 nationalities are represented at CERN. This organization has achieved a lot of scientific discoveries in the last 60 years thanks to many experiments made by the collaborations of many scientists. Two of the most important contributions were the discoveries of the electroweak bosons (W and Z) in 1983 and more recently, in 2012, the measurement of a new boson consistent with the predicted Standard Model Higgs boson [29] [30] [14]. The ever-increasing needs in computing resources for the different research helped to develop pioneering computational methods as the Internet technology and several grid computing projects.

The Large Hadron Collider (LHC) is a circular proton-proton synchrotron of 27 *km* of circumference built to a mean depth of 100 m under the Swiss-French border. It has been designed to reach an energy of 7 TeV corresponding to a center of mass energy of $\sqrt{s} = 14$ TeV for a luminosity of $1 \times 10^{34} \text{ cm}^{-2} \text{ s}^{-1}$. The energy reached in the center of mass was 7 TeV in 2011 and 8 TeV in 2012. The maximal speed of the protons in the LHC is 0.999999991 the speed of light (Lorentz factor of ~ 7500) which corresponds to 11000 revolutions per second. The protons beams each consists of 2808 bunches with about 1.15×10^{11} protons which leads to a bunch collision rate of 40 *MHz* [31]. Four interactions points are located along the ring. Four of them are exploited by the following experiments:

- The four main detectors: ATLAS, CMS, LHCb and ALICE,
- TOTEM: a telescope evaluating with precision the LHC luminosity and measuring elastic

Chapter 2. CERN and the LHCb experiment

and diffractive cross sections of particles emitted close to the interaction point of CMS [32],

- LHCf: studies forward emitted particles to simulate cosmic rays effects in matter close to the interaction point of ATLAS [33],



Figure 2.1: The LHC with the four main experiments : ATLAS, CMS, LHCb and ALICE.

The acceleration is performed in several steps. First, a linear accelerator (Linac2) injects protons of 50 *MeV* in the PSB (Proton Synchrotron Booster). Then, protons of 1.4 GeV are accelerated in the Proton Synchrotron (PS) reaching an energy of 25 GeV. Finally, the Super Proton Synchrotron (SPS) accelerates the proton beam up to 450 GeV before the injection in the LHC. The LHC hadron injector complex is illustrated on Figure 2.2.

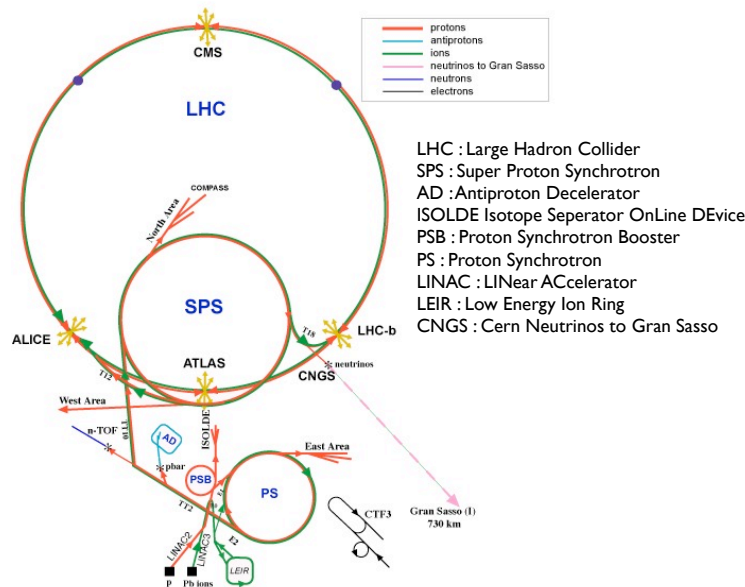


Figure 2.2: The LHC hadron injector complex.

2.2 Overview of three experiments : ATLAS, CMS and ALICE

2.2.1 ATLAS

The Toroidal LHC Apparatus (ATLAS) is dedicated to the study of the Higgs boson and to the physics beyond the Standard Model (as the CMS experiment). The ATLAS experiment is a cylinder of 22 m of diameter for 40 m length and weights 7000 tones. It has been designed in layers of sub-detectors as shown in Figure 2.3. It is made of an inner tracker dedicated to the reconstruction of charged particles, an electromagnetic calorimeter, a hadronic calorimeter and muon detectors. Neutrinos are the only particles missed by the ATLAS detector but their energy can be estimated from the measurement of the missing energy. More information about the purposes and the technical details of the ATLAS experiment can be found in [34].

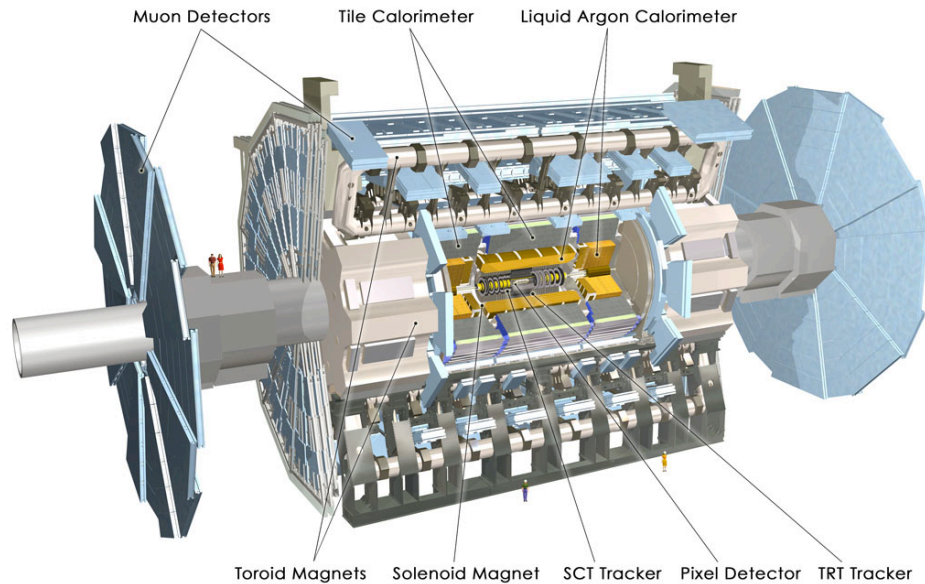


Figure 2.3: The ATLAS detector.

2.2.2 CMS

The Compact Muon Solenoid (CMS) experiment is the heaviest detector build around the LHC with its 12500 tons. As the ATLAS experiment the CMS detector consist of concentric sub-detectors. Compared to ATLAS, the main differences are:

- CMS is using a stronger magnetic field to achieve a better momentum resolution,
- The ATLAS jet resolution in the HCAL is better than CMS while CMS has a better ECAL resolution than ATLAS,

Chapter 2. CERN and the LHCb experiment

The scheme of the CMS experiment is presented on Figure 2.4. The CMS experiment is presented in [35].

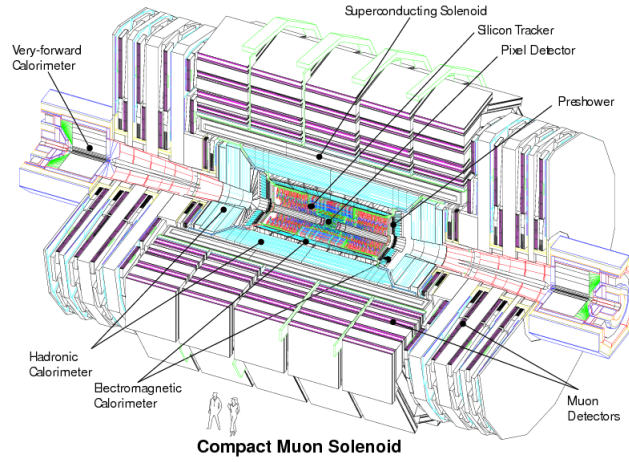


Figure 2.4: The CMS detector.

2.2.3 ALICE

This experiment is dedicated to the study of the Quark and Gluon Plasma (QGP). It studies heavy-ion ($Pb - Pb$) collisions at a center of mass energy of 2.76 TeV which reproduces the physical conditions just after the Big-Bang when quarks and gluons are not yet bounded. The comprehension of the phase transition between hadronic matter and the QGP predicted by the Quantum Chromo Dynamic (QCD) could provide a better understanding of the early Universe as well as collapses of dense stars [36].

The LHC injection stages are slightly different to accelerate and collide heavy lead ions than protons. It requires a second linear accelerator (Linac3) to accelerate ions. The ionized Pb nucleons reach an energy of 4.2 MeV and are collided with a carbon target to remove their electrons. Then, they are injected in the LEIR (Low Energy Ion Ring) and accelerated up to 72 MeV per nucleons. An energy of 5.9 GeV is reached in the PS where a second carbon target is present to remove the remaining electrons. Finally, the nucleons are accelerated up to 177 GeV in the SPS before the injection in the LHC [37].

The ALICE detector is presented on Figure 2.5.

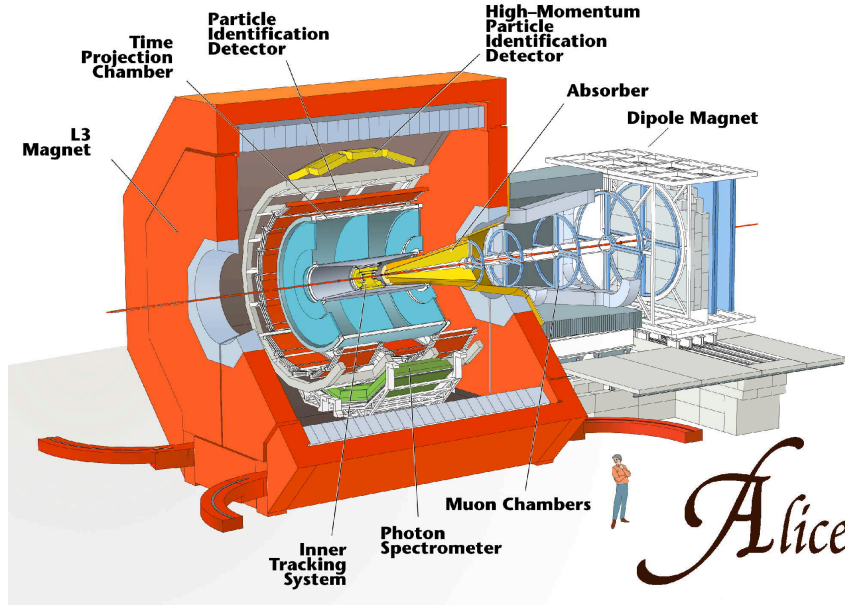


Figure 2.5: The ALICE experiment.

2.3 The LHCb experiment

The LHCb (for LHC beauty) detector is a single-arm forward spectrometer dedicated to the study of flavor physics. The principal aim of the LHCb experiment is to measure precisely CP violation processes and to search for new physics signs in rare decays. Its geometrical acceptance of $15 < \theta < 300$ mrad, corresponding to a pseudorapidity (defined as $\eta = -\ln(\tan(\theta/2))$) of $1.8 < \eta < 4.9$, has been chosen to study b and c hadrons. Indeed, b and c hadrons produced at the interaction point are boosted along the beam direction with a high longitudinal momentum for a relatively small transverse momentum. The luminosity at the LHCb interaction point is of about $\mathcal{L} = 2 \times 10^{32} \text{ cm}^{-2} \text{ s}^{-1}$ which is lower than ATLAS and CMS. Indeed, the beams are defocused on purpose at LHCb to reduce the number of primary interaction in an event. As shown on Figure 2.6, in addition to the magnet, the LHCb experiment is composed of various sub-detectors:

- A tracking system composed of the VERTex LOcator (VELO), the Tracker Turicensis (TT), the three Tracking stations T1, T2 and T3 (each composed of an Inner Tracker (IT) and an Outer Tracker (OT)),
- Two Ring Imaging CHerenkov Counter (RICH1 and RICH2),
- An Electromagnetic and a Hadronic CALorimeter (ECAL and HCAL),
- Five muon chambers (M1-M5),

These sub-detectors are described in the following sections together with the presentation of the track reconstruction procedure and the trigger systems. These sections summarize the main properties of the LHCb detector detailed in Ref. [38].

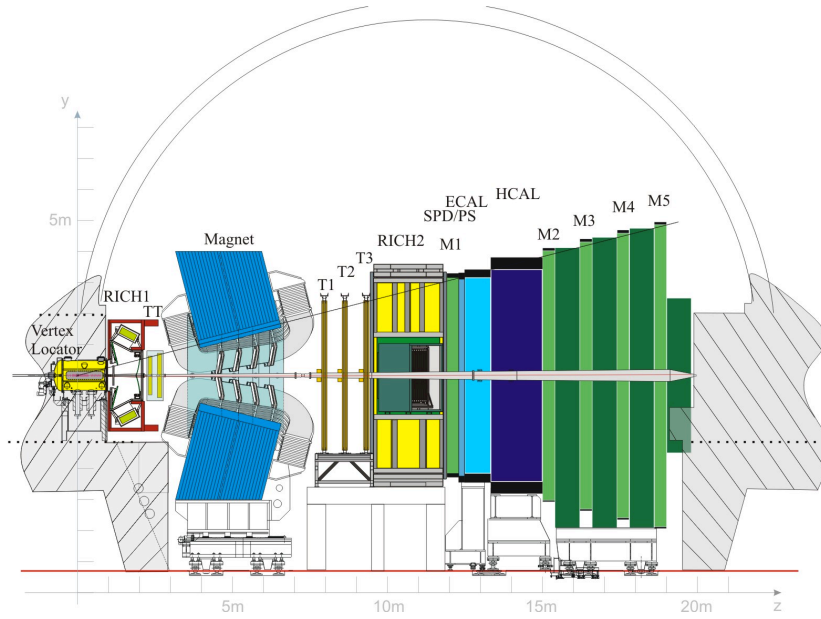


Figure 2.6: The LHCb spectrometer in the non-bending plane with its different components.

2.3.1 The Magnet

A dipole magnet of dimension $11\text{ m} \times 8\text{ m} \times 2.6\text{ m}$ for 1600 tons has been build to ensure a precise measurement of chaged tracks momentum. It is located between TT and the three tracking station T1, T2 and T3. It provides an integrated magnetic field of 4 Tm for tracks of 10 m length (0.1159 Tm in a region of $(0 - 2.5\text{ m})$ upstream the TT and 3.615 Tm in a region of $(2.5 - 7.95\text{ m})$ downstream the TT). Momentum resolution of around 0.4% for momenta up to $200\text{ GeV}/c$ requires a precise knowledge of the magnetic field. Typically, the integrated magnetic field is determined with a precision of the order of 10^{-4} . The nominal current of 5.85 kA for a total resistance of $100\text{ m}\Omega$ at 20°C induces a power dissipation of about 4.2 MW which requires a cooling system composed of a water flow of $150\text{ m}^3/h$ under a pressure of 11 bar at 25°C . On Figure 2.7, the magnet coil with its cooling system and power supplies are presented.

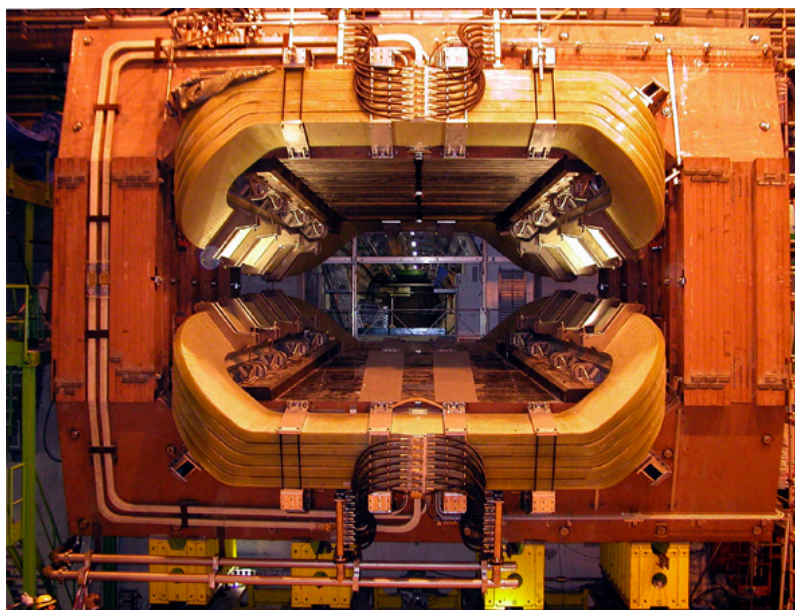


Figure 2.7: The LHCb dipole and its cooling system and power supplies in a transverse view.

2.3.2 The tracking system

2.3.2.a The VERtEX LOCator

The VELO has been designed to measure the decay vertex positions of b and c hadrons. A very good resolution on the primary and the secondary vertices positions and on the charged tracks momentum are needed to measure lifetimes with precision. The search for Long-Lived Particles (LLP) is exploiting the high accuracy of the VELO to reconstruct displaced vertices thanks to this silicon sub-detector surrounding the interaction point. The VELO is formed of two retractable detector halves composed of 25 stations of silicon sensors build perpendicularly to the beam direction which measure the radial r and the azimuthal ϕ position of each tracks coming from the region close to the collision point. A scheme of the VELO and its stations is shown on the top of Figure 2.8. The longitudinal positions are provided by the z position of each stations. Each modules is composed of silicon strips dedicated to the azimuthal and radial detection. The VELO sensors are illustrated on Figure 2.9.

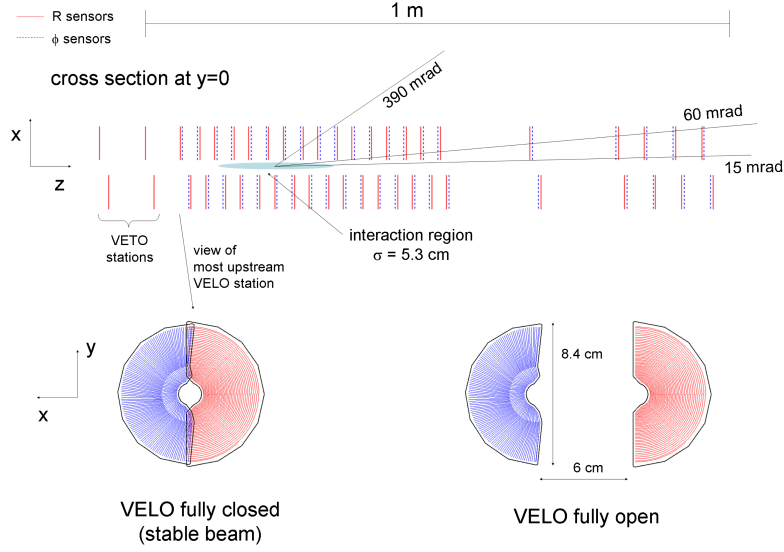


Figure 2.8: The VELO dimensions represented in the plane (x,z) at $y=0$ illustrations of the open and closed position.

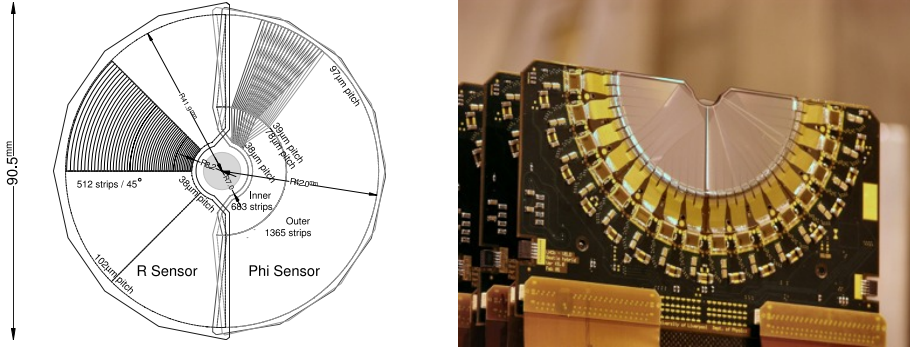


Figure 2.9: Geometry of the VELO sensors in ϕr and picture of sensors position on one of the two retractable halves.

At least three VELO stations have to be crossed by the track to be reconstructed in the geometrical acceptance of $1.6 < \eta < 4.6$. The cooling system maintains the VELO, which is located in an extreme radiation environment, at a temperature between -10 and 0°C to minimize radiation-induced effects. RF-boxes of $300\mu\text{m}$ thick aluminum protects the VELO from the RF noise induced by the beam and dissociates it from the LHC vacuum. During the protons injection, the sensors are in the “open” position to avoid radiation damages. When stable collisions are established, the sensors are placed in the “closed” position for data acquisition as shown in the bottom of Figure 2.8.

The VELO achieves quite impressive performances:

- The signal to noise ratio (S/N) ratio is better than 18,
- The best hit resolution is about $4\ \mu m$,
- It has a PV resolution of about $13\ \mu m$ in the (X,Y) plane for $69\ \mu m$ in the Z coordinate (for 25 tracks/vertex).

2.3.2.b The Silicon Tracker (ST): The Tracker Turicensis and The Inner Tracker

The Silicon Tracker is made up of the Tracker Turicensis and the Inner Tracker which are made of silicon microstrips of $\sim 200\ \mu m$ thick providing a spatial resolution of $\sim 50\ \mu m$. The TT stations of dimension $150 \times 130\ cm$ have been built upstream the magnet in four stations of four detection layers (x-u-v-x) as exposed on Figure 2.10. Its main purpose is to contribute to the reconstruction of low momentum tracks and of long-lived particles decaying outside the VELO. Vertical strips composed the first and the last layer while the second and third layers are made of strips rotated by respectively -5° and $+5^\circ$. The strip lengths have been optimized for different regions of the detector to maximize the strip occupancy. Typically, the hit occupancy of charged particles are 5×10^{-2} per cm^2 in the innermost regions whereas it is falling to $\sim 5 \times 10^{-4}$ per cm^2 in the outermost regions.

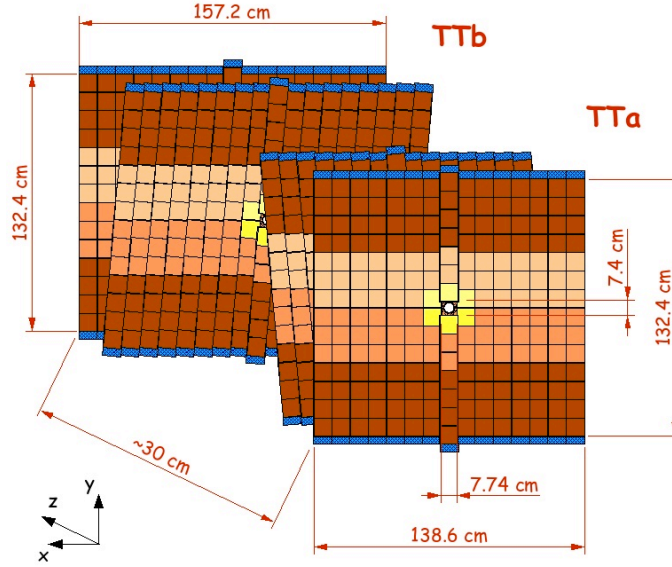


Figure 2.10: The four detection layers (x-u-v-x) with illustrations of the silicon microstrips.

The Inner Tracker (IT) is composed of three stations of four boxes surrounding the beampipe where the highest track density is observed (1.5×10^{-2} to 2×10^{-3} per cm^2) as shown on Figure 2.11.

Approximately 20% of charged particles produced at the collision point hit the IT stations.

The IT is therefore designed to provide an optimal spatial resolution for region with a high occupancy and support the radiation damages during a long operation time. Typically, the TT temperature does not exceed 5°C while the IT temperature is cooled at -15°C with C_6F_{14} to avoid that the induced leakage currents reach a level affecting significantly the signal-to-noise performance and to minimize the risk of thermal runaway.

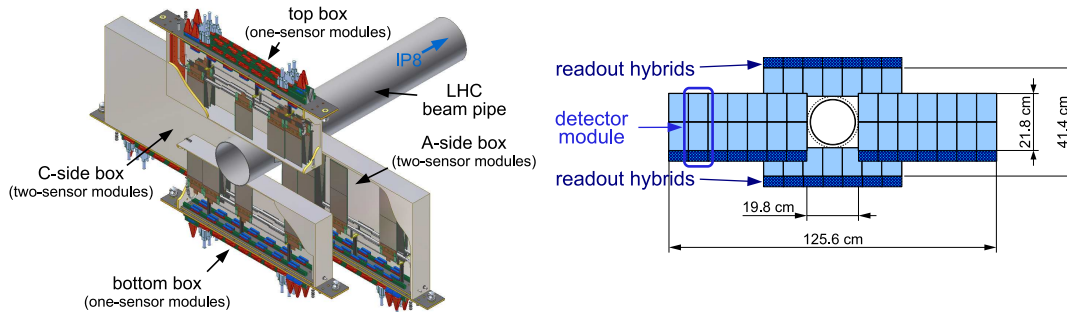


Figure 2.11: Representation of the four boxes of an IT station build around the LHC beam pipe with its dimension in the (x, y) plane.

2.3.2.c The Outer Tracker

The Outer Tracker is a drift-time detector build around the IT in the stations $T1$, $T2$ and $T3$ to measure charged particles track position over a large acceptance area. OT is composed of an array of gas-straw-tube modules which contains two layers of drift-tubes providing a very good resolution for the position of the passing particle. As for TT, OT is composed of four stations arranged in a geometrical configuration $x - u - v - x$ where the first and the last stations are made of vertical modules while the second and third stations are rotated by -5° and $+5^{\circ}$. The counting gas is a mix of Argon (70 %) and CO_2 (30 %) allowing a drift time below 50ns . The drift tubes have been aligned up to an accuracy of $100\text{ }\mu\text{m}$ in the x coordinate and 1 mm in the z coordinate. This mechanical alignment of the OT is crucial to provide a single cell resolution of $200\text{ }\mu\text{m}$. On Figure 2.12, the whole tracking system composed of the TT upstream the magnet and the three IT stations surrounded by the OT is presented.

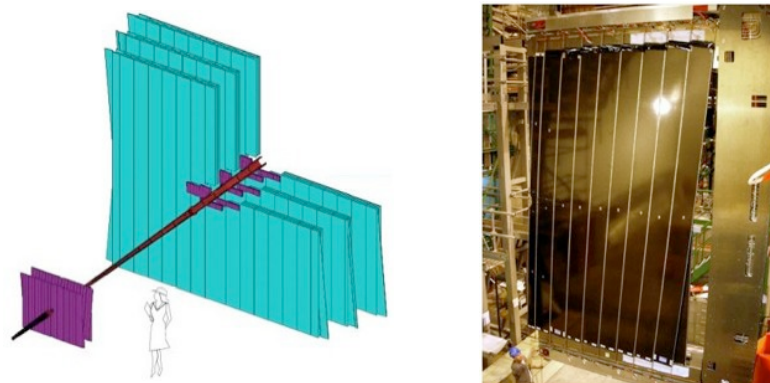


Figure 2.12: Representation of the tracking system composed of the TT and of the three IT stations (magenta) and of the OT (green) in addition with a picture of an OT station in the geometrical configuration "u".

2.3.2.d Track reconstruction

The reconstruction algorithm uses the hits in the different sub-detectors of the tracking system to compute the particles trajectory. The algorithm reconstructs the tracks starting from “seeds” which are track candidates in the VELO regions and the T stations (T1, T2 and T3). The trajectory is then refitted to deal with multiple scattering and are corrected for energy loss. A track is reconstructible if it has enough hits in the relevant detectors.

Several type of tracks are categorized and illustrated on Figure 2.13:

- Long Tracks: these tracks with the most precise momentum calculation are passing through the entire tracking system from the VELO to the T stations (T1, T2, T3),
- Downstream Tracks: these tracks are identified in the TT and the T stations and are typically from particles decaying outside the VELO (as K_s^0 and Λ),
- Upstream Tracks: tracks segment in the VELO and the TT only. These tracks are reconstructed from low momentum particles deflected by the magnetic field outside the detector after passing through the RICH1 detector. Cherenkov photons generated by these tracks are useful to understand the backgrounds in the RICHes,
- VELO Tracks: these tracks are VELO segment only and are often backward tracks used in the primary vertices reconstruction algorithm,
- T tracks: tracks crossing the T stations T1,T2 or T3 only which is the typical signature of particles produced by a secondary interaction,

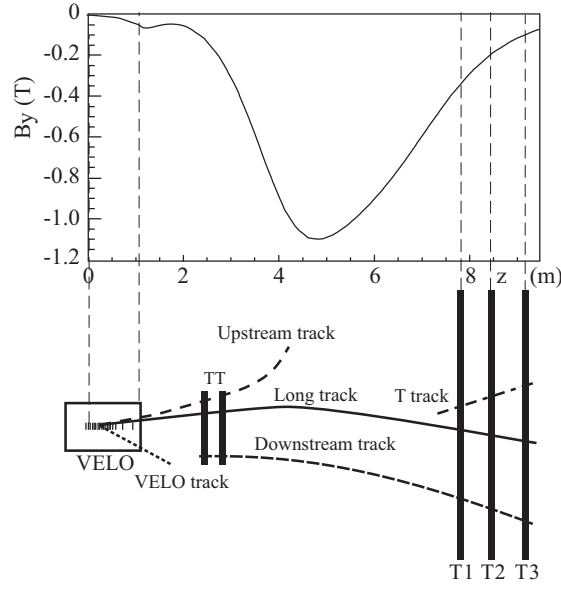


Figure 2.13: Definition of the different types of tracks considered by the reconstruction algorithms together with the amplitude of the magnetic field B as a function of the z coordinate. The VELO and T tracks used as "seeds" for the tracks reconstruction software are located in regions with low magnetic field.

2.3.3 Ring Imaging CHerenkov RICH 1 and 2

The RICH detectors RICH1 and RICH2 are dedicated to the detection of Cherenkov photons emitted by charged particles passing through a medium with a velocity β greater than the speed of light in this medium. The opening angle of the light cone is related to the speed of the charged particles which, combined with the momentum measured by the tracking system, allows to determine the mass of the particles. The light is reflected and focalized by spherical mirrors and deflected by planar mirrors to the Hybrid Photon Detectors (HPD) which allow to reconstruct the an image of the Cherenkov rings. The RICH1 and RICH2 information play a key role at LHCb in the particle identification procedure (PID). On Figure 2.14, the identification of particles by Cherenkov effect is illustrated in addition with an example of Cherenkov rings.

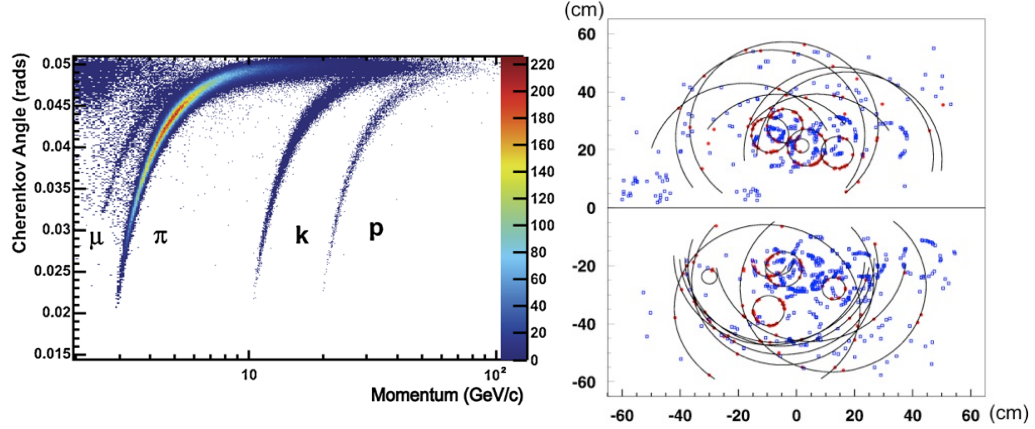


Figure 2.14: Left : Cherenkov angle for isolated tracks (Cherenkov ring does not overlap with others) as a function of the track momentum from the C_4F_{10} radiator. Right : Example of Cherenkov rings at LHCb. [3]

RICH1 is located upstream the dipole magnet and covers charged particles momentum from ~ 1 to 60 GeV/c by using the Cerenkov light emitted in the aerogel and C_4F_{10} radiators. RICH2 uses a CF_4 radiator and is placed after the T stations where the particles with highest momenta are found. It covers a momentum range of 15 – 100 GeV/c. It has a limited angular acceptance of $\pm 15 - 120$ mrad horizontally for ± 100 mrad vertically while RICH1 covers the full LHCb angular acceptance. RICH1 and RICH2 are presented on Figure 2.15.

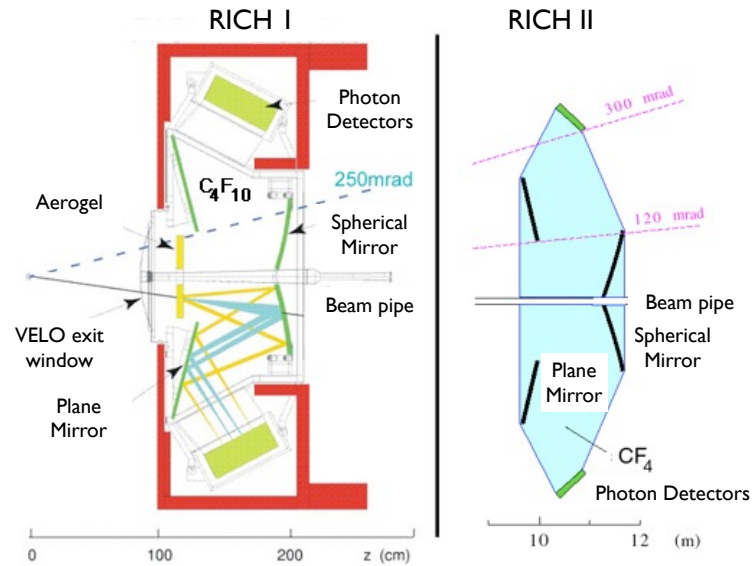


Figure 2.15: Representation of RICH1 and RICH2 with the different sets of mirrors and the HPD detecting the light emitted from particles passing through the medium (Aerogel, C_4F_{10} and CF_4).

2.3.4 Electromagnetic and Hadronic CALorimeters

The calorimeters are dedicated to energy and position measurements of electrons, photons and hadrons. They also provide the transverse energy of hadron, electron and photon candidates for the first trigger level.

The aim of the SPD/PS (Scintillating Pad Detector)/(PreShower) is to select charged particles and distinguishes charged from neutral particles. The scintillation light of the SPD and PS is collected using wavelength-shifting (WLS) fibers and are amplified by photomultipliers (MAPMTs).

The ECAL is composed of alternated scintillating tiles and lead plates readout by WLS fibers and for an angular acceptance coverage of $\pm 25 \text{ mrad}$ to $\pm 300 \text{ mrad}$ horizontally for $\pm 250 \text{ mrad}$ vertically. It has been designed to measure 25 radiation lengths for an energy resolution of about $\sigma/E(\text{GeV}) = 10\%/\sqrt{E} \otimes 1\%$. The saturation starts when particles deposite the equivalent of $E_T > 10 \text{ GeV}$ in a cell.

The HCAL is made of iron-scintillator samples which are playing the role of absorber and active materials. As the HCAL is mainly exploited at the trigger level, it measures a hadron interaction length of about $5.6 \lambda_I$ only while the ECAL is measuring the totality of the electromagnetic shower. It is build to cover an angular acceptance similar to that of the ECAL for an energy resolution of $\sigma/E(\text{GeV}) = (69 \pm 5)\%/\sqrt{E} \otimes (9 \pm 2)\%$.

The segmentation structure of the SPD/PS, ECAL and the HCAL are presented on Figure 2.16. The different sections defined in red, blue and yellow for the ECAL and in red and yellow for the HCAL have been designed to keep a constant occupancy. Indeed, the hit density changes by two orders of magnitude over the calorimeter surface. The smaller cells are closest to the beam where the particle density is larger.

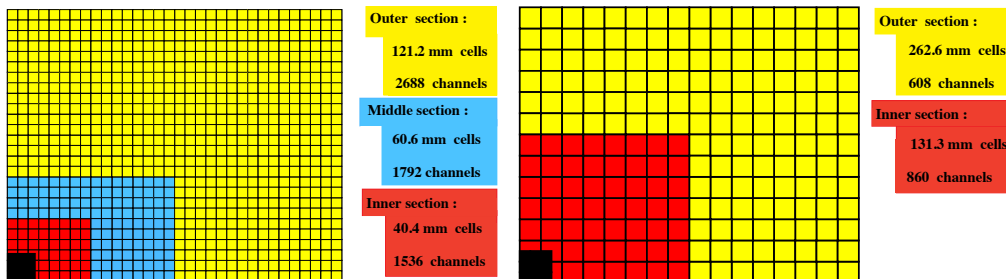


Figure 2.16: Cells dimensions given for SPD/PS and ECAL (left) and for HCAL (right) presented on one quarter of the detector in the (x, y) plane.

2.3.5 Muon chambers

Muons are detected by the muon system placed at the end of the spectrometer. It consists of five chambers (M1-M5) of charged particles detectors. The first chamber is placed in front of the calorimeter system for an improvement of the transverse momentum measurement at the trigger level. The last four stations are interleaved with Fe absorbers of 80 cm of thickness. As muons interact weakly with the detector material, they can penetrate through the calorimeter and Fe absorbers while all the others particles are stopped. A minimal muon momentum of 6 GeV/c only is required to pass through the whole system which corresponds to about 20 radiation lengths.

The muon system which provides a p_T resolution of 20% is made of 1380 muon chambers covering a section of 435 m^2 for a geometrical acceptance of 16 to 258 $mrad$ vertically and of 20 to 306 $mrad$ horizontally. The five muons chambers in addition with a transverse view of the muon stations are illustrated on Figure 2.17.

The tracking device is composed of Multi Wire Proportional Chambers (MWPC) and Gas Electron Multipliers (GEM). Since the interaction rate is high, triple GEM detectors are used instead of MWPC in the inner region of M1.

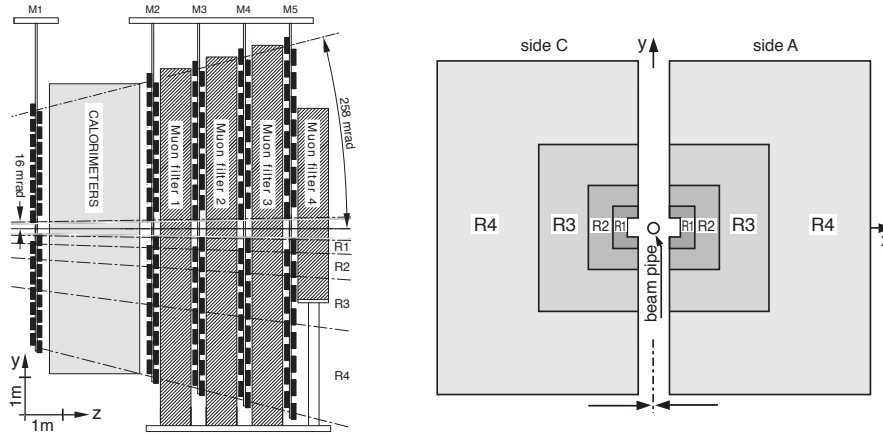


Figure 2.17: Side view of the LHCb Muon Detector (left) with the different stations M1-M5. Each station is divided in four regions $R1 - R4$ (right) where the size of their logical pads are scaled by the ratio 1:2:4:8. [4]

2.3.6 The trigger systems

The role of the trigger systems is to reduce the number of recorded events, discarding events which are not relevant for physics studies. It reduces the beam crossing rate of 40 MHz (but 10 MHz of visible crossing rate) to an acceptable rate for storage ($\sim 2 kHz$). The main trigger decisions are separated in three levels : Level-0 Trigger (L0), High-Level Trigger (HLT)1 and HLT2.

Chapter 2. CERN and the LHCb experiment

The L0 processes the data using the information of the hardware components of the LHCb detector as the VELO, the calorimeters and the muon chambers.

The L0 is considering:

- hadrons, electrons and photons from calorimeter information with the largest E_T (L0-Calorimeter trigger),
- the two highest values of muon transverse momentum p_T measured in the muon chambers (L0-Muon trigger);

In addition, the L0-PileUp trigger of the VELO is used for the determination of the luminosity by estimating the number of pp interactions in each bunch crossing.

L0 reduces the visible crossing rate from 10 MHz to 1 MHz. The High Level Trigger (HLT) is a C++ software-only application which has access to the information of events passing L0 decisions (the lines). Those algorithms are based on the same software used for the LHCb offline data processing. The HLT is composed of two sub-levels. HLT1 reduces the rate from 1 MHz to 43 kHz and refines the L0 decisions by reconstructing particle tracks from the VELO and T stations hits in combination with requirements on the transverse momentum or impact parameters of tracks. In addition, it confirms that no charged particles could be associated to a γ or a π^0 candidate in the calorimeters.

Tracks are combined in HLT2 to form composite particles as for the offline analysis but without refitting tracks by a Kalman filter. HLT2 is performing combination of inclusive and exclusive algorithms which aim to reconstruct and select the candidates required by the different analysis performed at LHCb. At this stage, the rate is about 4 kHz and the data is stored for further analysis. Additional information about the LHCb trigger system and its performance in 2011 can be found in [39]. The architecture of the LHCb trigger is presented in Figure 2.18.

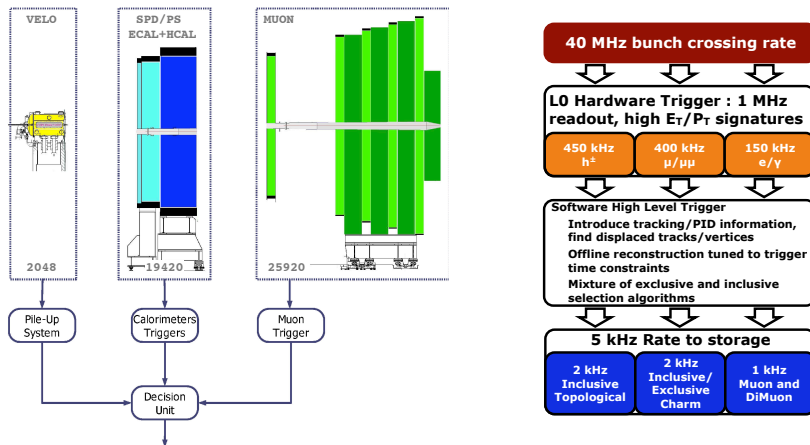


Figure 2.18: Architecture of the LHCb trigger : scheme of the Level-0 trigger (left) and diagram of the three trigger stages with their corresponding reduction rate (right).

2.3.7 LHCb Software

The LHCb software is based on the open framework GAUDI [40] which provides the tools for the Monte Carlo generation, the online and offline analysis. The main packages are:

- **Gauss**: this package manages the generation of Monte Carlo simulation. First, it generates the physics of the pp collisions and the different decay cascades of the particles in the event through an event generators usually PYTHIA. The different physical processes undergone by the generated particles inside the LHCb detector are then simulated with Geant4 which models the LHCb detector,
- **Boole**: is dedicated to the digitalisation of the LHCb detector response of each particles simulated by Gauss. It simulates the signal response of all the sub-detectors and taking into account the several electronic noises,
- **Moore**: executes the high level trigger code of the different trigger lines for the HLT itself and the Monte Carlo simulation,
- **Brunel**: the outputs from Boole are collected to perform the track reconstruction from the different hits and from the information given by the calorimeters. The particles properties as the PID determined from the RICH or the particle momentum are stored in data summary tape (known as DST) to be processed in offline analysis,
- **DaVinci**: the data are organized in different streams dedicated to specific analysis in order to reduce the data storage and the computing time. These Stripping lines are implemented with the DaVinci software which is also used for the offline analysis. It provides a large number of tools dedicated to the handling of the physical information available in the DST.

3 Search for long-lived particles decaying semileptonically

This section presents the criteria considered for the selection and reconstruction of events with LLPs. The procedure is subdivided into two main steps. In the first step events with a displaced high p_T muon are selected. For this we exploit dedicated trigger and stripping lines. Then a displaced vertex is reconstructed by combining charged tracks including the muon.

Simulated events are used to define the analysis criteria and to compute the detection efficiency.

3.1 Events samples considered in this study

Table 3.1 presents a summary of the different set of events used in this analysis. The datasets collected in 2011 and 2012 correspond to 0.98 fb^{-1} and 1.98 fb^{-1} respectively. The signal and background models have been generated by Pythia 8 and fully simulated by GEANT4 with the official simulations conditions for the two years.

The SUSY parameters for each simulated signal sample are presented on Table 3.2. At least one $\tilde{\chi}_1^0$ and one muon in the enlarged LHCb acceptance $1.5 \leq \eta \leq 5$ are required. Similar criteria are applied for the production of the background MC samples.

The main source of background is from $b\bar{b}$ events. The LHCb standard inclusive b simulation is ineffective for this analysis which requires a high p_T muon. The muon can be produced in a restrictive portion of the phase space where the b quarks are produced with a large transverse momentum. Therefore, a special $b\bar{b}$ production has been done to better match the phase space of interest, as described in Section 3.1.2. Because of the large computing time required, this production has been performed only for $\sqrt{s} = 7 \text{ TeV}$.

Chapter 3. Search for long-lived particles decaying semileptonically

Table 3.1: Summary of data and full simulation MC (2011 and 2012) sets of events used in this study. $N(year)$ is the number of generated events with the simulations conditions for the given year. Mass units are in GeV/c^2 . The number of collisions per bunch in the beam settings of the full simulated samples is $\nu = 2$ for 2011 and $\nu = 2.5$ for 2012. The geometrical acceptance is defined as $1.5 \leq \eta_\mu \leq 5$.

Set		$N(2011)$	$N(2012)$
LV38 5ps	$m(\tilde{\chi}_1^0)=38 \quad \tau = 5 \text{ ps}$	42.9k	38.7k
LV38 10ps	$m(\tilde{\chi}_1^0)=38 \quad \tau = 10 \text{ ps}$	41.4k	38.9k
LV38 50ps	$m(\tilde{\chi}_1^0)=38 \quad \tau = 50 \text{ ps}$	42.3k	39.0k
LV98 5ps	$m(\tilde{\chi}_1^0)=98 \quad \tau = 5 \text{ ps}$	34.1k	38.2k
LV98 10ps	$m(\tilde{\chi}_1^0)=98 \quad \tau = 10 \text{ ps}$	43.5k	38.3k
LV98 50ps	$m(\tilde{\chi}_1^0)=98 \quad \tau = 50 \text{ ps}$	43.1k	37.9k
LV198 5ps	$m(\tilde{\chi}_1^0)=198 \quad \tau = 5 \text{ ps}$	44.6k	38.0k
LV198 10ps	$m(\tilde{\chi}_1^0)=198 \quad \tau = 10 \text{ ps}$	43.0k	37.7k
LV198 50ps	$m(\tilde{\chi}_1^0)=198 \quad \tau = 50 \text{ ps}$	35.0k	38.1k
$W \rightarrow \mu\nu$		5M	
$Z/\gamma^* \rightarrow \mu\mu$		2M	
$W \rightarrow \tau\nu$		5M	
$Z \rightarrow \tau\tau$		1.05M	
$t\bar{t}$	$t \rightarrow b\bar{b} + 1 \text{ lepton}(p_T > 10 \text{ GeV}/c)$	493.2k	
Special $b\bar{b}$	one b in acceptance $1.5 \leq \eta \leq 5$ + one μ in acceptance, $p_T(\mu) > 12 \text{ GeV}/c$	214.1k	
Data 2011	Reco14 (EW) Strip20r1p1	$\int \text{Ldt} = 0.98 \text{ fb}^{-1}$	
Data 2012	Reco14 (EW) Strip20r0p1	$\int \text{Ldt} = 1.98 \text{ fb}^{-1}$	

3.1.1 Signal samples

Table 3.2, presents the SUSY parameters $M1$, $M2$, $\tan\beta$, μ and $m_{\tilde{q}}$ used to produce the particle spectrum. All other SUSY parameters are set to their default Pythia values. The masses of the SUSY particles and therefore the kinematics of the process are determined by the SUSY parameters together with the lifetime τ of the neutralino which has been chosen to be 5, 10 and 50 ps. The efficiencies at generator level, ϵ_{Gen} , requiring at least one muon and one LLP in the LHCb acceptance are of the order of 11% and can be found on Table 3.3.

3.1. Events samples considered in this study

Table 3.2: SUSY parameters of the models considered. The LLP of the LV model is the lightest super-partner, the neutralino : $\tilde{\chi}_1^0$. M1 and M2 are the Pythia parameters RMSS(1) and RMSS(2), $m_{\tilde{g}}$ is RMSS(3), μ is RMSS(4), $\tan \beta$ RMSS(5) and $m_{\tilde{q}}$ is RMSS(8-12). Samples with lifetime of 5,10 and 50 ps have been generated for each mass. The lifetime of the LLP is fixed by hand.

Model	M1	M2	$m_{\tilde{g}}$	$\tan \beta$	μ	$m_{\tilde{q}}$	$m_{\text{LLP}} (GeV/c^2)$
LV38	40	2000	2000	2.0	1200	1300	38
LV98	100	2000	2000	2.0	1200	1300	98
LV198	200	2000	2000	2.0	1200	1300	198

Table 3.3: Generator efficiency, ϵ_{Gen} , (in percent) for events with at least one LLP and one muon in the LHCb acceptance at $\sqrt{s} = 7$ TeV (2011) and $\sqrt{s} = 8$ TeV (2012) of the different models and the corresponding lifetime.

Model \ τ (ps)	5	10	50
LV38 (2011)	11.08 ± 0.10	11.09 ± 0.07	11.30 ± 0.11
LV98 (2011)	11.00 ± 0.08	11.30 ± 0.19	11.08 ± 0.10
LV198 (2011)	11.07 ± 0.10	11.12 ± 0.10	11.14 ± 0.05
LV38 (2012)	12.15 ± 0.09	12.17 ± 0.10	12.34 ± 0.11
LV98 (2012)	12.09 ± 0.10	12.07 ± 0.10	12.22 ± 0.08
LV198 (2012)	12.07 ± 0.11	12.24 ± 0.11	11.81 ± 0.10

3.1.2 Background samples

The typical signature of massive long-lived particles decaying semileptonically is a displaced vertex reconstructed with several tracks and a high transverse momentum lepton. Several types of SM background processes can fake a displaced vertex with a lepton. The following processes have been identified:

- semi-leptonic decay of b-hadron (QCD background) decaying into a high p_T muon and several tracks,
- idem for c-hadrons,
- muonic decays of W and Z with additional tracks from the PV, for instance,
- $t\bar{t}$,
- “punch-through” hadrons misidentified as muons subsequently combined with other tracks,
- particle interacting with the detector structure, mainly the RF-shield in the VELO.

The interactions with the detector material are discarded by the procedure described in Section 3.3.3. After that, the main source of background is from QCD processes with b-hadrons. $c\bar{c}$ and $t\bar{t}$ contributions are found to be negligible. W and Z muonic decays are efficiently discarded by requiring that the muon is non prompt. Note that the high p_T muons coming from the W and Z background share the kinematical properties of the muons from signal. Therefore these similarities allow to use such decays as control channels. The punch-through component can be removed by requiring a maximal fraction of energy deposit by the muon candidate in the calorimeters [41].

3.1.2.a Special $b\bar{b}$ production

The aim of the special generation of $b\bar{b}$ events is to provide a simulated set with kinematic properties similar to the signal. A study has been made to optimize a cut on the partonic \hat{p}_T of the generation process. The corresponding distribution in Pythia is shown in Figure 3.1. Only quarks with a relatively large \hat{p}_T can produce high energy hadrons subsequently decaying into high- p_T muons. The MC generator efficiency has been maximized while preserving the coverage of the kinematical properties of $b\bar{b}$ as required by the present analysis. The minimal value of \hat{p}_T has been determined at the generator level by computing the generator cross-section times the fraction ϵ_{gen} of events satisfying some basic analysis criteria:

- a muon of $p_T > 12$ GeV/c in the pseudorapidity window $\eta \in [1.5, 5]$,
- and a b-hadron with $p_T > 2$ GeV/c also in $\eta \in [1.5, 5]$,

Figure 3.2 shows the evolution of $\epsilon_{gen} \times \sigma$ (cross-section) as a function of \hat{p}_T which is quite flat up to $\hat{p}_T^{min} \sim 20$ GeV/c. Therefore, this value has been chosen for the production of the special $b\bar{b}$ MC sample.

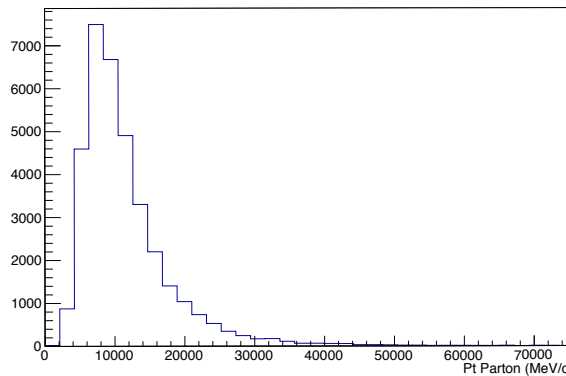


Figure 3.1: Pythia \hat{p}_T distribution for $b\bar{b}$ generation.

3.2. Characteristics of the signal from MC truth (generator-level studies)

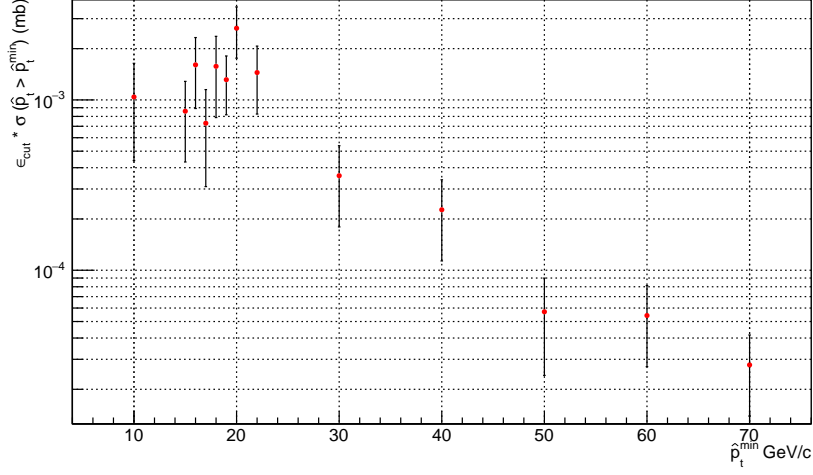


Figure 3.2: Cross-section times the fraction of events ϵ_{gen} with a muon of $p_T > 12$ GeV/c and a b-hadron in the LHCb enlarged geometrical acceptance $\eta \in [1.5, 5]$, as a function of the \hat{p}_T^{min} .

The generator efficiency for the special sample is $(9.29 \pm 0.11) \cdot 10^{-4}$. The \hat{p}_T^{min} cut improves this efficiency by a factor of about 10^5 in comparison with the standard inclusive $b\bar{b}$ simulation.

In the following, for the prediction of the $b\bar{b}$ background yield we consider the total inclusive value of $\sigma(pp \rightarrow b\bar{b}X) = \sigma_{incl}^{b\bar{b}} = 288 \pm 4 \pm 48 \mu b$ measured by LHCb [42]. As previously stated we do not have MC samples at 8 TeV. From an estimate done with the Pythia generator, the cross-section is about 20% larger than at 7 TeV, allowing a simple extrapolation.

3.2 Characteristics of the signal from MC truth (generator-level studies)

For neutralino masses of 38 and 98 GeV/c², the branching ratio of $\tilde{\chi}_1^0 \rightarrow \mu^+ q_i q_j (\mu^- \bar{q}_i \bar{q}_j)$ is 8.3 % for each quark composition ($q_i = u, c$ and $q_j = \bar{d}, \bar{s}, \bar{b}$) with 50% of μ^+ and μ^- . A small contribution of $q_i = t$ (0.02%) arises for models with neutralino mass of 198 GeV/c².

Some kinematical properties provided by the 4-vector information of the LLP and the associated muon can be found in the Figures from 3.3 to 3.6, for the different neutralino masses and lifetime.

Figure 3.3 shows the p_T , the isolation variable and the impact parameter to the Primary Vertex (PV) of the muon. The muon isolation is defined as the sum of the energy of tracks surrounding the muon in a cone build in the (η, ϕ) space of radius $R_{\eta\phi} = 0.3$ divided by the energy of the muon track (a value of one denotes a fully isolated muon). Because of the high masses of the LLPs the muon is expected to be more isolated on average in comparison with muons coming from the background due to b-hadrons decays. The impact parameter of the

muon with respect to the associated primary vertex is shown for different lifetime of the LLP. This parameter distinguish LLP muons from muons coming from W and Z decays.

Figure 3.4 shows the flight distance of the LLP defined as the distance between the associated primary vertex and the decay position of the LLP. On Figure 3.5 the radial distance to the z axis and the z decay position of the LLP are presented. The radial distance is a key variable for the displaced vertices reconstruction algorithm implemented for this analysis. By requiring a minimal radial distance of the vertex, the prompt background component can be discarded. This is the case for W and Z decays.

The reconstructed transverse momentum of the LLP is shown on Figure 3.6 together with the mass of the LLP. To get closer to the analysis conditions, only charged stable particles falling inside the LHCb acceptance have been considered for this reconstruction.

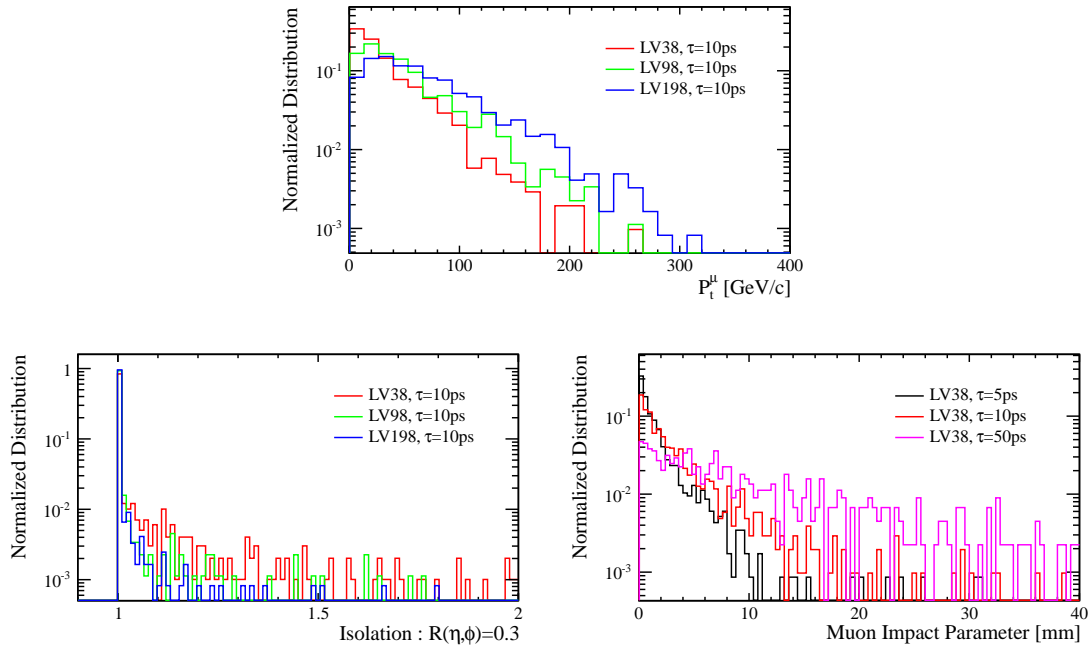


Figure 3.3: Properties of the muon coming from the LLP. Top: transverse momentum of the muon in the LHCb acceptance. Bottom left: isolation variable of the muon. Bottom right: impact parameter of the muon with respect to the associated primary vertex.

3.2. Characteristics of the signal from MC truth (generator-level studies)

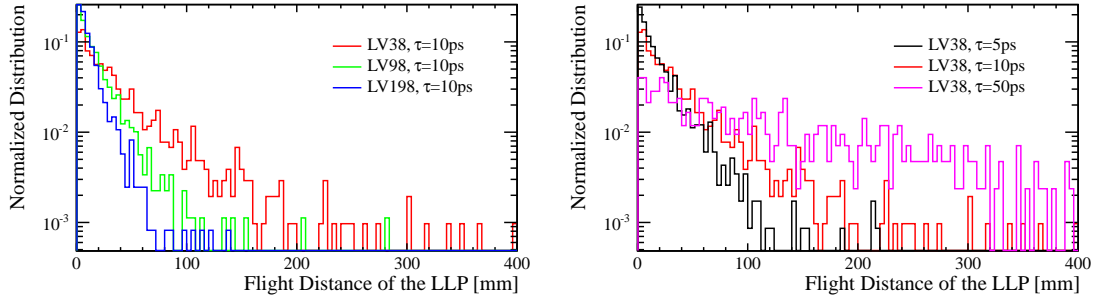


Figure 3.4: Flight distance of the LLP for several masses (left) and different lifetime for LV38 (right).

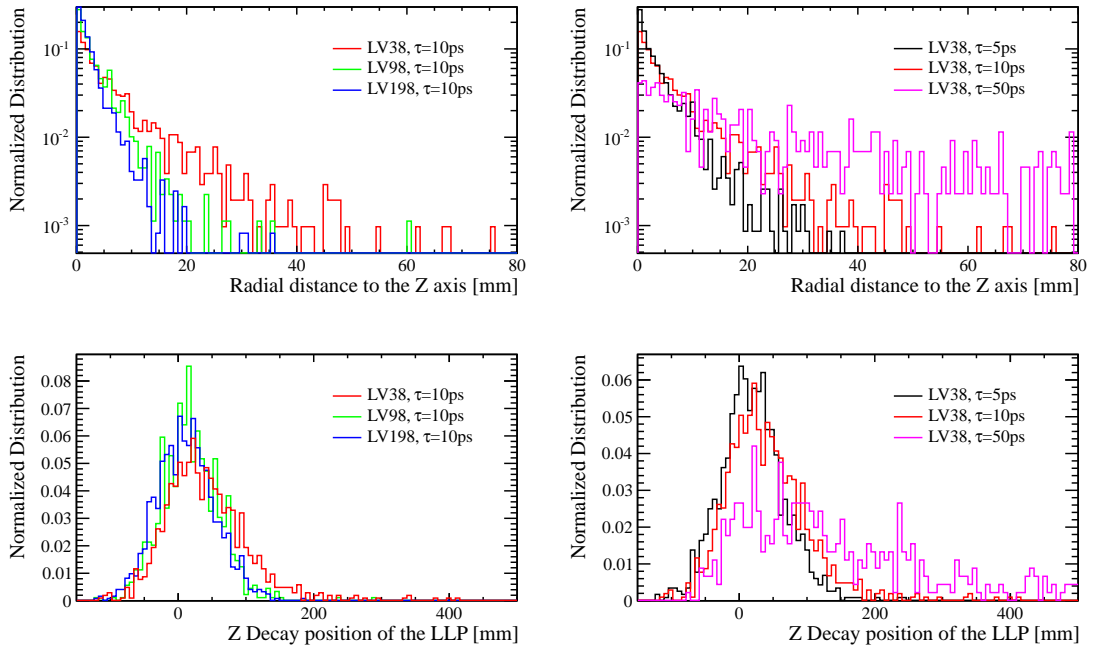


Figure 3.5: Geometrical properties of the LLP decay vertex for several masses (left) and different lifetime for LV38 (right): Top: radial distance to the Z axis, bottom: Z decay position of the LLP.

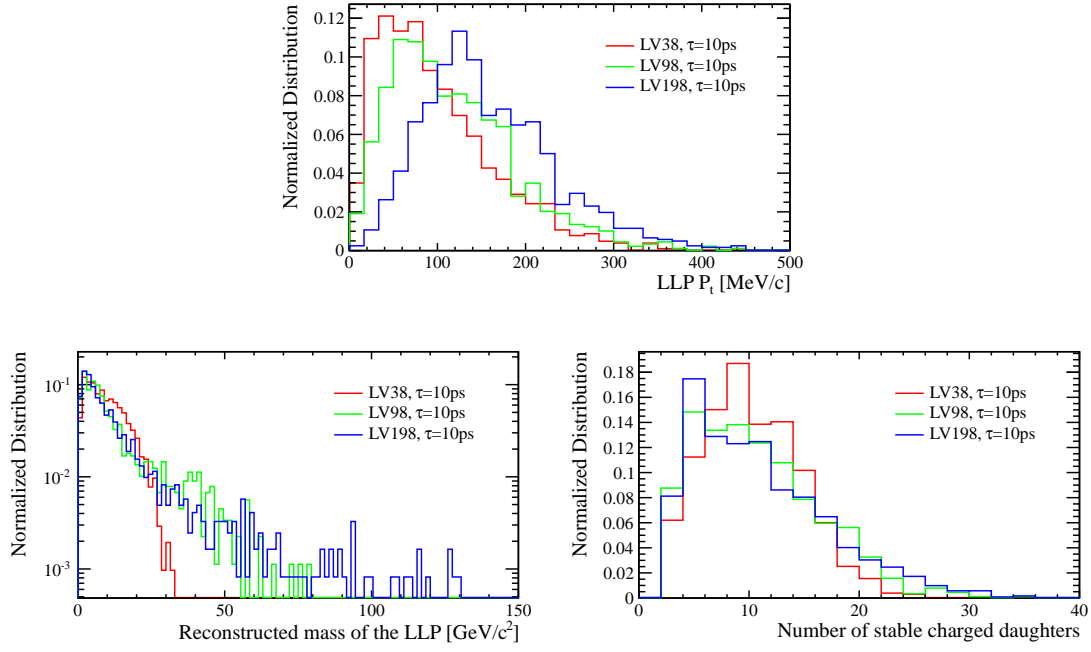


Figure 3.6: Transverse momentum of the LLP (top). Mass of the LLP reconstructed with the stable charged daughters in the LHCb acceptance (bottom left). Number of stable charged daughters in the LHCb acceptance (bottom right).

3.3 Data selection

3.3.1 Trigger and Stripping algorithms

The selection applied at the trigger and the stripping level are summarized on Table 3.4.

Events are required to pass the `L0Muon`, `Hlt1SingleMuonHighPT`, `Hlt2SingleMuonHighPT` and finally the `StrippingLLP2MuXHighPTHHighIPMuon`. The stripping algorithm is part of the Electro-Weak (EW) stripping 20r1p1 for 2011 data (incremental restripping of 2011 data with the reconstruction Reco14) and stripping 20r0p1 for 2012. It asks for a muon with a minimum transverse momentum of 12 GeV/c and a minimum impact parameter with respect to the best primary vertex of 0.25 mm in the event.

Table 3.4: Summary of the selection criteria applied on the muon at the `Hlt1SingleMuonHighPTDecision`, `Hlt2SingleMuonHighPTDecision` and `StrippingLLP2MuXHighPTHHighIPMuonLine` level.

	Track	p_T	IP
<code>Hlt1SingleMuonHighPTDecision</code>	$\chi^2/nDoF < 3$	$p_T > 4.8 \text{ GeV/c}$	X
<code>Hlt2SingleMuonHighPTDecision</code>	X	$p_T > 10 \text{ GeV/c}$	X
<code>StrippingLLP2MuXHighPTHHighIPMuon</code>	X	$p_T > 12 \text{ GeV/c}$	$IP > 0.25 \text{ mm}$

The efficiency of the trigger and stripping is determined from the Monte Carlo signal samples. The results are summarized on Table 3.5 , 3.6 and 3.7 for $\sqrt{s} = 7 \text{ TeV}$ (2011) and on Table 3.8 , 3.9 and 3.10 for $\sqrt{s} = 8 \text{ TeV}$ (2012). The systematic uncertainties on the selection efficiency induced by the trigger and the stripping have been estimated with $Z \rightarrow \mu^+ \mu^-$ events as presented in Section 3.5.

Table 3.5: Trigger and stripping efficiencies in percent for signal models with a mass of 38 GeV/c² at $\sqrt{s} = 7 \text{ TeV}$. The uncertainties are statistical. `Hlt1`, `Hlt2` and `Stripping` is referring to `Hlt1SingleMuonHighPTDecision`, `Hlt2SingleMuonHighPTDecision` and `StrippingLLP2MuXHighPTHHighIPMuonLine`.

	$LV38,5ps$	$LV38,10ps$	$LV38,50ps$
<code>L0Muon</code>	81.13 ± 0.19	81.38 ± 0.19	80.96 ± 0.19
<code>Hlt1</code>	57.98 ± 0.26	55.34 ± 0.27	37.70 ± 0.26
<code>Hlt2</code>	78.92 ± 0.29	79.22 ± 0.30	77.39 ± 0.37
<code>Stripping</code>	49.59 ± 0.42	61.72 ± 0.38	70.78 ± 0.65
Total	18.42 ± 0.19	22.02 ± 0.20	16.72 ± 0.18

Table 3.6: Same as Table 3.5 for signal models with a mass of 98 GeV/c².

	<i>LV98,5ps</i>	<i>LV98,10ps</i>	<i>LV98,50ps</i>
<i>L0Muon</i>	83.72 ± 0.20	83.41 ± 0.18	83.69 ± 0.18
<i>Hlt1</i>	62.27 ± 0.29	60.06 ± 0.26	43.80 ± 0.26
<i>Hlt2</i>	82.90 ± 0.28	82.97 ± 0.25	82.86 ± 0.30
<i>Stripping</i>	53.24 ± 0.30	66.57 ± 0.37	76.51 ± 0.63
Total	23.01 ± 0.23	27.67 ± 0.21	23.24 ± 0.20

Table 3.7: Same as Table 3.5 for signal models with a mass of 198 GeV/c².

	<i>LV198,5ps</i>	<i>LV198,10ps</i>	<i>LV198,50ps</i>
<i>L0Muon</i>	85.45 ± 0.17	85.65 ± 0.17	85.11 ± 0.19
<i>Hlt1</i>	62.98 ± 0.25	60.02 ± 0.26	42.28 ± 0.29
<i>Hlt2</i>	89.47 ± 0.20	89.71 ± 0.20	88.95 ± 0.28
<i>Stripping</i>	62.43 ± 0.52	73.75 ± 0.34	83.76 ± 0.61
Total	30.06 ± 0.22	34.01 ± 0.23	26.81 ± 0.22

Table 3.8: Trigger and stripping efficiencies in percent for signal models with a mass of 38 GeV/c² at $\sqrt{s} = 8$ TeV. The uncertainties are statistical. Hlt1, Hlt2 and Stripping is referring to Hlt1SingleMuonHighPTDecision, Hlt2SingleMuonHighPTDecision and StrippingLLP2MuXHighPTHHighIPMuonLine.

	<i>LV38,5ps</i>	<i>LV38,10ps</i>	<i>LV38,50ps</i>
<i>L0Muon</i>	81.53 ± 0.20	81.79 ± 0.20	81.50 ± 0.20
<i>Hlt1</i>	60.12 ± 0.28	56.35 ± 0.28	37.80 ± 0.27
<i>Hlt2</i>	80.66 ± 0.29	80.33 ± 0.30	79.50 ± 0.37
<i>Stripping</i>	52.61 ± 0.34	64.04 ± 0.42	71.37 ± 0.66
Total	20.80 ± 0.21	23.71 ± 0.22	17.48 ± 0.19

Table 3.9: Same as Table 3.8 for signal models with a mass of 98 GeV/c².

	<i>LV98,5ps</i>	<i>LV98,10ps</i>	<i>LV98,50ps</i>
<i>L0Muon</i>	84.28 ± 0.19	84.12 ± 0.19	84.25 ± 0.19
<i>Hlt1</i>	63.05 ± 0.27	60.53 ± 0.27	43.61 ± 0.28
<i>Hlt2</i>	84.50 ± 0.25	84.84 ± 0.26	84.85 ± 0.30
<i>Stripping</i>	56.23 ± 0.32	68.06 ± 0.40	77.88 ± 0.60
Total	25.25 ± 0.22	29.40 ± 0.23	24.28 ± 0.22

Table 3.10: Same as Table 3.8 for signal models with a mass of $198 \text{ GeV}/c^2$.

	$LV198, 5ps$	$LV198, 10ps$	$LV198, 50ps$
<i>L0Muon</i>	85.98 ± 0.17	86.02 ± 0.18	85.52 ± 0.18
<i>Hlt1</i>	63.53 ± 0.25	61.16 ± 0.26	43.25 ± 0.27
<i>Hlt2</i>	90.36 ± 0.20	90.45 ± 0.21	90.52 ± 0.25
<i>Stripping</i>	62.74 ± 0.31	74.94 ± 0.39	85.00 ± 0.61
Total	30.97 ± 0.24	35.66 ± 0.25	28.46 ± 0.23

3.3.2 Preliminary event selection (preselection)

The preselection initially identifies events with at least one muon firing the trigger and stripping lines, adding quality cuts to remove background coming from mis-identified muons or muons badly reconstructed. Then a displaced vertex is reconstructed with several tracks including the preselected muon. Global event cuts and a "Matter Veto" (MV) have been added to the vertex selection to discard "beam-splash" events and vertices produced by the particle interacting with the detector material. In the following two sections, the preselection criteria are described in details as well as the properties of the selected events.

3.3.2.a Muon preselection

In addition to a minimal transverse momentum and a minimal impact parameter required at the stripping level, loose quality cuts are applied. To discard kaons or pions punching through the calorimeters and being mis-identified as muons, the corresponding energy deposit in the calorimeters is considered. This selection is similar as that described in the $W \rightarrow \mu\nu$ analysis [43].

In summary, the muons selected at this stage have:

- $p_T^\mu > 12 \text{ GeV}/c$ (stripping)
- Impact parameter (Impact Parameter (IP)) of the muon with respect to the best PV : $IP > 0.25 \text{ mm}$ (stripping)
- Error on the muon momentum divided by the momentum: $\sigma(P^\mu)/P^\mu < 0.05$
- Quality of the muon track: $\chi^2/DoF < 2$
- $(E_{Ecal} + E_{Hcal})/P^\mu < 0.04$

Figure 3.7 shows the muon properties of events after trigger and stripping. The distribution from the 2011 dataset are compared to the MC signal model $LV38 \text{ } 10ps$ and to the $b\bar{b}$ simulated sample. The $b\bar{b}$ distributions and the data are very close. As discussed in Section 3.3.4, displaced muons with a poor isolation coming from $b\bar{b}$ events are the main source of background.

No stronger selection has been made on the muon isolation to preserve enough background events in a signal free region: this is necessary for the two signal determination techniques described in Section 3.4.

The distributions for 2011 and 2012 of different muon properties are compared on Figure 3.8 as well. Given the small difference in \sqrt{s} the distributions coincide.

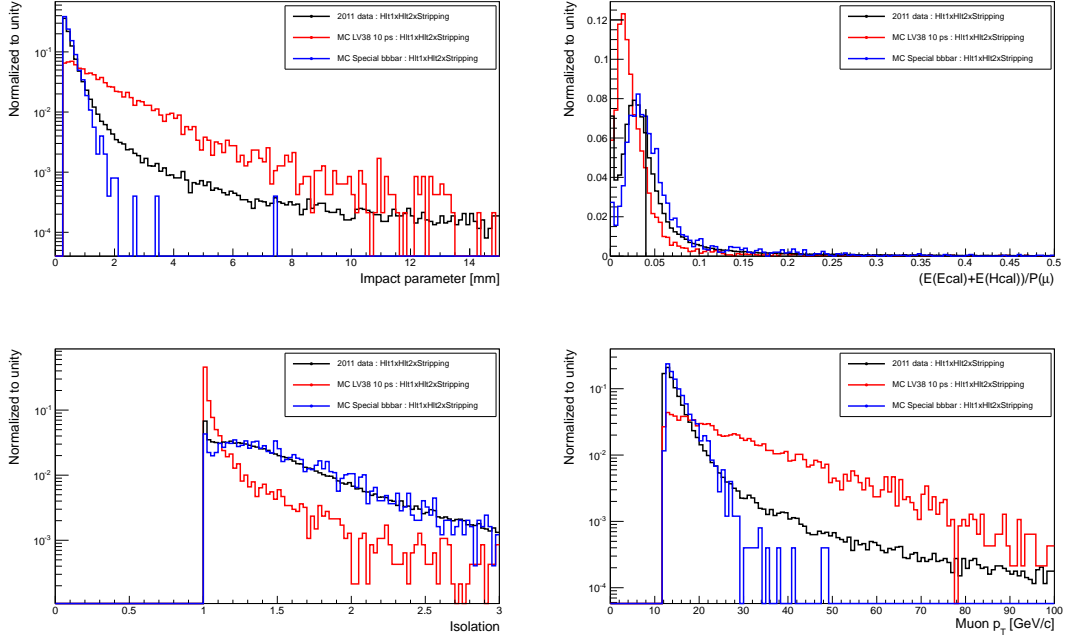


Figure 3.7: Distributions of the muon variables for the 2011 dataset, compared to simulated $b\bar{b}$ and to the MC signal $LV38$ 10 ps, for events after trigger and stripping. Top left: Muon impact parameter with respect to the best primary vertex. Top right : $E(Ecal)/P^\mu + E(Hcal)/P^\mu$. Bottom left : Muon isolation. Bottom right : muon transverse momentum. The distributions are normalized to unity.

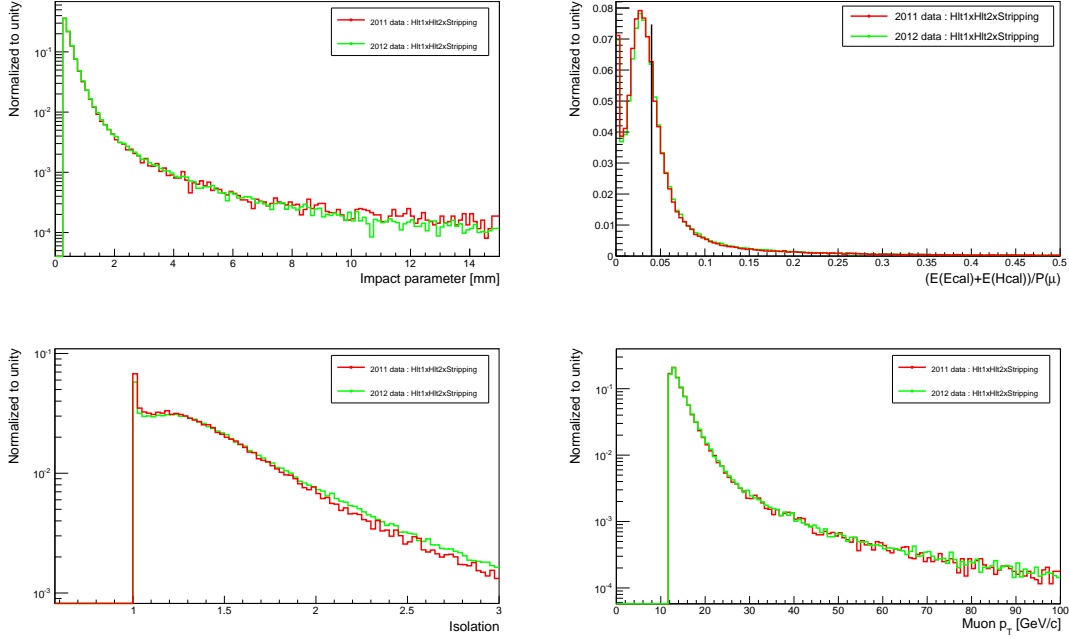


Figure 3.8: Like Figure 3.7, comparison between 2011 and 2012 data.

3.3.2.b The reconstruction of primary and secondary vertices

This section presents the procedure implemented to identify secondary vertices in the event. This algorithm is the same used for the search for Higgs-like bosons decaying into a pair of long-lived exotic particles but tuned for this specific analysis, as originally presented in [6].

The same sequence of algorithms is used for Primary Vertices (PV), and for secondary vertices reconstruction. The two consecutive steps executed to select Reconstructed Vertices (Reconstructed Vertices (RV)) are summarized hereby. The algorithms rely on fully reconstructed tracks.

In the first step an algorithm (**PVSeed3DTool**) creates *seeds* by looking for points in the VELO with a sufficient number of tracks passing close to each others. It starts from a track, called *base track*, and determines the number of tracks with a distance of closest approach (Distance of Closest Approach (DOCA)) smaller than 0.3 mm. If the number of close tracks is smaller than 4, another base track is considered. Then, for every track pair, the average point of closest approach (Point of Closest Approach (POCA)) is calculated and an average is made in a two-steps procedure. POCA with distance larger than 3 mm to the mean are removed and the calculation is done again. A weight is then associated to each POCA entry, taking typical track parameter errors and opening angle of the track into account. When the number of close tracks with maximal z spread distance exceeds the minimal number of close tracks required, the *seed* is accepted. The tuning of this procedure is designed to maximize the efficiency, allowing for some fake seeds. This have been proven not to affect much the performance of the PV reconstruction [44]. The second step consists on an adaptive least square fit performed by **LSAdaptPV3DFitter** from the combination of *seeds*. The procedure has been developed to avoid systematic shifts of the PV due to a fraction of badly measured tracks (ghosts and multiple scattering effects). An adaptive weight least square method, the Tukey biweight method, is used to assign a $(1 - \chi_{IP}^2/C_T^2)^2$ weight to a track according to its χ_{IP}^2 . C_T is the Tukey constant. The procedure requires a minimum number of tracks (generally 5 for primary and 3 for displaced vertices) with a maximum χ^2 (typically 9) and a minimum track weight of 1×10^{-8} . Afterwards, tracks that have a maximum χ^2 larger than 25 are removed from the list used for further vertex searches. It has to be noticed that the online version relies on straight-line extrapolation of tracks and makes less use of tracks uncertainties. This results in a poor efficiency for vertices further than 200 mm of the interaction point, very weakly affecting the detection efficiency for the models considered in this work (compare to Figure 3.5, for instance). The selection of the PVs is done by requiring for each candidate:

- at least 10 tracks
- at least one forward track and one backward track
- a radial distance not larger than 0.3 mm from the reconstructed beam position, and $|z| < 400$ mm.

3.3.2.c Displaced vertex preselection

Once the set of PVs identified, all the other RVs are candidates for the decay position of LLPs. The beam-line position is given by the VELO position in the beginning of each run. The position recorded in 2011 data is illustrated in Figure 3.9, showing an average displacement in the x coordinate of 0.46 mm (0.61 mm for 2012 data).

The event preselection requires at least one PV in the event and at least one LLP candidate with:

- at least 4 forward tracks including the preselected muon;
- no backward tracks;
- an invariant reconstructed mass from tracks larger than $4.5 \text{ GeV}/c^2$;
- The MV is activated to reconstruct LLP candidates outside the detector material. The Matter-Veto is a geometrical cut which removes vertices falling inside the detector structure as described in Appendix C of [6];

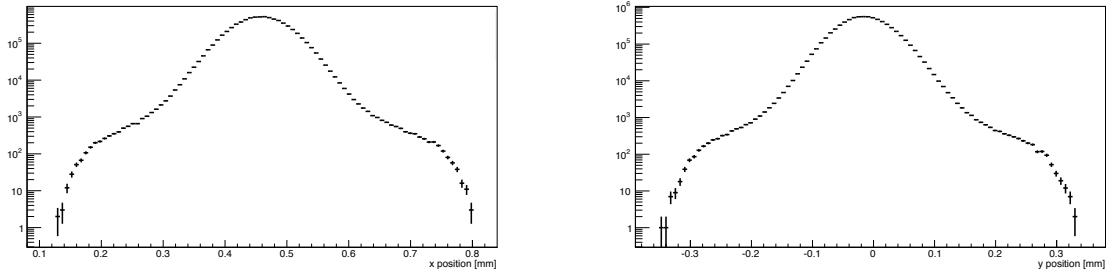


Figure 3.9: x and y positions of the reconstructed primary vertices obtained after the $R < 0.3 \text{ mm}$ cut for 2011 data.

3.3.3 Properties of the selected vertices, the matter veto

Figures 3.10 and 3.11 show the distributions of the longitudinal and of the radial position of the RVs, and Figure 3.12 the (x,z) scatter plot with and without MV. The position of the detector material is clearly visible: the region beyond $R \sim 5 \text{ mm}$ is heavily polluted by the products of particles interacting with matter. The MV procedure removes such background discarding RVs falling in the detector material.

Chapter 3. Search for long-lived particles decaying semileptonically

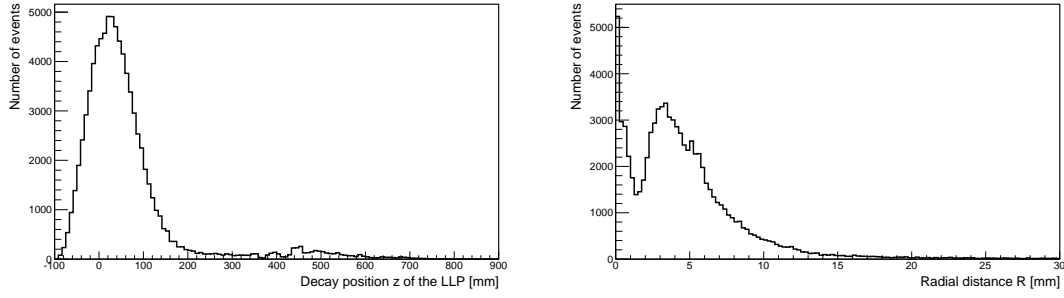


Figure 3.10: From preselected 2011 data, the longitudinal (left plot) and radial (right plot) coordinates (lab frame) of the reconstructed secondary vertices with at least four forward tracks including the preselected muon, no backward tracks, and an invariant mass larger than $4.5 \text{ GeV}/c^2$ without MV.

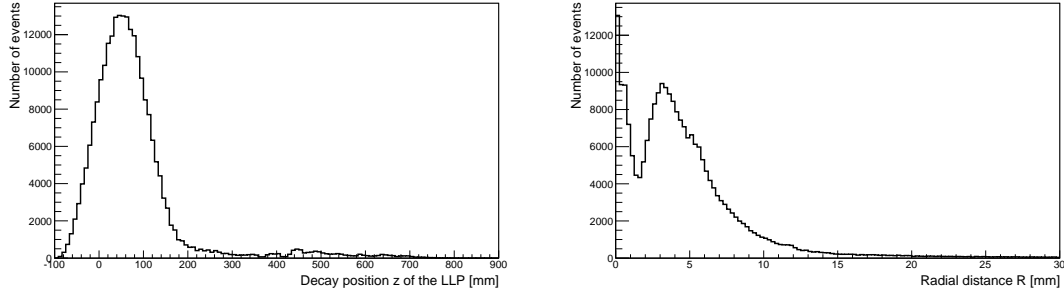


Figure 3.11: Like Figure 3.10, for preselected 2012 data.

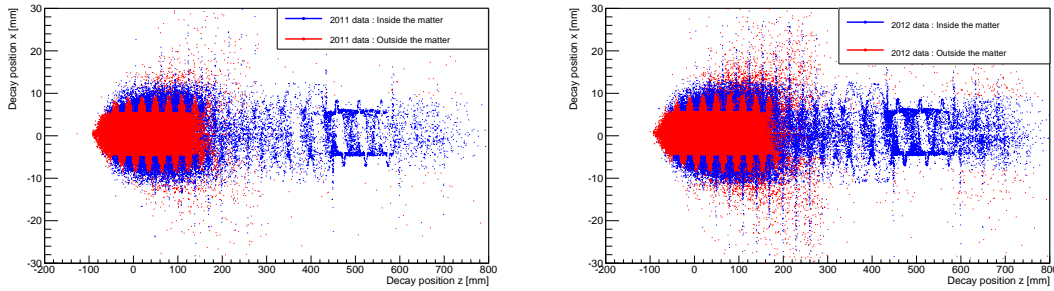


Figure 3.12: Like Figure 3.10, position of the reconstructed vertices in coordinates (x, z) (lab frame). The data are presented by categorizing events kept after the MV procedure (in red) and events removed by the MV (in blue). Left: from the 2011 dataset. Right: from the 2012 dataset.

As discussed in [6] and [5], special "global event cuts" have been set to remove events coming from interactions of the beam-halo with the material upstream or downstream of the VELO that increases the number of fake RVs at large distance from the beam. This effects is known as "beam-splash" events.

First, a cut is requiring that the number of VELO tracks does not exceed one-tenth of the number of VELO clusters to avoid too much near-parallel tracks reconstructed from the large number of hits in the polluted region. Secondly, as the hits associated to the beam-splash particles are close in ϕ in the VELO, a vector sum in the transverse plane has been defined:

$$D_\phi = \sum_{\phi \text{ hits } i} \begin{pmatrix} \cos \phi_i \\ \sin \phi_i \end{pmatrix} \quad (3.1)$$

where the sum runs over all hits in VELO ϕ -strips and ϕ_i is the direction of the strip. The distributions of the quantity is illustrated in Figure 3.13. To reject beam-splash events we require that $\|D_\phi\| < 250$. The selection leaves the signal efficiency quasi unmodified.

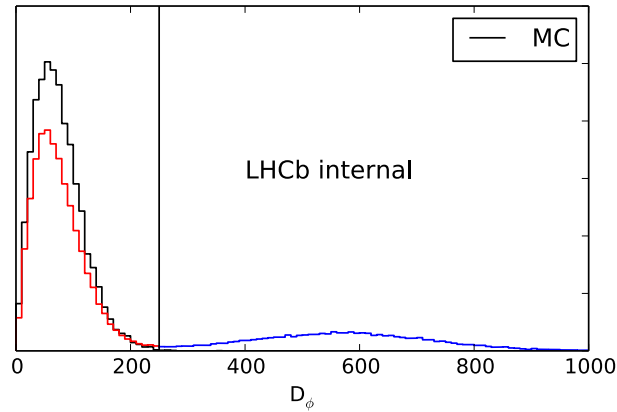


Figure 3.13: Distribution of $\|D_\phi\|$ in simulated events (black) and 2011 data selected for the displaced vertex analysis (red and blue). The vertical line corresponds to the cut applied in the analysis.

After applying the MV filter, most of the structure has disappeared but not completely, most likely because of reconstruction errors, as shown on Figure 3.14. Note that at this point of the analysis no minimal radial distance to the beam line is applied. The vertex reconstruction efficiency has been tested on $B^0 \rightarrow J/\psi K^{*0}$ events and the discrepancy between data and Monte Carlo have been taken into account as a systematics effect on the selection efficiency for the different signal models. This study is presented on Section 3.5.2.

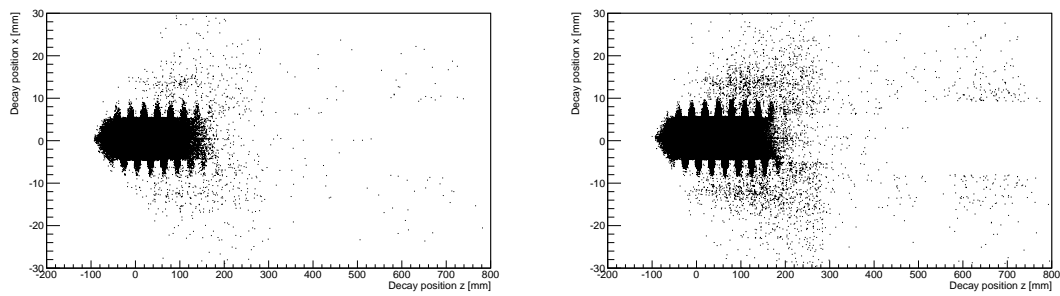


Figure 3.14: Like Figure 3.12 but for events selected after the MV procedure. Left: 2011 dataset. Right: 2012 dataset.

3.3.4 Situation after the preselection, background studies

In this section, the properties of the preselected and MV filtered events are presented. The results are compared to the background and signal predictions.

The number of events after the displaced vertex reconstruction are shown on Table 3.11 for the 2011 and 2012 datasets. The number of events with positive and negative muon candidates are also given. The number of expected events for the different simulated background samples are also given in the table for the year 2011. Table 3.12 shows that less than 1 % of events have more than one candidate in data and also in the background sets. 4–5% of the signal events contain more than one candidate. In the following, when more than one candidate is present in the event, the one with the highest p_T muon is chosen.

Table 3.11: Number of preselected events for each background MC sample, $\sqrt{s} = 7$ TeV, $\sqrt{s} = 8$ TeV, and the number of expected background events in 2011. The values for LV38 10 ps are also reported. The last line is for the 2012 dataset.

Sample	Generated	N (μ^+)	N (μ^-)	Total	Expected ($0.98 fb^{-1}$)
LV38 10 ps	45 k	1124	1070	2194	
Special $b\bar{b}$	214.4 k	75	90	165	18147 ± 3566
$W \rightarrow \mu\nu$	5 M	911	617	1528	539 ± 60
$Z \rightarrow \mu\mu$	2.0 M	194	192	386	52 ± 6
$W \rightarrow \tau\nu$	5 M	39	16	55	19 ± 4
$Z \rightarrow \tau\tau$	1.05 M	13	8	21	5 ± 2
$t\bar{t}$	509.6k	2	3	5	< 0.1
2011 data		10945	10551	21496	$(18.8 \pm 3.6) \cdot 10^3$
2012 data		30667	30211	60878	

Table 3.12: Fraction of events with more than one candidate.

Sample	Fraction
LV models ($\sqrt{s} = 7 TeV$)	(3.6 – 5.5) %
LV models ($\sqrt{s} = 8 TeV$)	(3.9 – 6.1) %
Special $b\bar{b}$, W and Z	< 1 %
2011 and 2012 data	< 1 %

The observed asymmetry between μ^+ and μ^- in the $W \rightarrow \mu\nu$ events results from the production processes of the W bosons dominated by $u\bar{d}(\bar{u}d) \rightarrow W^+(W^-)$. Therefore, the production cross-section is larger for W^+ in pp collisions because of the proton valence quark composition (two quarks u and one quark d).

The $(18.8 \pm 3.6) \cdot 10^3$ background events predicted are compatible with the number of events

recorded in 2011. As expected, the background is highly dominated by $b\bar{b}$ events (QCD background) with a small contributions from W and Z bosons. We remember that the special $b\bar{b}$ sample has been generated with a $\hat{p}_T > 20$ GeV/c required to increase the probability to find a high p_T muon in the b-hadron decays. In the following, the numerical value of this prediction is not used because the background yield will be estimated from the data itself. Only the background distribution shapes will be used as prototypes.

The prediction for the 2012 dataset is obtained by considering a cross-section 20% larger than the corresponding value at 7 TeV. $(44.1 \pm 8.8) \cdot 10^3$ $b\bar{b}$ events at $\sqrt{s} = 8$ TeV are estimated, close to the 60.8k events observed.

On Figure 3.15 and 3.16, several distributions of the preselected events are presented for the 2011 dataset in comparison with the different sources of background. As an example of signal, the distribution of $LV38(\tau = 10$ ps) is displayed as well.

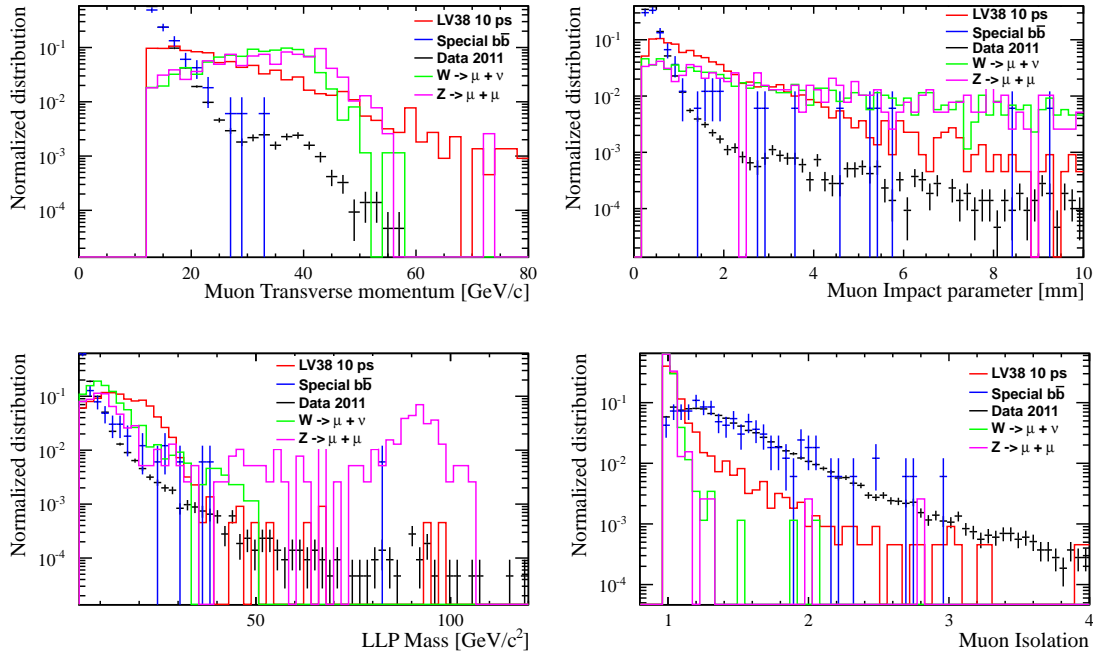


Figure 3.15: Distributions from 2011 data compared to simulated events, after preselection. Top left: muon transverse momentum Top right: the muon impact parameter with respect to the best primary vertex. Bottom left: the reconstructed mass of the displaced vertex computed with the outgoing tracks. Bottom right: muon isolation. The distribution are normalized to unity.

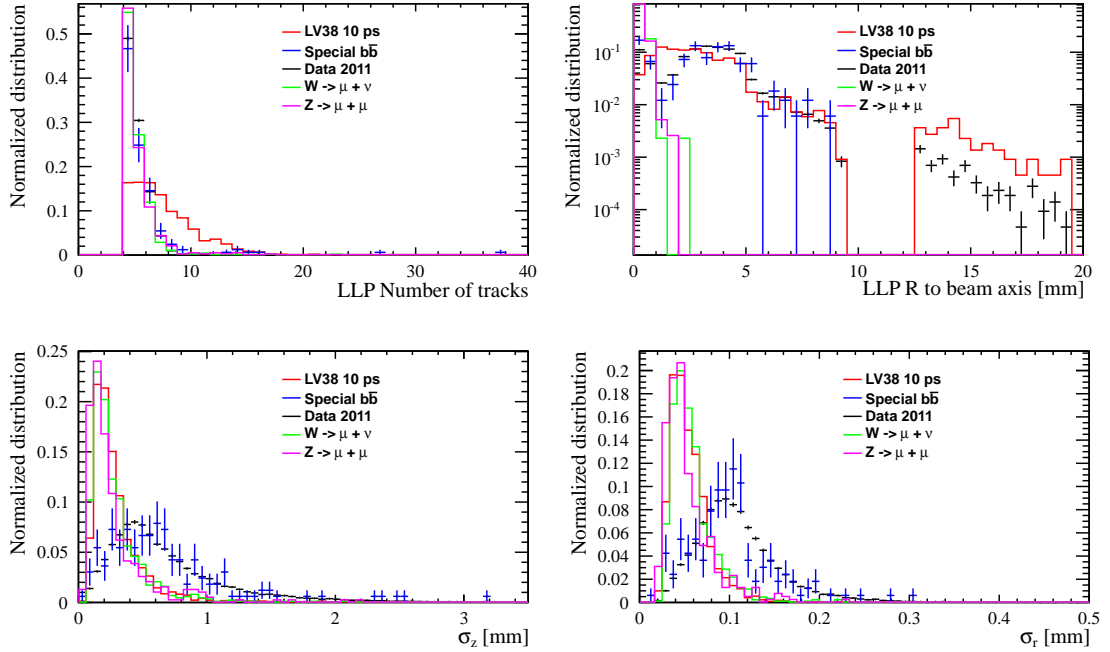


Figure 3.16: Distributions from 2011 data compared to simulated events, after preselection. Top left: the number of tracks that have been used to reconstruct the vertex including the muon. Top right: the radial distance R to the beam line of the reconstructed vertex. Bottom left: the longitudinal vertex fit error. Bottom right: the radial vertex fit error. The distribution are normalized to unity.

From Figure 3.15, we see that the majority of the signal has an isolation variable peaked at 1 which is not the case for tracks from b hadrons. This effect is also highlighted on the plots of the vertex fit radial and longitudinal errors provided by the vertex reconstruction algorithm. Light boosted particles will produce close parallel tracks, producing a worse fit quality than the vertex reconstructed with more diverging tracks from a heavier particles. It is important to note that at this stage of the analysis no selections has been applied on the radial distance R of the reconstructed LLP vertex from the beam line.

The background can be divided in two categories, taking the muon isolation and the LLP vertex radial distance as parameters:

- Displaced vertex reconstructed with a non-isolated muon: mainly the QCD background,
- Prompt and well isolated muons are the signature of W or Z decays.

The background associated to W or Z bosons can be easily removed by asking a minimal value of R . Choosing $R > 0.55 \text{ mm}$, the results of Table 3.14 are obtained. In practice only $b\bar{b}$ events remain after this selection. On Figure 3.19 and 3.20, simulated $b\bar{b}$ events are compared to the 2011 data after the minimal displacement requirement. The distributions are consistent with a pure $b\bar{b}$ background.

Chapter 3. Search for long-lived particles decaying semileptonically

On table 3.14, the selection criteria applied at this stage of the analysis are summarized. The contributions of the different step of the analysis to the selection efficiency are presented on Table 3.15, 3.16 and 3.17 for the different signal models considered at $\sqrt{s} = 7$ TeV (2011) and on table 3.18, 3.19 and 3.20 for $\sqrt{s} = 8$ TeV (2012). The statistics for the 2011 and 2012 datasets are given in Table 3.21.

Figures 3.17 and 3.18 compares the distributions from the 2011 datasets to the same from the 2012 dataset. No substantial difference is visible.

Table 3.13: Number of events after the radial cut ($R > 0.55$ mm) in data and in the simulated sets, for 2011. The results from the 2012 dataset are also given.

Sample	Generated	Total	Expected (2011)
LV38 10 ps	45 k	2083	
Special $b\bar{b}$	214.4 k	135	14848 ± 3297
$W \rightarrow \mu\nu$	5M	11	4 ± 2
$Z \rightarrow \mu\mu$	2.0M	5	2 ± 1
$W \rightarrow \tau\nu$	5M	3	1 ± 1
$Z \rightarrow \tau\tau$	1.05M	3	1 ± 1
$t\bar{t}$	509.6k	0	< 0.01
2011 data		18925	14852 ± 3297
2012 data		53331	

Table 3.14: Summary of the preselection criteria.

	Variable	Value
Muon preselection	p_T^μ	> 12 GeV/c
	IP_μ	> 0.25 mm
	χ^2/DoF of the μ track	< 2
	$\sigma(P^\mu)/P^\mu$	< 0.05
	$\frac{E(Ecal(\mu))}{p^\mu} + \frac{E(Hcal(\mu))}{p^\mu}$	< 0.04
Displaced vertex preselection	N^{track} including μ	≥ 4
	m_{LLP} reconstructed	≥ 4.5 GeV/c ²
	Backward tracks	No
	MV	active
	Number of PV upstream of the RV	≥ 1
Additional selection (intermediate)	R to the beam line	≥ 0.55 mm

Table 3.15: Summary of the selection efficiencies (in percent) at the the different stage of the analysis for model with a LV model with a neutralino mass of $38 \text{ GeV}/c^2$ at $\sqrt{s} = 7 \text{ TeV}$ (2011).

Selection stages	$LV38, 5ps$	$LV38, 10ps$	$LV38, 50ps$
Generator cut	11.08 ± 0.10	11.09 ± 0.07	11.30 ± 0.11
Trigger and Stripping selection	18.42 ± 0.19	22.02 ± 0.20	16.72 ± 0.18
Displaced Vertex Reconstruction	48.07 ± 0.56	50.95 ± 0.52	51.07 ± 0.59
MV	86.93 ± 0.55	79.37 ± 0.59	65.39 ± 0.79
Muon quality cuts	81.00 ± 0.68	79.75 ± 0.66	80.15 ± 0.81
$R > 0.55 \text{ mm}$	93.81 ± 0.47	95.74 ± 0.37	97.09 ± 0.38
Total	0.65 ± 0.03	0.75 ± 0.04	0.49 ± 0.02

Table 3.16: Summary of the selection efficiencies (in percent) at different stage of the analysis for signal models with a neutralino mass of $98 \text{ GeV}/c^2$ at $\sqrt{s} = 7 \text{ TeV}$ (2011).

Selection stages	$LV98, 5ps$	$LV98, 10ps$	$LV98, 50ps$
Generator cut	11.00 ± 0.08	11.30 ± 0.19	11.08 ± 0.10
Trigger and Stripping selection	23.01 ± 0.23	27.67 ± 0.21	23.24 ± 0.20
Displaced Vertex Reconstruction	34.77 ± 0.54	37.48 ± 0.44	38.02 ± 0.49
MV	96.22 ± 0.37	91.50 ± 0.42	76.06 ± 0.69
Muon quality cuts	85.52 ± 0.70	86.22 ± 0.54	85.89 ± 0.64
$R > 0.55 \text{ mm}$	85.35 ± 0.75	89.96 ± 0.50	93.84 ± 0.57
Total	0.61 ± 0.03	0.81 ± 0.04	0.60 ± 0.03

Table 3.17: Like 3.16, for a neutralino mass of $198 \text{ GeV}/c^2$ at $\sqrt{s} = 7 \text{ TeV}$ (2011).

Selection stages	$LV198, 5ps$	$LV198, 10ps$	$LV198, 50ps$
Generator cut	11.07 ± 0.10	11.12 ± 0.10	11.14 ± 0.05
Trigger and Stripping selection	30.06 ± 0.22	34.01 ± 0.23	26.81 ± 0.22
Displaced Vertex Reconstruction	25.61 ± 0.58	27.52 ± 0.37	28.95 ± 0.43
MV	99.04 ± 0.17	95.20 ± 0.34	78.79 ± 0.72
Muon quality cuts	87.88 ± 0.56	87.64 ± 0.53	87.46 ± 0.65
$R > 0.55 \text{ mm}$	83.83 ± 0.67	88.91 ± 0.54	95.04 ± 0.49
Total	0.62 ± 0.02	0.76 ± 0.03	0.56 ± 0.02

Table 3.18: Like 3.16, for a neutralino mass of $38 \text{ GeV}/c^2$ at $\sqrt{s} = 8 \text{ TeV}$ (2012).

Selection stages	$LV38, 5ps$	$LV38, 10ps$	$LV38, 50ps$
Generator cut	12.15 ± 0.09	12.17 ± 0.10	12.34 ± 0.11
Trigger and Stripping selection	20.80 ± 0.21	23.71 ± 0.22	17.48 ± 0.66
Displaced Vertex Reconstruction	51.85 ± 0.56	56.25 ± 0.52	55.49 ± 0.60
MV	84.97 ± 0.55	77.15 ± 0.59	64.11 ± 0.78
Muon quality cuts	79.93 ± 0.68	78.90 ± 0.65	78.20 ± 0.84
$R > 0.55 \text{ mm}$	95.22 ± 0.40	96.60 ± 0.32	97.36 ± 0.38
Total	0.84 ± 0.02	0.95 ± 0.02	0.58 ± 0.01

Table 3.19: Like 3.16, for a neutralino mass of $98 \text{ GeV}/c^2$ at $\sqrt{s} = 8 \text{ TeV}$ (2012).

Selection stages	$LV98, 5ps$	$LV98, 10ps$	$LV98, 50ps$
Generator cut	12.09 ± 0.10	12.07 ± 0.10	12.22 ± 0.08
Trigger and Stripping selection	25.25 ± 0.22	29.40 ± 0.23	24.28 ± 0.22
Displaced Vertex Reconstruction	40.62 ± 0.50	43.78 ± 0.47	43.04 ± 0.52
MV	96.27 ± 0.30	89.90 ± 0.43	76.03 ± 0.69
Muon quality cuts	85.77 ± 0.57	85.65 ± 0.53	84.67 ± 0.66
$R > 0.55 \text{ mm}$	86.04 ± 0.61	90.57 ± 0.47	95.05 ± 0.43
Total	0.88 ± 0.02	1.09 ± 0.02	0.78 ± 0.02

Table 3.20: Like 3.16, for a neutralino mass of $198 \text{ GeV}/c^2$ at $\sqrt{s} = 8 \text{ TeV}$ (2012).

Selection stages	$LV198, 5ps$	$LV198, 10ps$	$LV198, 50ps$
Generator cut	12.07 ± 0.11	12.24 ± 0.11	11.81 ± 0.10
Trigger and Stripping selection	30.97 ± 0.24	35.66 ± 0.25	28.46 ± 0.23
Displaced Vertex Reconstruction	31.89 ± 0.43	34.72 ± 0.41	34.51 ± 0.46
MV	98.77 ± 0.18	94.34 ± 0.34	78.37 ± 0.67
Muon quality cuts	87.50 ± 0.54	88.09 ± 0.49	87.27 ± 0.62
$R > 0.55 \text{ mm}$	83.28 ± 0.66	90.15 ± 0.48	95.62 ± 0.40
Total	0.86 ± 0.02	1.13 ± 0.02	0.76 ± 0.02

Table 3.21: Number of events selected at each selection stages, for the 2011 and 2012 datasets.

Selection stages	2011 data	2012 data
Stripping selection	4.9 <i>M</i>	12.0 <i>M</i>
Muon quality cuts	1.8 <i>M</i>	4.3 <i>M</i>
Displaced Vertex Reconstruction	28890	82108
MV	21496	60878
$R > 0.55$ mm	18925	53331

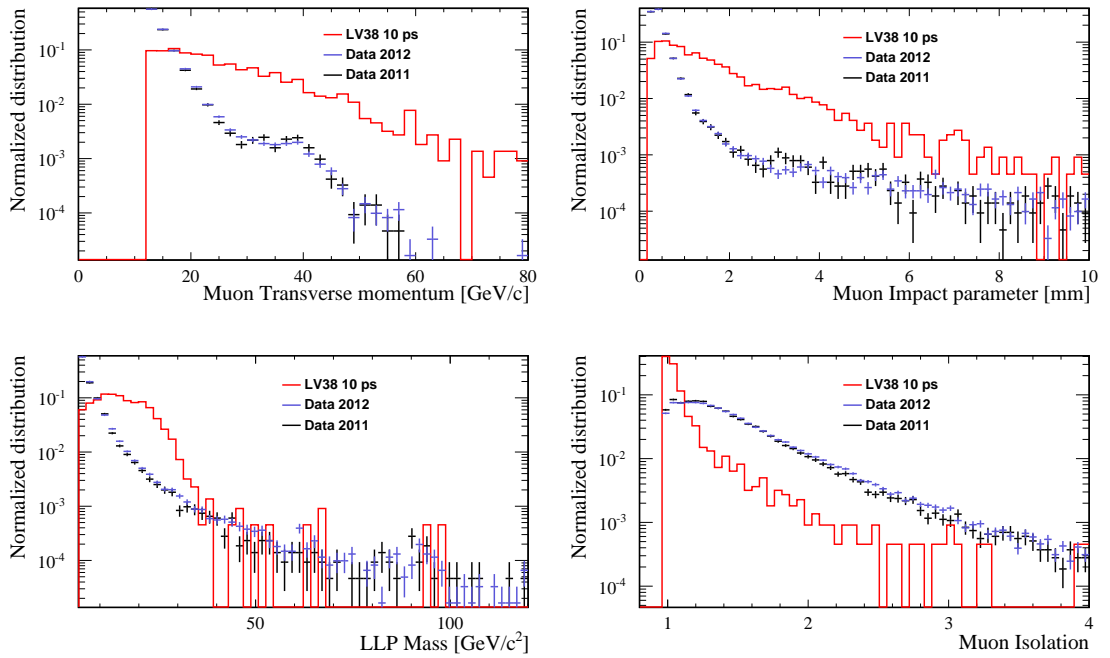


Figure 3.17: Same as Figure 3.15 but for the comparison of the 2011 and 2012 datasets. LV38 10 ps is also show for comparison.

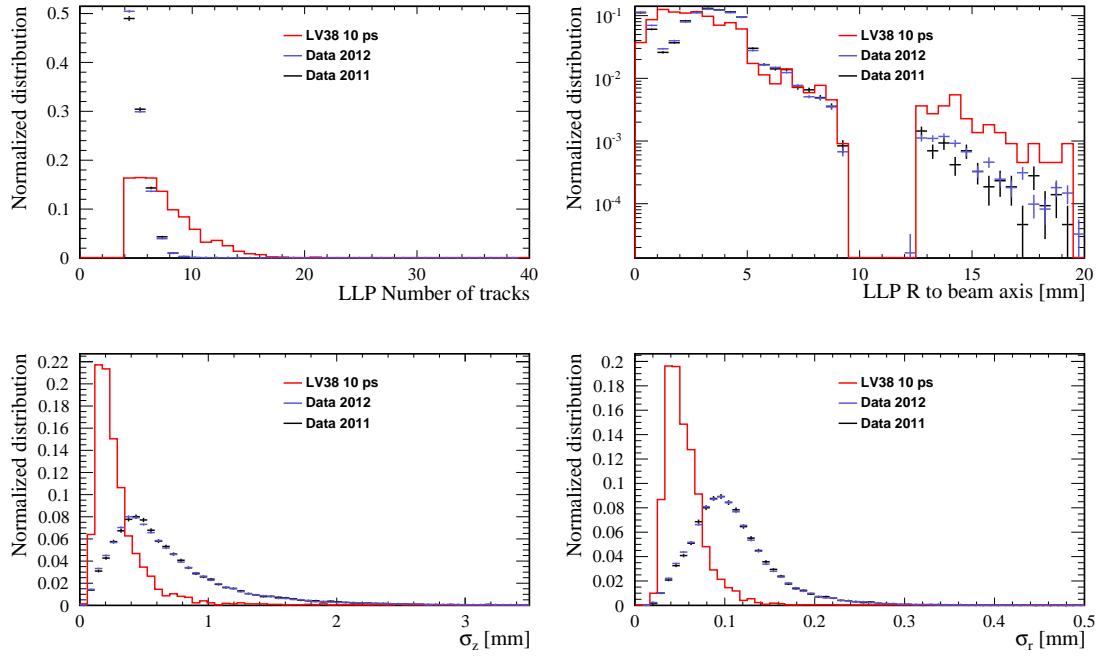


Figure 3.18: Same as Figure 3.16 but for the comparison of the 2011 and 2012 datasets. *LV38 10 ps* is also show for comparison.

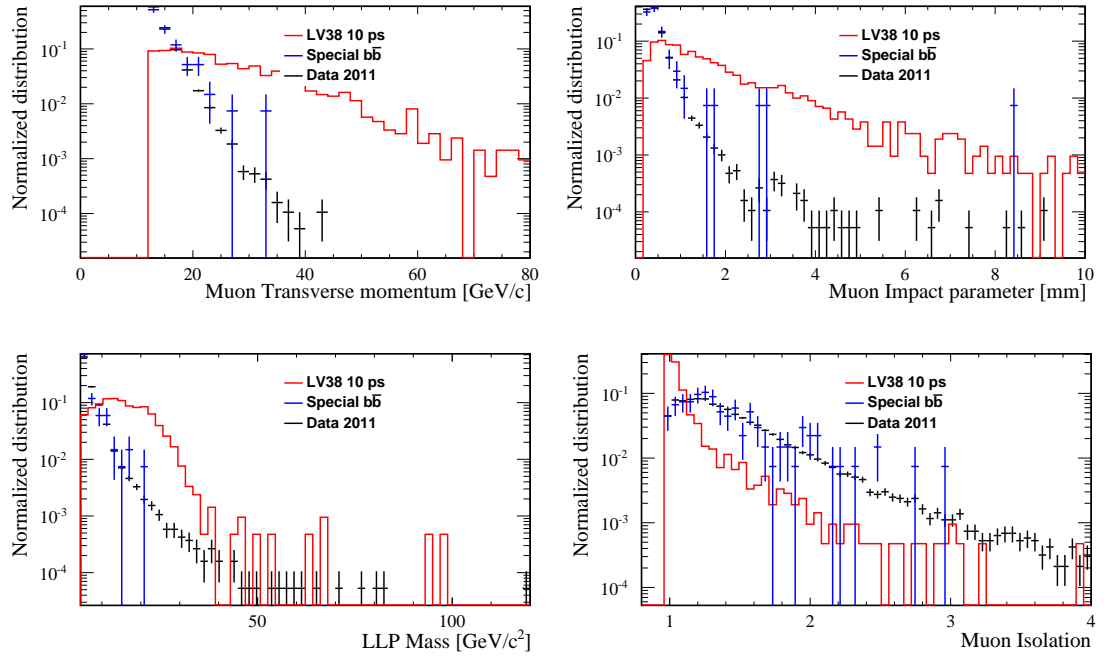


Figure 3.19: 2011 data compared to simulated $b\bar{b}$ events after the requirement of a minimal distance R to the beam axis of 0.55 mm . Top left: muon transverse momentum. Top right: muon impact parameter with respect to the best primary vertex. Bottom left: reconstructed mass of the displaced vertex. Bottom right: muon isolation. The distributions are normalized to unity.

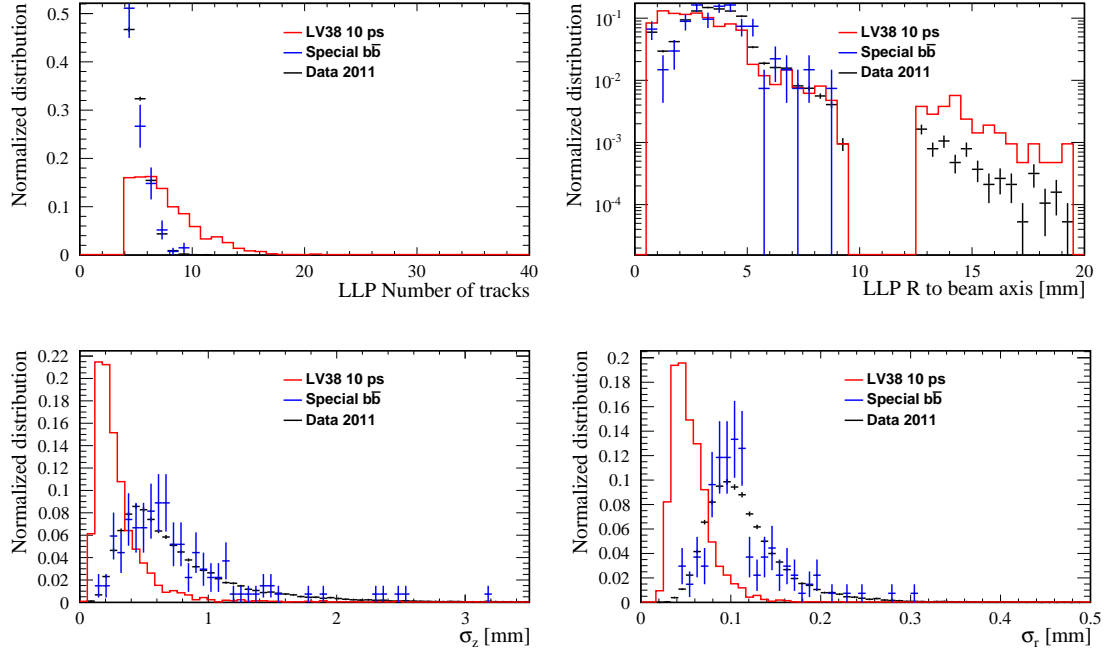


Figure 3.20: 2011 data compared to simulated $b\bar{b}$ events after the requirement of a minimal distance R to the beam axis of 0.55 mm . Top left: number of tracks used to reconstruct the vertex including the muon. Top right: radial distance R to the beam line of reconstructed vertex. Bottom left: longitudinal vertex fit error. Bottom right: radial vertex fit error. The distribution are normalized to unity.

3.3.5 Neural Network

After the minimal displacement requirement, a multi-layer perceptron (MLP) neural network is used to purify the events. The MLP is an option of the Toolkit for Multivariate Data Analysis (TMVA version 4.2.0) [45].

The MLP input variables are the following:

- PT_MUON: the muon transverse momentum,
- IP_MUON: the muon impact parameter with respect to the best PV,
- N_LLQ: number of charged tracks used to reconstruct the LLP,
- R_LLQ: LLP radial distance from the beam line,
- SIGMA_R_LLQ: uncertainty on the radial coordinate of the vertex fit,
- SIGMA_Z_LLQ: uncertainty on the longitudinal coordinate of the vertex fit,

The muon isolation (ISO_MUON) and the reconstructed mass of the long-lived particles (M_LLQ) are not included in the neural network classifier. Indeed, the discrimination power of these two variables is subsequently exploited in the two data driven signal determination methods.

The training of the MLP requires samples of signal and background events. Signal events are easily provided by the simulation. This is not the case for the background because, of the too low simulated $b\bar{b}$ statistics available. To cope with this, the data itself has been used to represent the background. The hypothesis is that the amount of signal in the dataset is small. Half of the Monte Carlo sample of signal events have been used for the training stage in addition with the same amount of data events. This procedure has been reproduced for each signal model. As an example, the input variables distributions are presented on Figure 3.21 for the 2011 data and for the LV38 ($\tau = 10$ ps) signal model. On Figure 3.22 the transformation of the variables into gaussian distributions after the "decorrelation" phases are illustrated for LV38 ($\tau = 10$ ps). On Figure 3.23 the linear correlation between the input variables are shown for the signal and the background (2011 data). In addition, the muon isolation (ISO_MUON) and the reconstructed mass (M_LLQ) have been added as "spectator variable" (i. e. not used for the selection) to highlight the low correlation between these two variables.

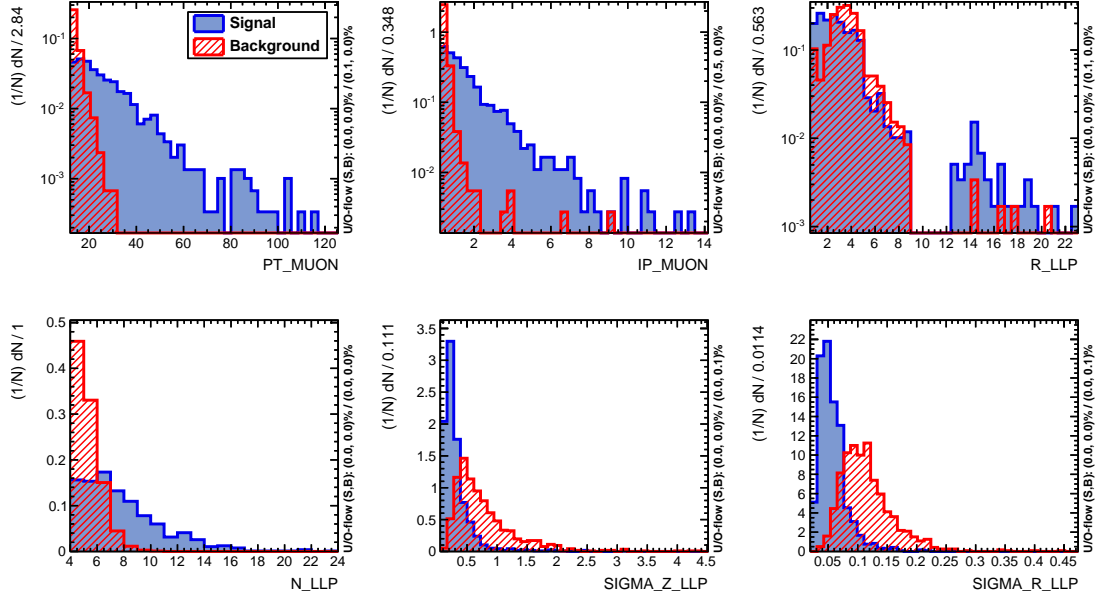


Figure 3.21: Input variables distributions of the multi-layer perceptron (MLP) neural network for the signal (LV38 ($\tau = 10$ ps)) and the background model (2011 data).

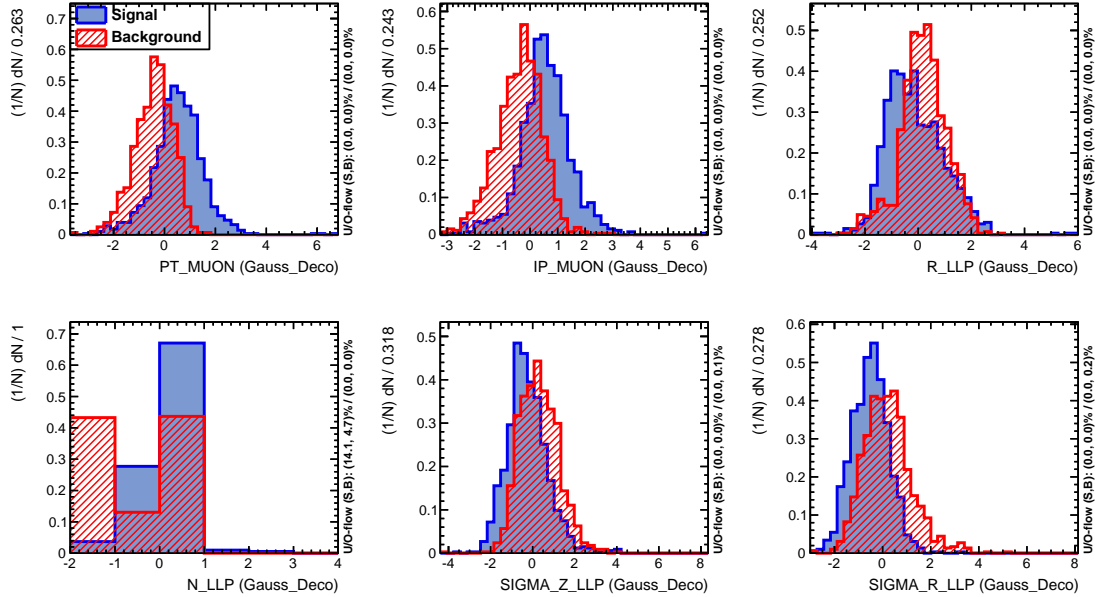


Figure 3.22: Distributions of the MLP input variables for the signal (LV38 ($\tau = 10$ ps)) and the background transformed into gaussian distributions after the decorrelation phase that take into account the linear correlation between each variables.

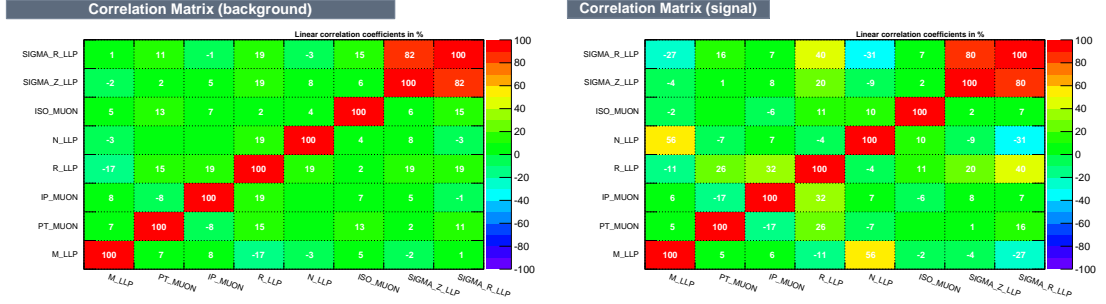


Figure 3.23: Linear correlation coefficient matrix for signal events (LV38 ($\tau = 10$ ps)) and background events computed by TMVA for the input and spectator variables. Note the low correlation between muon isolation and the LLP reconstructed mass.

The MLP is using a "sigmoid" activation function type trained with a Back-Propagation (Back Propagation (BP)) algorithm with a number of cycles of N_{cycles} and 5 hidden layers. On Figure 3.24 the convergence and the overtraining tests are presented. The test sample for the background is defined by the data selected at the intermediate selection stage without the $2k$ events used for the training phase. The error on the estimator converged after 600 training epochs. The distributions of the MLP response for the training and the test samples coincide showing no overtraining effects.

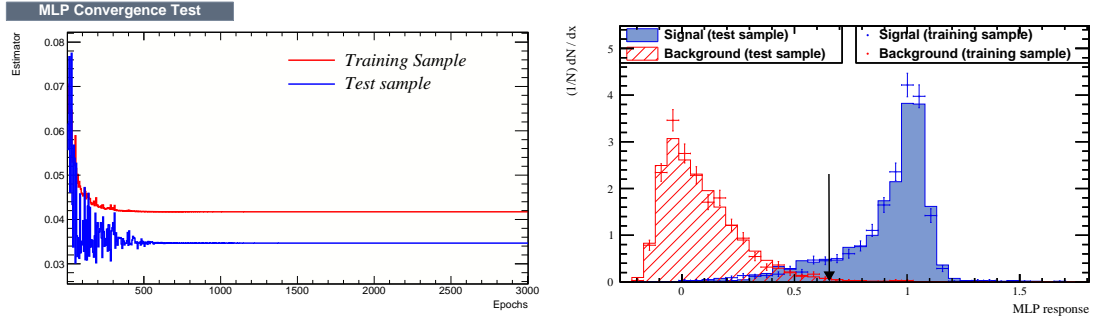


Figure 3.24: Convergence and overtraining tests : (left) error on the estimator as a function of the number of epochs (cycles) and (right) MLP response distributions of the trained and test sample for signal (LV38 ($\tau = 10$ ps)) and background (2011 data).

To quantify the potential bias induced by a "contamination" of the background sample by signal events, a large fraction of signal events (2.5 to 5 %) are added to the background data set used for the MLP training. As shown on Figure 3.26, no significant bias from a possible contamination by signal events is expected for a reasonable cut on the neural network response (MLP cut). The same conclusion has been reached for all signal model and for the two datasets (the corresponding plots are present on in Appendix A.4).

The optimal MLP cut has been determined by maximising the significance defined by $\hat{S} =$

$S/\sqrt{(S+B)}$ with a hypothetical presence of 5 signal events. For LV38 ($\tau = 10$ ps), a maximal significance of 0.336 is obtained when cutting at 0.65 on the MLP output as presented on Figure 3.25. The background rejection obtained by this selection also allows to keep enough background events which are required for the signal determination procedure.

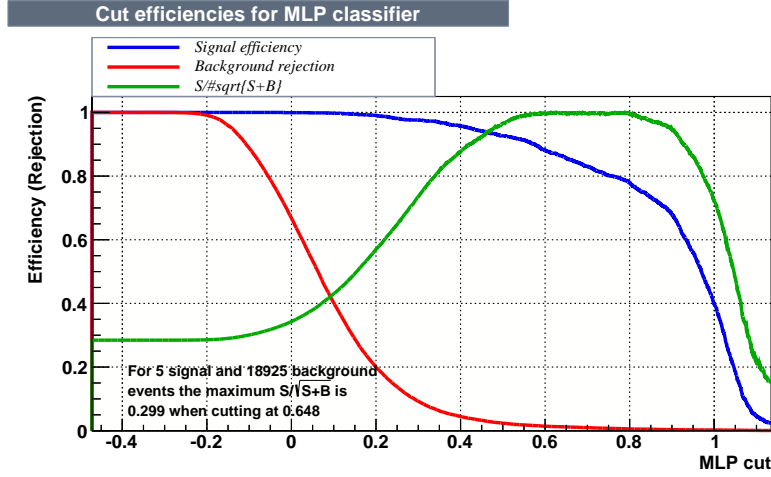


Figure 3.25: Signal significance, signal efficiency and background rejection as a function of the MLP cut for LV38 ($\tau = 10$ ps).

Thus, depending on the signal model analyzed, a cut on the MLP response between 0.48 and 0.65 for 2011 data and between 0.55 and 0.85 for 2012 has been applied. The signal and background MLP responses for each signal models for 2011 and 2012 analysis are presented on Appendix A.3.

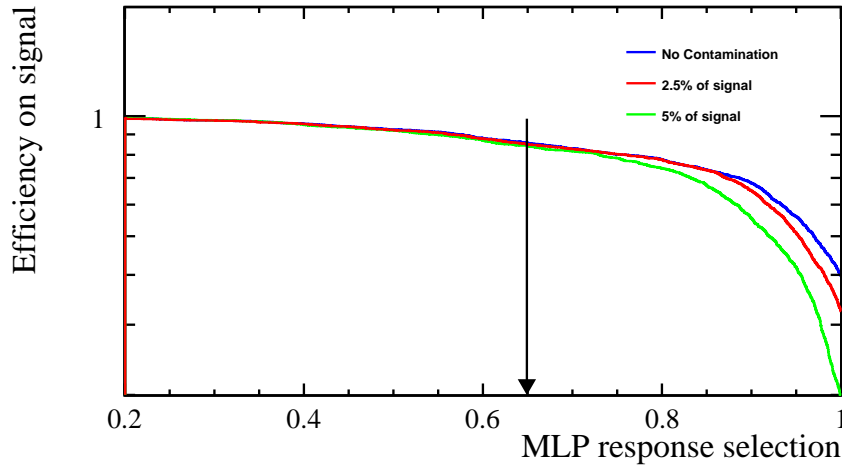


Figure 3.26: Signal (LV38 ($\tau = 10$ ps)) efficiency as a function of the MLP response for different fraction of signal event added to the background model (2011 data) at the training stage.

3.4 Signal determination

After the MLP filter no simulated background survives. Therefore two data driven methods have been used to estimate the residual background : The first, described in Section 3.4.1, is an extended likelihood fit of the reconstructed LLP mass (performed with *RooFit* [46]). The background is modeled by events from a sideband selected by a cut on the muon isolation variable. The second method is a two-dimensional sideband technique, the "ABCD" method, used as a cross-check (Section 3.4.2). Both methods are exploiting the low correlation between the LLP mass and the muon isolation, variables which are not included in the neural network active inputs. Furthermore, they have been tested and validated with W and Z decays that share similar properties with signal events (Section 3.4.1.b and 3.4.2.c).

3.4.1 LLP mass fit

The muon isolation distribution for the 2011 data and LV38 signal is displayed in Figure 3.27, after the MLP selection. The region $\text{Isolation} < 1.4$, which contains $(95 \pm 2) \%$ of the signal, is chosen as “signal” region, while the “background” (sideband) region is chosen in the window $1.4 < \text{Isolation} < 1.9$. With this choice, the signal and the background regions have about the same number of events from data. The situation is presented on Figure 3.28 and 3.29 showing the properties of the LLP candidates chosen in the two regions, and, for comparison, the expected signal shape for LV38 10 ps . Figure 3.29 is for the number of tracks, radial distance of the vertex and the vertex errors. The $\chi^2/nDoF$ between the distributions from the sideband and the signal region for each variable are between 0.6 and 1.5 as presented on table 3.22. This indicates that the nature of the candidates in the two regions are similar and that the chosen sideband can be used to model the background in the signal region. Therefore, an extended likelihood simultaneous fit of the the LLP reconstructed mass in the signal and the sideband region is performed for the signal determination.

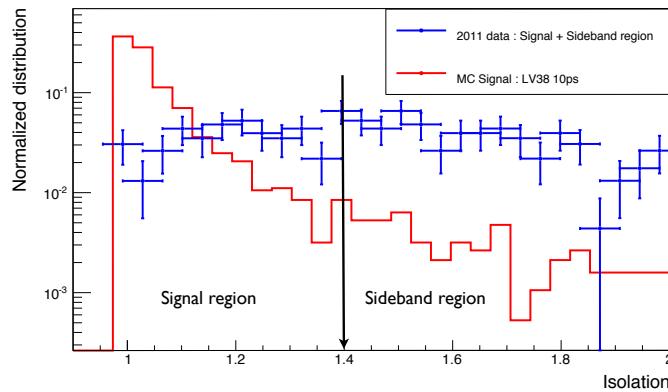


Figure 3.27: Muon isolation for 2011 data compared to LV38 10 ps signal model after the MLP cut with the definition of the signal-free sideband region used to model the background LLP mass shape in the signal region.

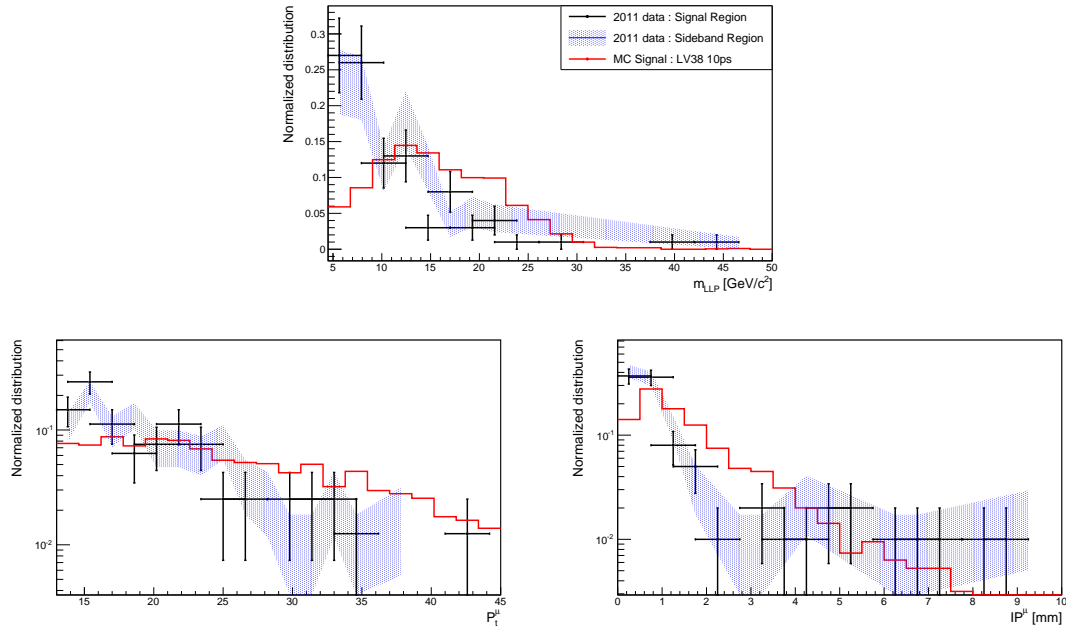


Figure 3.28: Distribution from the 2011 dataset. In black the candidates from the signal region, in dashed blue from the sideband. The predicted LV38 10 ps distribution is in red. Top right: the LLP reconstructed mass. Bottom left: the transverse momentum of the muon. Bottom right: the muon impact parameter with respect to the best primary vertex. The distributions are normalized to unity.

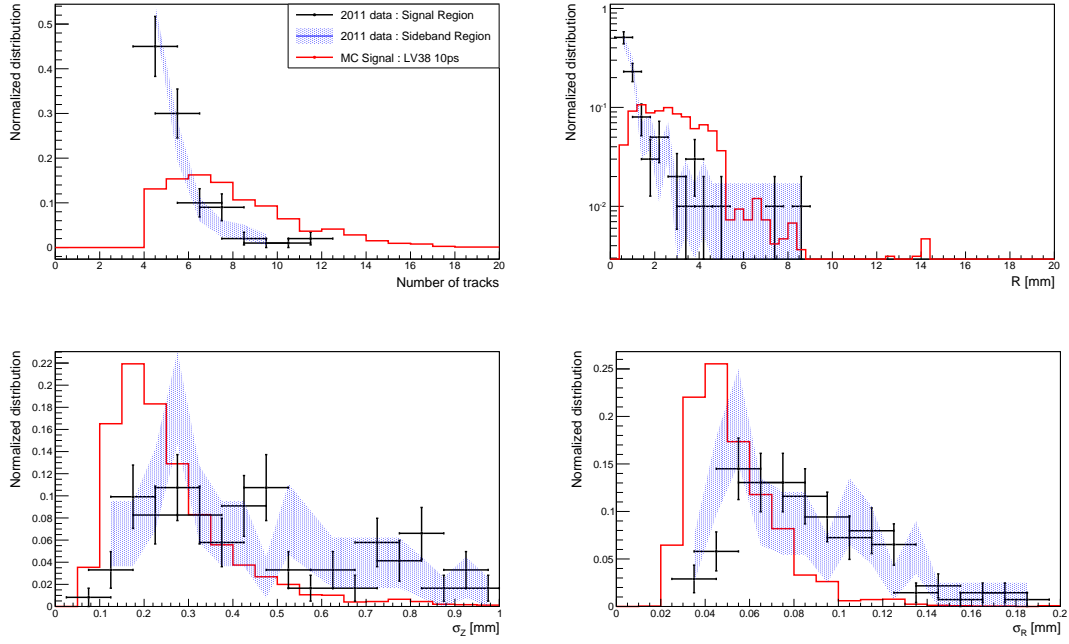


Figure 3.29: Same as figure 3.28 for other variables. Top left: the number of tracks used to reconstruct the LLP. Top right: LLP radial distance R to the beam line. Bottom left and right: the longitudinal and the radial errors on the LLP vertex fit. The distributions are normalized to unity.

Table 3.22: $\chi^2/nDoF$ between the distributions from the sideband and the signal region for each variable.

Variables	m_{LLP}	p_T^μ	IP^μ	N	R	σ_z	σ_R
$\chi^2/nDoF$	1.1	0.6	1.5	1.0	1.0	1.1	0.9

3.4.1.a Fit of LV models to the 2011 and 2012 dataset

An unbinned extended likelihood fit of the LLP mass, m_{LLP} , is applied to determine the presence of signal assuming the different LV models. The background pdf (probability density function) is modeled by the sum of two decreasing exponentials and the signal by an exponential convoluted with a Gaussian (single sided *RooDecay* function). Therefore, the pdfs for the sideband and for the signal region are defined as follow:

- Sideband region:

$$F_{side}(m_{LLP}) = f_{QCD} \cdot e^{-\frac{m_{LLP}}{\tau_{m_{LLP}}}} + (1 - f_{QCD}) \cdot e^{-\frac{m_{LLP}}{r \cdot \tau_{m_{LLP}}}} \quad (3.2)$$

- Signal region:

$$\begin{aligned}
 F_{sig}(m_{LLP}) &= N_{bkg} \cdot F_{side}(m_{LLP}) \\
 &+ N_{sig} \cdot e^{-\frac{m_{LLP}}{\tau_{LV}}} \otimes G(m_{LLP}, \mu_{m_{LLP}, sig}, \sigma_{m_{LLP}, sig})
 \end{aligned} \tag{3.3}$$

The fit is performed simultaneously on the simulated signal events, the background events from the sideband, and the candidates selected in the signal region. The result of the fits of the signal shape for three signal models are presented on Figure 3.30 with the corresponding fit parameters of the *RooDecay* function on Table 3.23. For candidates with a mass larger than $\sim 100 \text{ GeV}/c^2$ a deterioration of the resolution is expected due to particles escaping the geometrical acceptance. This appears in a larger value of the slope of the exponential tail. Typically, the exponential component of the mass shape becomes dominant for LV198.

Table 3.23: Fit parameters of the *RooDecay* function for the different signal model considered ($\tau = 10 \text{ ps}$, $\sqrt{s} = 7 \text{ TeV}$).

Model	τ_{LV}	$\mu_{m_{LLP}, sig}$	$\sigma_{m_{LLP}, sig}$
LV38	3346.8 ± 479.5	15481.4 ± 271.0	7080.3 ± 305.6
LV98	8937.5 ± 2109.0	12016.6 ± 1712.0	24778.9 ± 1646.3
LV198	34790.2 ± 984.2	5401.2 ± 1280.0	9911.4 ± 1850.5

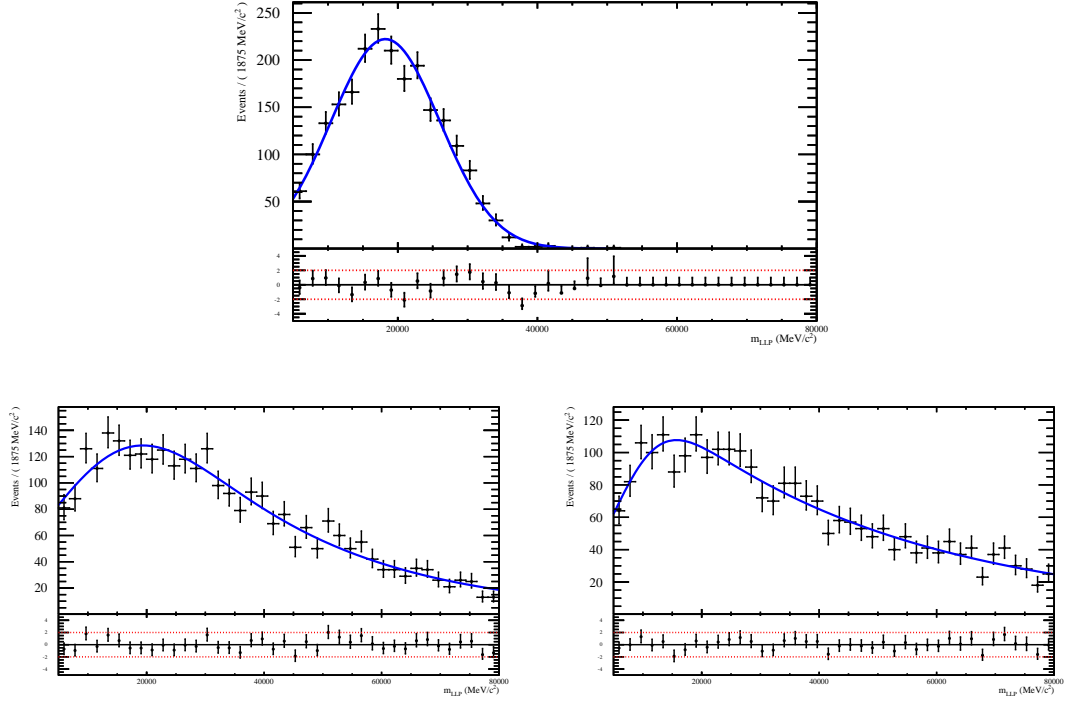


Figure 3.30: Fit results of the different signal model in the signal region with a single side *RooDecay* function ($\tau = 10$ ps) : LV38 (top), LV98 (bottom left) and LV198 (bottom right).

On Figure 3.31 and 3.32 the result of the simultaneous fit in the sideband and in the signal region for 2011 and 2012 data for LV38 ($\tau = 10$ ps) are presented. The fit parameters obtained for the 2011 data are summarized in Table 3.24 for this model. The parameters for the other models, for the 2011 and 2012 datasets are listed in Appendix A.2.

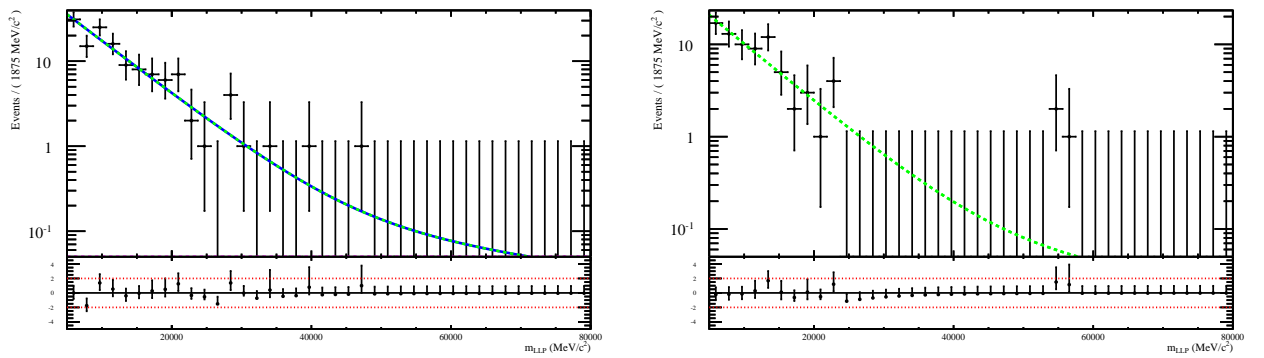


Figure 3.31: Results of the fit performed on 2011 data for LV38 10 ps. The results of the simultaneous fit in the sideband region (right) and in the signal region (left) are shown. The green dashed function is the background component. The blue curve represents the total function (background + signal) in the signal region.

Chapter 3. Search for long-lived particles decaying semileptonically

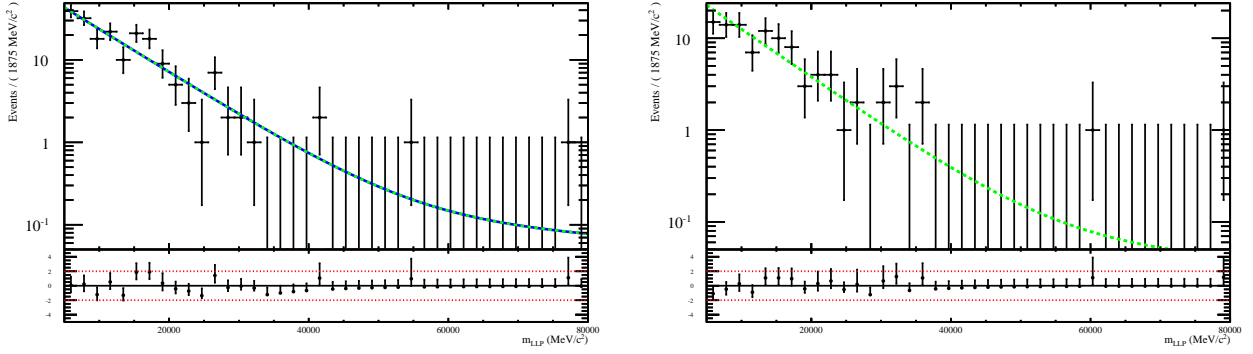


Figure 3.32: Same as Figure 3.31 for the 2012 dataset.

Table 3.24: Parameters from fit performed on the 2011 data sample for LV38 10 ps . See formulas 3.2 and 3.2. N_{sig} and N_{bkg} represent the number of signal events and background events respectively.

$\mu_{m_{LLP},sig}$	$(15481.4 \pm 271.0) \text{ MeV}/c^2$
$\sigma_{m_{LLP},sig}$	$(7080.3 \pm 305.6) \text{ MeV}/c^2$
τ_{LV}	3346.8 ± 479.5
$\tau_{m_{LLP}}$	7771.2 ± 534.2
r	6.32 ± 1.32
f_{QCD}	0.97 ± 0.02
N_{bkg}	126.23 ± 12.25
N_{sig}	-0.31 ± 1.17

On Table 3.25 and 3.26 the results of the fit are summarized for each signal model for the 2011 and 2012 datasets. The results are compatible with zero signal candidates for all the models. The number of background events computed by the fit are in agreement with the number of observed background events. In the table the MLP threshold value is also given.

3.4. Signal determination

Table 3.25: Results of the fitting procedure for each model performed on 2011 data: MLP min is the threshold value on the Neural Network response, N_{sideband} the number of events in the sideband region, N_{signal} the number of events in the signal region. $N_{\text{sig},\text{fit}}$ and $N_{\text{bkg},\text{fit}}$ are the fitted numbers of signal and background events in the signal region.

Model	MLP min	N_{signal}	N_{sideband}	$N_{\text{bkg},\text{fit}}$	$N_{\text{sig},\text{fit}}$
LV38 , $\tau = 5 \text{ ps}$	0.65	102	74	99.01 ± 11.22	2.97 ± 2.52
LV38 , $\tau = 10 \text{ ps}$	0.65	126	76	126.23 ± 12.25	-0.31 ± 1.17
LV38 , $\tau = 50 \text{ ps}$	0.65	83	56	86.89 ± 10.18	-2.01 ± 1.66
LV98 , $\tau = 5 \text{ ps}$	0.6	84	92	86.34 ± 9.90	-2.34 ± 3.01
LV98 , $\tau = 10 \text{ ps}$	0.55	88	59	90.75 ± 10.44	-2.78 ± 3.90
LV98 , $\tau = 50 \text{ ps}$	0.55	87	63	89.86 ± 10.37	-2.82 ± 3.83
LV198 , $\tau = 5 \text{ ps}$	0.55	97	77	99.87 ± 10.58	-2.87 ± 3.04
LV198 , $\tau = 10 \text{ ps}$	0.48	114	115	118.98 ± 11.60	-3.04 ± 3.42
LV198 , $\tau = 50 \text{ ps}$	0.48	83	60	85.22 ± 10.10	-2.16 ± 3.82

Table 3.26: Like Table 3.25 for 2012 data ($\sqrt{s} = 8 \text{ TeV}$).

Model	MLP	N_{signal}	N_{sideband}	$N_{\text{bkg},\text{fit}}$	$N_{\text{sig},\text{fit}}$
LV38 , $\tau = 5 \text{ ps}$	0.7	168	92	169.69 ± 14.03	-1.68 ± 4.57
LV38 , $\tau = 10 \text{ ps}$	0.85	174	94	177.30 ± 20.72	-3.21 ± 4.93
LV38 , $\tau = 50 \text{ ps}$	0.8	167	98	164.72 ± 12.85	2.07 ± 5.04
LV98 , $\tau = 5 \text{ ps}$	0.65	153	89	150.85 ± 12.58	2.28 ± 3.08
LV98 , $\tau = 10 \text{ ps}$	0.7	146	78	143.23 ± 12.18	2.78 ± 2.80
LV98 , $\tau = 50 \text{ ps}$	0.65	128	71	125.81 ± 11.45	2.20 ± 2.72
LV198 , $\tau = 5 \text{ ps}$	0.6	178	89	176.17 ± 13.29	1.84 ± 2.09
LV198 , $\tau = 10 \text{ ps}$	0.7	183	85	180.50 ± 13.46	2.51 ± 2.40
LV198 , $\tau = 50 \text{ ps}$	0.55	138	84	135.65 ± 11.84	2.35 ± 2.66

The sensitivity of the method has been tested with toy Monte Carlo experiments. A fixed amount of signal events, N_s , is randomly extracted from the signal Monte Carlo sample and added to the dataset for each toy experiment. The fit procedure is applied and the number of signal events found is compared to the true value N_s . 5000 toy experiments are generated and analyzed. On Table 3.27, the number of signal events determined by the fit are given for each N_s values. The method has a 4σ sensitivity for ~ 5 LLPs. The pull distributions are given on Figure 3.33.

Table 3.27: Number of signal events extracted from the fit of the Monte Carlo toy experiments for different models with a fixed lifetime of $\tau = 10$ ps and a number N_s of signal events. The number of background has been fixed to respectively 126, 88 and 114 for LV38, LV98 and LV198, as it is the case in the 2011 data analysis.

Model	$N_s = 1$	$N_s = 2$	$N_s = 3$	$N_s = 4$	$N_s = 5$	$N_s = 10$
LV38	0.84 ± 1.17	1.61 ± 1.24	2.73 ± 1.37	3.90 ± 1.54	4.89 ± 1.21	9.64 ± 1.40
LV98	0.21 ± 3.93	1.43 ± 4.04	2.57 ± 3.41	3.61 ± 3.94	4.74 ± 3.62	9.70 ± 3.80
LV198	0.35 ± 3.57	1.32 ± 3.79	2.84 ± 3.69	3.51 ± 3.61	4.73 ± 3.54	9.88 ± 3.77

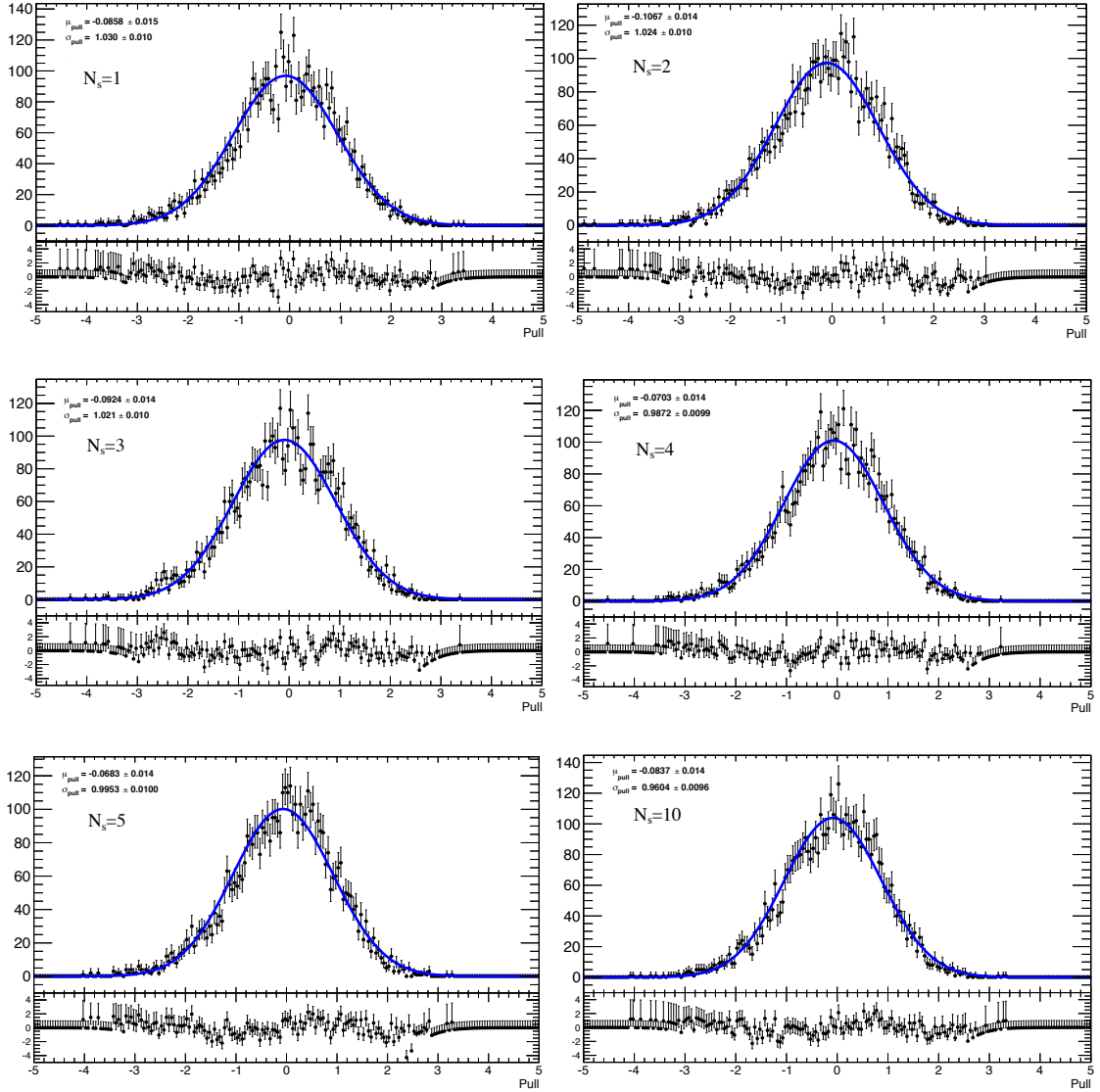


Figure 3.33: Pull distribution of the number of extracted signal events for different number of injected signal events for LV38 ($\tau = 10$ ps). μ_{pull} and σ_{pull} are the mean and the standard deviation of the gaussian fit. The pull distribution is defined as: $Pull = \frac{N_s^{fit} - N_s}{\sigma_{N_s^{fit}}}$.

3.4.1.b Fit method applied to W and Z decays

The aim of this study is to test and validate the fitting method on $W \rightarrow \mu\nu$ and $Z \rightarrow \mu\mu$ decays. The displaced vertex reconstructed from W and Z events are preselected probably by missing the primary vertex in the displaced vertex algorithm. Besides the position of the vertex, the LV signals and these two channels share quite similar properties. In particular the muon is isolated and has a large p_T . The LLP candidate is formed by collecting tracks from the primary vertex. In the case of $Z \rightarrow \mu\mu$, when the two muons are collected accompanied by soft tracks,

Chapter 3. Search for long-lived particles decaying semileptonically

the Z mass peak is visible in the distribution. The fit method has been applied to events after preselection, before the radial cut in such a way to preserve the W and Z (prompt) decays.

As it has been the case for the LV analysis, the sideband is defined to be a region of the muon isolation where the presence of W and the Z events is negligible in comparison to the amount of $b\bar{b}$ events. The chosen signal and sideband regions are the same for W and Z event:

- Signal region $1 \leq E/E(\mu) < 1.4$: W and Z events + QCD background
- Sideband region $1.9 > E/E(\mu) > 1.4$: containing mainly QCD background

On Figure 3.34 the bi-parametric distribution of the muon isolation versus the reconstructed mass of the LLP are presented for the data, W and Z events. For comparison, the prediction for the signal $LV38$ $10ps$ is also shown.

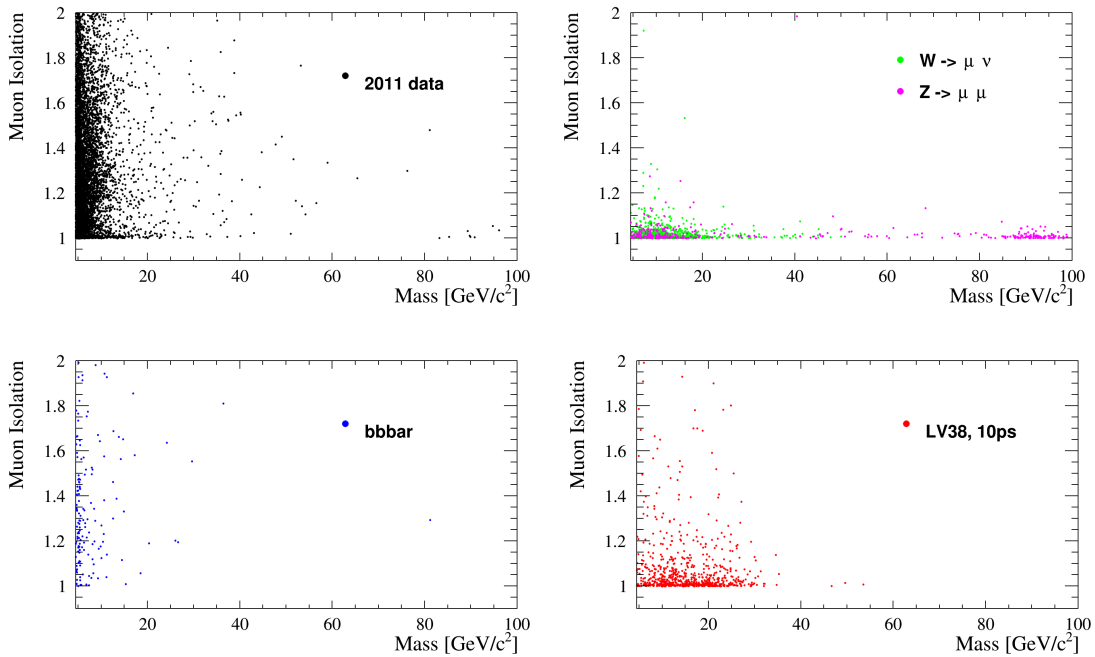


Figure 3.34: LLP reconstructed mass versus the muon isolation. Top Left: 2011 data. Bottom left: $b\bar{b}$ simulated events. Top Right: W and Z MC events. Bottom Right: $LV38$ $10ps$ signal events for comparison.

A simultaneous fit of the mass of the LLP candidates in the signal and background regions is made in the range $m_{LLP} \in (5, 150)$ GeV/c^2 , $p_T^\mu \in (16, 70)$ GeV/c . This corresponds to the range where the probability to observe W and Z is greater than QCD background and the contribution of $W \rightarrow \tau \nu$ and $Z \rightarrow \tau \tau$ negligible.

The $W \rightarrow \mu\nu$ signal distribution has been modeled with two exponentials convoluted by a Gaussian resolution function:

$$F_W(m) = (f_W \exp(-\frac{m}{\tau_{W,1}}) + (1 - f_W) \exp(-\frac{m}{\tau_{W,2}})) \otimes G(m, \mu_W, \sigma_W) \quad (3.4)$$

For the Z , a similar function is used plus a Breit-Wigner for the Z peak:

$$F_Z(m) = f_{Z,1} BW(m, \mu_{Z,BW}, g_Z) + (1 - f_{Z,1}) (f_{Z,2} \exp(-\frac{m}{\tau_Z}) + (1 - f_{Z,2}) G(m, \mu_{Z,2}, \sigma_Z)) \quad (3.5)$$

Figure 3.35 shows the fit results of the $W \rightarrow \mu\nu$ and $Z \rightarrow \mu\mu$ Monte Carlo sample for $\sqrt{s} = 7$ TeV.

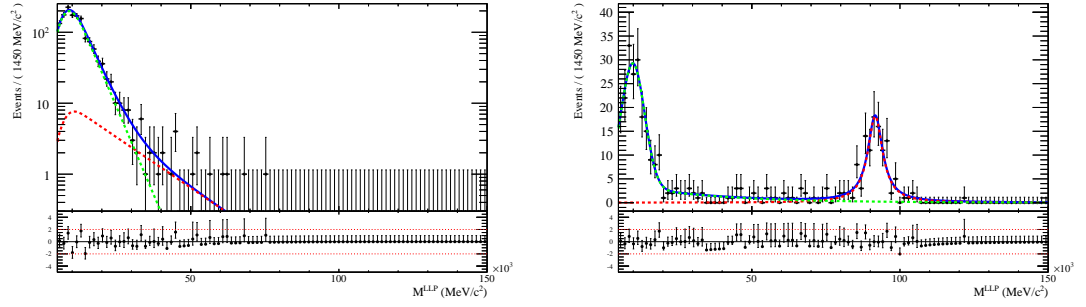


Figure 3.35: $W \rightarrow \mu\nu$ and $Z \rightarrow \mu\mu$ Monte Carlo sample mass fit for 2011 conditions. Left: $W \rightarrow \mu\nu$ mass fit with $F_W(m)$, in red and green the two exponentials convoluted with the same gaussian resolution function. $\chi^2/nDoF = 1.6$. Right: $Z \rightarrow \mu\mu$ mass fit $F_Z(m)$, in red the Breit-Wigner function and in green the sum of the exponential and the Gaussian function. $\chi^2/nDoF = 2.2$.

The QCD background has been modeled by two negative slope exponentials:

$$F_{QCD}(m) = f_{QCD} \cdot e^{-\frac{m}{\tau_{QCD}}} + (1 - f_{QCD}) \cdot e^{-\frac{m}{r \cdot \tau_{QCD}}} \quad (3.6)$$

Therefore, the functions to be fitted are the following:

- sideband region:

$$F_{side}(m) = N_{side}F_{QCD}(m) \quad (3.7)$$

- Signal region:

$$F_{sig}(m) = N_{QCD}F_{QCD}(m) \quad (3.8)$$

$$+ N_{EW}(f_{EW} \cdot F_W(m) + (1 - f_{EW}) \cdot F_Z(m)) \quad (3.9)$$

N_{side} , N_{QCD} and N_{EW} are the number of events in the sideband region, the number of QCD background events in the signal region and the number of W plus Z events in the signal region. Figure 3.36 shows the result of the simultaneous fit of the candidate mass distribution in the signal region and in the sideband region for the 2011 data. The fitted parameters are given in Table 3.28.

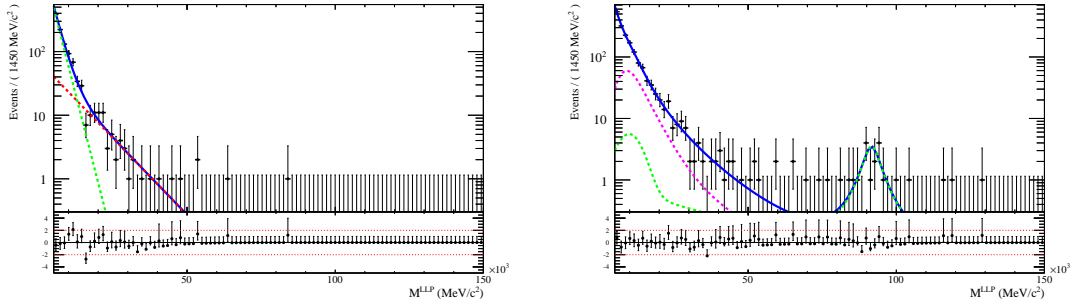


Figure 3.36: Mass fit for the determination of the W and Z signal in the 2011 dataset. Left: the fit for candidates from the sideband region; in green and red the two exponential, in blue the total fitted function. Right: the fit for candidates from the signal region; in blue the total fitted function, in magenta, the W component modeled with $F_W(m)$, and, in green, the Z component modeled with $F_Z(m)$. The fit gives $\chi^2/nDoF = 1.8$.

The same procedure has been reproduced by considering separately the positive and the negative charge of the preselected muons to extract the observed cross-section $W^+ \rightarrow \mu^+ \nu$ and $W^- \rightarrow \mu^- \nu$ for 2011. The results are given in Figure 3.37 and Table 3.28.

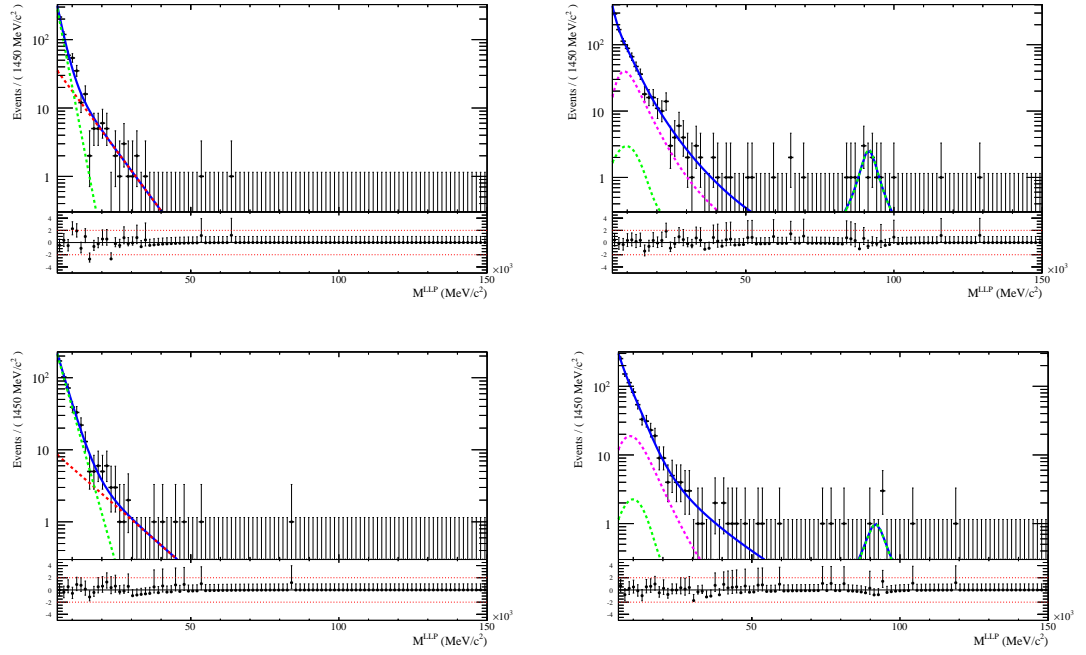


Figure 3.37: Same as Figure 3.36. Top: fit of events with a positive charged preselected muon. $\chi^2/nDoF = 1.4$. Bottom: fit of events with a negative charged preselected muon. $\chi^2/nDoF = 2.3$.

Chapter 3. Search for long-lived particles decaying semileptonically

Table 3.28: Parameters of the simultaneous fit procedure of 2011 data with W and Z decay channel playing the role of signal. Total denotes no distinction in the muons charge.

	Total	Positive charged muon	Negative charged muon
$F_{sig}(m)$			
N_{QCD}	1284.7 ± 71.2	641.3 ± 48.5	657.9 ± 54.5
N_{EW}	482.3 ± 65.3	303.7 ± 44.8	164.2 ± 49.7
f_{EW}	0.859 ± 0.036	0.870 ± 0.040	0.846 ± 0.074
$F_{side}(m)$			
N_{side}	1041.0 ± 32.3	545.0 ± 23.3	496.0 ± 22.3
$F_{QCD}(m)$			
τ_{QCD}	$(-1.1 \pm 0.1) \times 10^{-4}$	$(-1.3 \pm 0.2) \times 10^{-4}$	$(-0.8 \pm 0.2) \times 10^{-4}$
r	3.792 ± 0.349	3.857 ± 0.388	4.098 ± 0.786
f_{QCD}	0.2407 ± 0.056	0.328 ± 0.098	0.143 ± 0.057
$F_Z(m)$			
$\mu_{Z,BW}$	91655.7 ± 382.6	91521.1 ± 457.1	91779.4 ± 692.4
g_Z	6105.5 ± 841.4	5506.4 ± 927.5	7038.5 ± 1733.8
$\mu_{Z,2}$	9921.3 ± 517.9	9833.2 ± 824.9	9981.3 ± 664.4
$\sigma_{Z,2}$	3928.0 ± 517.8	3994.8 ± 859.2	3865.1 ± 644.8
τ_Z	$(-3.3 \pm 0.8) \times 10^{-5}$	$(-3.4 \pm 1.2) \times 10^{-5}$	$(-3.2 \pm 1.0) \times 10^{-5}$
$f_{Z,1}$	0.674 ± 0.029	0.625 ± 0.041	0.072 ± 0.042
$f_{Z,2}$	0.653 ± 0.056	0.637 ± 0.090	0.663 ± 0.073
$F_W(m)$			
μ_W	6461.7 ± 243.9	6620.7 ± 277.2	6114.8 ± 522.8
σ_W	2829.1 ± 355.9	2476.1 ± 407.1	3522.1 ± 782.6
f_W	0.077 ± 0.044	0.109 ± 0.075	0.049 ± 0.047
$\tau_{W,1}$	15276.4 ± 4049.0	13924.0 ± 4304.3	17477.5 ± 8497.6
$\tau_{W,2}$	4406.7 ± 424.2	4334.9 ± 609.4	4382.3 ± 695.3

68 ± 20 $Z \rightarrow \mu^+ \mu^-$ events have been computed from the fit which is compatible with 48 ± 6 events predicted by the MC simulation for 2011, in the signal region for $m_{LLP} \in [5, 150]$ GeV/ c^2 and $p_T^\mu \in [16, 70]$ GeV/ c .

From simulation, the preselection efficiencies for W^+ and W^- events are respectively $\epsilon_{W^+} = (3.00 \pm 0.10) \cdot 10^{-4}$ and $\epsilon_{W^-} = (2.64 \pm 0.13) \cdot 10^{-4}$ (uncertainties are statistical). The production cross-section of $W^{+/-} \rightarrow \mu^{+/-} \nu(\bar{\nu})$ and the ratio R_W are then:

$$\sigma_{W^+ \rightarrow \mu^+ \nu} = 878 \pm 144 \text{ pb} \quad (3.10)$$

$$\sigma_{W^- \rightarrow \mu^- \bar{\nu}} = 526 \pm 169 \text{ pb} \quad (3.11)$$

$$R_W = \frac{\sigma_{W^+ \rightarrow \mu^+ \nu}}{\sigma_{W^- \rightarrow \mu^- \bar{\nu}}} = 1.7 \pm 0.6 \quad (3.12)$$

The uncertainties are statistical only. These values are compatible with the measured cross-sections made by LHCb for 2011 data with an integrated luminosity of 1 fb^{-1} at LHCb [41]:

$$\sigma_{W^+ \rightarrow \mu^+ \nu} = 846.9 \pm 2.0 \pm 10.9 \pm 29.9 \text{ pb} \quad (3.13)$$

$$\sigma_{W^- \rightarrow \mu^- \bar{\nu}} = 664.6 \pm 1.8 \pm 8.7 \pm 23.5 \text{ pb} \quad (3.14)$$

$$R_W = \frac{\sigma_{W^+ \rightarrow \mu^+ \nu}}{\sigma_{W^- \rightarrow \mu^- \bar{\nu}}} = 1.274 \pm 0.005 \pm 0.009 \quad (3.15)$$

where the first uncertainty is statistical, the second is systematical and the third is due to the luminosity determination. The production cross-sections at $\sqrt{s} = 8 \text{ TeV}$ have been estimated from this results by comparing the production cross-section given by MadGraph 5 [47] at the Next-to-leading Order (NLO) at $\sqrt{s} = 7$ and 8 TeV .

The proportionality factors are:

$$k_{W^+} = \frac{\sigma_{W^+}(8 \text{ TeV})}{\sigma_{W^+}(7 \text{ TeV})} = 1.14 \quad (3.16)$$

$$k_{W^-} = \frac{\sigma_{W^-}(8 \text{ TeV})}{\sigma_{W^-}(7 \text{ TeV})} = 1.16 \quad (3.17)$$

$$(3.18)$$

Thus, this fitting procedure, presented in Appendix A.6, have been reproduced for 2012 dataset with an integrated luminosity of 1.98 fb^{-1} and leads to the following production cross-section and ratio at $\sqrt{s} = 8 \text{ TeV}$:

$$\sigma_{W^+ \rightarrow \mu^+ \nu} = 1025 \pm 113 \text{ pb} \quad (3.19)$$

$$\sigma_{W^- \rightarrow \mu^- \bar{\nu}} = 740 \pm 84 \text{ pb} \quad (3.20)$$

$$R_W = \frac{\sigma_{W^+ \rightarrow \mu^+ \nu}}{\sigma_{W^- \rightarrow \mu^- \bar{\nu}}} = 1.4 \pm 0.2 \quad (3.21)$$

These values are compatible with the production cross-sections made for 2011 data multiplied by the proportionality factors k_{W^+} and k_{W^-} .

It has been possible to extract a correct Z and W signal yield from the simultaneous fit procedure. This study is a good indication that the events collected in the sideband defined by a cut on the muon isolation variable, allow to model the background in the signal region.

3.4.2 The ABCD method

This method exploits the low correlation between the LLP reconstructed mass, m_{LLP} , and the isolation variable for the muon, together with the relatively good separation of the signal and the background in a bi-parametric distribution (m_{LLP} , $1/\text{Isolation}$).

Choosing two boundary values in the (m_{LLP} , $1/\text{Isolation}$) plane four regions A,B,C, and D are defined, with their respective observed number of events N_A, N_B, N_C , and N_D . The region D contains the largest fraction of signal. If a negligible amount of signal is present in A, B, C, and if the background does not show a correlation in the two variables the estimates for the number of background events in D, \bar{B}_D , and for the signal, \bar{S}_D , are:

$$\bar{B}_D = \frac{N_B N_C}{N_A} \quad (3.22)$$

$$\bar{S}_D = N_D - \bar{B}_D \quad (3.23)$$

When a too large amount of signal is present in the “sideband” regions A, B and C, if known, the signal “contamination” can be subtracted to improve the estimate. The optimization of the boundaries defining the four regions in the plane (m_{LLP} , $1/\text{Isolation}$) is done by maximizing the significance of the signal ($S_D / \sqrt{S_D + \bar{B}_D}$) with a set of 1000 toy Monte Carlo experiments. The significance can be approximated by:

$$\hat{S} = \frac{S_D}{\sqrt{S_D + \bar{B}_D^2 \left(\frac{1}{N_A} + \frac{1}{N_B} + \frac{1}{N_C} \right)}} \quad (3.24)$$

This quantity depends on the number of signal events hypothesis. For illustration, Figure 3.38 shows the computed significance values for different set of cuts in the plane (m_{LLP} , $1/\text{Isolation}$). For this example, 200 background events and 5 LV38 signal events have been considered. The background is obtained from the data bi-parametric distribution after the MLP selection. The four regions with the optimal boundaries (16 GeV/c², 0.9) are presented on Figure 3.39 for a toy experiment. The larger portion of the signal is in the D region, but a quite large fraction is also present in the sidebands.

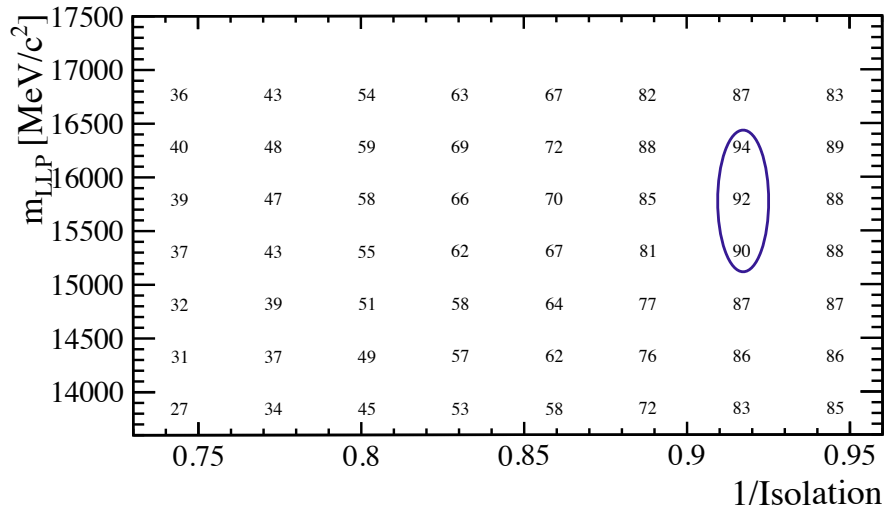


Figure 3.38: Example of the significance values for 200 background events and 5 signal events as a function of the cuts on the LLP mass and the muon isolation. The significance is multiplied by a factor 100. The blue circle denotes the boundaries with the best significance.

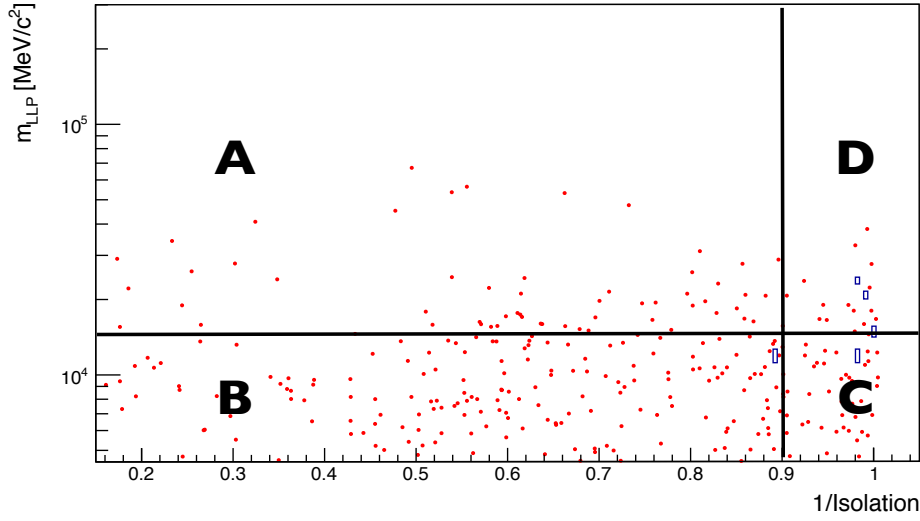


Figure 3.39: Example of toy experiment with 200 background events (red) and 5 signal events based on LV38 ($\tau = 10$ ps) (blue boxes). A, B, and C are the sidebands used to estimate the background in D.

The implementation and test of the ABCD method consist of the following steps. The region boundaries are chosen for each model, based on the best significance. Some level of correlation between m_{LLP} and $1/isolation$ can affect the ABCD procedure: the second step is to estimate the effects of such correlation, Section 3.4.2.a. Then the ABCD is applied for each model to the events of the two datasets, Section 3.4.2.a. Finally the method is tested on $Z \rightarrow \mu\mu$ decays for the 2011 dataset, Section 3.4.2.c.

3.4.2.a Definition of boundaries and estimate of the correlation bias

For the setup of the ABCD method toy MC experiments are used. For this, the number of data events available to model the background for the generation of the experiments is increased up to about 2000 by relaxing the MLP selection by a factor 0.8 (see Appendix A.5).

Based on equation 3.24, the boundaries that give the best signal significance assuming 5 signal events and 200 background events are calculated for each signal model and datasets. The values are given in Table 3.29.

To quantify the effect of a potential correlation between the m_{LLP} and the $1/Isolation$ variables, the results from the toy experiments generated from the bi-parametric distribution $PDF(m_{LLP}, 1/Isolation)$ are compared to the results obtained by a generation from the two projections, i. e. from $PDF(m_{LLP}) \times PDF(1/Isolation)$. On Table 3.30 the results of the MC toy study are presented for the 2011 dataset and LV38 10 ps. The average number of signal events in the region A, B and C have been subtracted to determine the signal and background yields. From the generation based on the bi-parametric distribution, $\bar{S}_D = 2.64 \pm 2.92$ signal events ($\bar{B}_D = 4.58 \pm 1.48$ background events) are predicted. In comparison, 1.96 ± 2.97 signal

3.4. Signal determination

events (4.99 ± 1.58 background events) are obtained with toys based on the projections. Both tests are compatible with the average number of signal events in the region D, 2 ± 1 , which indicates a low level of correlation. A correction on the number of events given by the difference $1.96 - 2.64 = -0.68$ is used to account for the correlation.

The results of this procedure applied to the 2011 and 2012 data, and for each signal modes, are presented on Appendix A.6). The level of bias is about 0.7 signal events, on the average.

As a cross-check, the determination of the bias from correlation has been performed on MC $b\bar{b}$ background events and 2011 data, after totally removing the MLP selection, see Appendix A.7). These tests indicate that the method is reliable.

Table 3.29: Optimized boundaries for the ABCD analysis of the 2011 (left table) and 2012 (right table) dataset. The MLP cut used is also indicated.

Model	2011			2012		
	MLP min	m_{LLP} (GeV/c^2)	Iso^{-1}	MLP min	m_{LLP} (GeV/c^2)	Iso^{-1}
LV38, ($\tau = 5$ ps)	0.52	16	0.9	0.63	16	0.9
LV38, ($\tau = 10$ ps)	0.52	16	0.9	0.76	16	0.9
LV38, ($\tau = 50$ ps)	0.52	16	0.9	0.72	16	0.9
LV98, ($\tau = 5$ ps)	0.48	16.5	0.93	0.58	16.5	0.93
LV98, ($\tau = 10$ ps)	0.44	16.5	0.93	0.63	16.5	0.93
LV98, ($\tau = 50$ ps)	0.44	16.5	0.93	0.58	16.5	0.93
LV198, ($\tau = 5$ ps)	0.44	21.5	0.93	0.54	21.5	0.93
LV198, ($\tau = 10$ ps)	0.38	21.5	0.93	0.63	21.5	0.93
LV198, ($\tau = 50$ ps)	0.38	21.5	0.93	0.49	21.5	0.93

Table 3.30: Results of 1000 toy experiments for LV38 10 ps signal events and 2011 data with the boundaries placed at $m_{LLP} = 16$ GeV/c^2 and $Iso^{-1} = 0.9$, for 200 background and 5 signal events. "Total" defines the average of the sum of background and signal events in each region and "signal" correspond to the number of signal events. "2D" and "Proj" are referring to the toys based on the bi-parametric $PDF(m_{LLP}, 1/Isolation)$ and on the projections $PDF(m_{LLP}) \times PDF(1/Isolation)$, respectively. The uncertainties are the RMS.

Model	\bar{S}_D	\bar{B}_D	N_A	N_B	N_C	N_D
LV38 ($\tau = 10$ ps) (2D,total)	2.64 ± 2.92	4.58 ± 1.48	29.00 ± 4.92	144.16 ± 6.48	24.62 ± 4.76	7.22 ± 2.52
LV38 ($\tau = 10$ ps) (2D,signal)			0.94 ± 0.88	0.83 ± 0.84	1.25 ± 0.95	1.98 ± 1.09
LV38 ($\tau = 10$ ps) (Proj,total)	1.96 ± 2.97	4.99 ± 1.58	30.59 ± 5.12	142.25 ± 6.22	25.21 ± 4.69	6.95 ± 2.52
LV38 ($\tau = 10$ ps) (Proj,signal)			1.04 ± 0.91	0.70 ± 0.75	1.32 ± 0.97	1.94 ± 1.10

3.4.2.b Determination of the signal for the 2011 and 2012 datasets

The ABCD method is applied to the data for each signal model after the selection on the MLP. On Table 3.31 and 3.32, the results of the procedure are presented for the 2011 and 2012 datasets. The statistical uncertainties are obtained from the toy Monte Carlo. The estimated number of signal events has been corrected for correlation effects and is compatible with zero for all LV models.

Table 3.31: Results of the ABCD method applied to the 2011 dataset, for each signal model. The number of estimated signal events \hat{S}_D is corrected for the correlation effects.

Model (N_{rem} event)	MLP	\hat{S}_D	\hat{B}_D	N_A	N_B	N_C	N_D
LV38 ($\tau = 5$ ps) (1069)	0.65	-1.8 ± 3.9	11.1 ± 2.1	52	140	30	10
LV38 ($\tau = 10$ ps) (1222)	0.65	-0.7 ± 4.2	12.1 ± 2.4	50	170	41	12
LV38 ($\tau = 50$ ps) (801)	0.65	-1.8 ± 3.7	9.7 ± 2.3	36	115	31	9
LV98 ($\tau = 5$ ps) (1296)	0.60	0.1 ± 2.8	5.5 ± 1.4	45	165	20	6
LV98 ($\tau = 10$ ps) (2111)	0.55	-0.7 ± 3.6	9.5 ± 2.0	54	177	31	9
LV98 ($\tau = 50$ ps) (1509)	0.55	3.0 ± 3.1	5.0 ± 1.4	34	136	20	8
LV198 ($\tau = 5$ ps) (1589)	0.55	-0.1 ± 1.9	3.1 ± 0.8	27	256	29	3
LV198 ($\tau = 10$ ps) (1974)	0.48	-2.3 ± 1.8	4.7 ± 1.1	32	237	35	2
LV198 ($\tau = 50$ ps) (1383)	0.48	1.2 ± 2.2	3.0 ± 0.9	18	158	26	4

Table 3.32: Same as Table 3.31 for the 2012 dataset.

Model (N_{rem} event)	MLP	\hat{S}_D	\hat{B}_D	N_A	N_B	N_C	N_D
LV38 ($\tau = 5$ ps) (1034)	0.7	3.6 ± 5.0	19.0 ± 3.0	114	246	41	25
LV38 ($\tau = 10$ ps) (1152)	0.85	1.7 ± 6.4	22.7 ± 4.3	112	257	52	27
LV38 ($\tau = 50$ ps) (745)	0.8	2.5 ± 6.1	16.4 ± 3.6	94	252	44	21
LV98 ($\tau = 5$ ps) (1795)	0.65	0.6 ± 4.4	13.5 ± 2.5	98	246	34	15
LV98 ($\tau = 10$ ps) (2310)	0.7	0.0 ± 3.8	10.9 ± 1.9	79	261	36	11
LV98 ($\tau = 50$ ps) (1553)	0.65	-2.0 ± 4.1	13.8 ± 2.4	83	204	34	12
LV198 ($\tau = 5$ ps) (1800)	0.6	-0.5 ± 2.7	8.4 ± 1.2	49	328	56	8
LV198 ($\tau = 10$ ps) (2263)	0.7	0.4 ± 2.5	7.1 ± 1.1	43	335	55	7
LV198 ($\tau = 50$ ps) (1570)	0.55	-2.2 ± 2.3	7.3 ± 1.2	45	273	44	6

3.4.2.c Validation with $Z \rightarrow \mu\mu$ as a control channel

The ABCD method is applied to the preselected 2011 dataset, considering $Z \rightarrow \mu\mu$ events as the target signal. On Figure 3.40, the region A,B,C and D are highlighted for 2011 data, with simulated Z events superposed. The best significance has been obtained with boundaries placed at $m_{LLP} = 70$ GeV/c² and $1/Isolation = 0.93$, assuming 20 signal events. The MC prediction is 17 ± 4 $Z \rightarrow \mu\mu$ events in the D region.

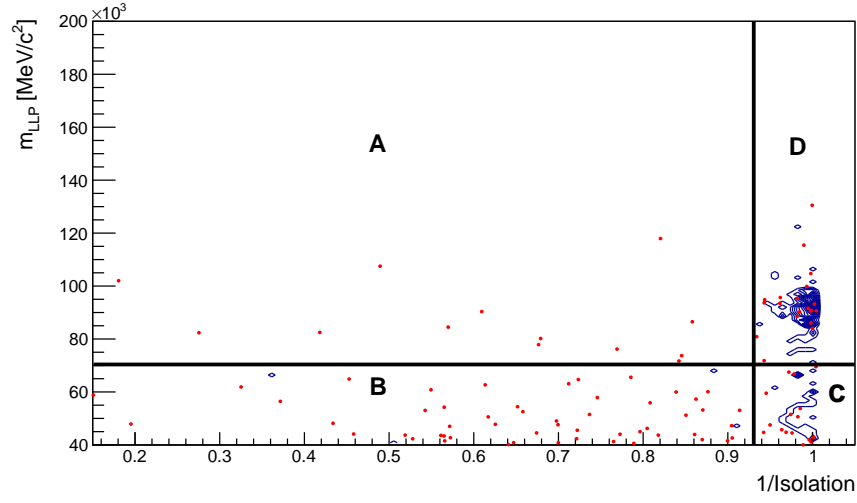


Figure 3.40: The A,B,C and D regions defined in the plane $(m_{LLP}, 1/Isolation)$. The 2011 data preselected events are plotted in red for masses of the LLP greater than $40 \text{ GeV}/c^2$. The contours are obtained from $Z \rightarrow \mu\mu$ simulated decays.

The number of events in the region A,B, C and D in the 2011 dataset are respectively 15, 121, 35 and 20. The events in the region A and B are pure QCD background, while the C region contains 17.6 ± 5.1 $W \rightarrow \mu\nu$ decays on average, and 2.6 ± 1.5 $Z \rightarrow \mu\mu$.

The number of events in each region after the subtraction of the Z and W predicted number of events in the region C are summarized on Table 3.33. 18.2 ± 4.3 signal events (\bar{S}_D) and 1.8 ± 0.7 background events (\bar{B}_D) are obtained.

For 18 Z events and 150 background events, an average $\bar{S}_D = 20.1 \pm 3.4$ ($\bar{B}_D = 1.6 \pm 0.9$) is obtained when the PDF is the bi-parametric distribution, while $\bar{S}_D = 15.9 \pm 3.3$ ($\bar{B}_D = 3.6 \pm 1.7$) is obtained from the projections. Thus, 4.2 events are subtracted from the 17.6, to correct for correlation effects. Therefore, the number of $Z \rightarrow \mu\mu$ events in the region D from the ABCD method is 14.1 ± 4.3 comparing well with the 17 ± 4 $Z \rightarrow \mu\mu$ events predicted.

Table 3.33: From the ABCD method applied to the measurement of the number of Z events in the 2011 dataset. number of events in the four regions and estimates for the signal and background in D. The average number of W and Z decays predicted from the simulation have been subtracted from N_C .

	N_A	N_B	N_C	N_D	\bar{S}_D	\bar{B}_D
2011 data	15	121	14.8	20	18.2 ± 4.3	1.8 ± 0.7

3.5 Detection efficiency and systematic effects

On Table 3.34 and 3.35, the contributions to the efficiency at different stages of the event selection obtained from the analysis of simulated events are presented for $\sqrt{s} = 7$ and 8 TeV. The range indicated covers the LLP lifetimes of 5, 10 and 50 ps .

Table 3.34: Contributions to the efficiency in percent at the different stages of the event selection at $\sqrt{s} = 7$ TeV. The range is for the LV models with lifetime of $\tau = 5, 10$ and 50 ps .

Selection stage	LV38	LV98	LV198
Trigger and Stripping selection	16.7 – 22.0	23.0 – 27.7	26.8 – 34.0
Displaced Vertex Reconstruction	48.1 – 51.1	34.8 – 37.5	25.6 – 29.0
MV	65.4 – 86.9	91.5 – 96.2	78.8 – 99.0
Muon quality cuts	79.8 – 81.0	85.5 – 86.2	87.5 – 87.9
$R > 0.55$ mm	93.8 – 97.1	85.4 – 90.0	83.8 – 95.0
MLP and Isolation	78.0 – 90.2	92.2 – 94.3	95.5 – 98.4
Total	3.6 – 5.3	5.0 – 6.8	4.9 – 6.8

Table 3.35: Same as table 3.34 for $\sqrt{s} = 8$ TeV

Selection stage	LV38	LV98	LV198
Trigger and Stripping selection	17.5 – 23.7	24.3 – 29.4	28.5 – 35.6
Displaced Vertex Reconstruction	51.9 – 56.3	40.6 – 43.8	31.9 – 34.7
MV	64.1 – 85.0	76.0 – 97.3	78.4 – 98.8
Muon quality cuts	78.2 – 79.9	84.7 – 85.8	87.5 – 88.1
$R > 0.55$ mm	95.2 – 97.4	86.0 – 95.1	83.3 – 95.6
MLP and Isolation	82.2 – 98.5	89.1 – 91.0	90.6 – 93.4
Total	3.6 – 5.4	5.8 – 8.1	5.8 – 8.4

The discussion of the sources of systematic uncertainties follows the analysis flow:

- We first consider the detection of the muon, in Section 3.5.1,
- Section 3.5.2 treats the vertex reconstruction
- Section 3.5.3 the MLP filter
- Section 3.5.4 the mass and muon isolation calibration
- Section 3.5.5 the beam line position
- Section 3.5.6 the integrated luminosity

3.5. Detection efficiency and systematic effects

The different contributions for the analysis of the 2011 and 2012 datasets are summarized on table 3.36 and 3.37 .

Table 3.36: Summary of the systematic uncertainties, in %, on the selection efficiency for the 2011 dataset analysis.

Contribution / Model	LV38 5ps	LV38 10ps	LV38 50ps	LV98 5ps	LV98 10ps	LV98 50ps	LV198 5ps	LV198 10ps	LV198 50ps
Muon reconstruction	4.5	4.5	4.5	3.9	3.9	3.9	3.9	3.9	3.9
IP cut (Stripping)	1.6	0.9	0.5	1.1	0.5	0.4	0.7	0.6	0.4
Vertex reconstruction	8	8	8	8	8	8	8	8	8
Neural network	1.4	1.4	1.4	1.6	1.8	1.6	2.1	1.3	1.6
Number of tracks cut	5	5	5	5	5	5	5	5	5
Isolation cut	3.5	3	3.1	1.1	1.0	1.2	0.8	1.0	1.1
Mass cut	1.4	2.0	2.5	1.2	1.4	1.3	1.3	1.3	1.2
Beam line position	0.2	0.2	0.1	0.6	0.5	0.3	0.8	0.7	0.5
Luminosity	1.7	1.7	1.7	1.7	1.7	1.7	1.7	1.7	1.7
Total	11.4	11.3	11.4	10.7	10.7	10.6	10.7	10.6	10.6

Table 3.37: Same as table 3.36 for the analysis of the 2012 dataset.

Contribution / Model	LV38 5ps	LV38 10ps	LV38 50ps	LV98 5ps	LV98 10ps	LV98 50ps	LV198 5ps	LV198 10ps	LV198 50ps
Muon reconstruction	4.5	4.5	4.5	3.9	3.9	3.9	3.9	3.9	3.9
IP cut (Stripping)	1.6	1.1	0.5	1.0	0.4	0.2	0.6	0.5	0.6
Vertex reconstruction	6	6	6	6	6	6	6	6	6
Neural network	1.7	2.9	2.9	3.3	3.2	2.5	3.8	4.9	2.2
Number of tracks cut	5	5	5	5	5	5	5	5	5
Isolation cut	4.3	3.6	3.5	1.5	1.4	1.5	0.7	1.1	1.0
Mass cut	1.1	1.5	0.9	0.9	0.9	1.4	0.8	0.8	1.0
Beam line position	0.2	0.2	0.2	0.6	0.4	0.4	1.0	0.5	0.3
Luminosity	1.16	1.16	1.16	1.16	1.16	1.16	1.16	1.16	1.16
Total	10.5	10.4	10.2	9.6	9.5	9.4	9.7	10.2	9.2

3.5.1 Muon reconstruction

The muon reconstruction efficiency ϵ^{rec} can be factorized into the product of the trigger efficiency ($L0 \times H1t1 \times H1t2$), the efficiency to identify a long track as a muon, and the track reconstruction efficiency:

$$\epsilon^{rec} = \epsilon^{trig} \times \epsilon^{id} \times \epsilon^{trck}$$

ϵ^{rec} is determined by a tag and probe method performed on $Z \rightarrow \mu\mu$ events, similar to the analysis of Ref. [48]. As a control, the procedure has been first performed on the 2011 data and simulated events with exactly the same selection used in the quoted analysis note. Subsequently, the selection criteria on the muons are adjusted to the conditions used in this analysis: in particular, the p_T threshold has been lowered to 10 GeV/c.

The MC simulation and data events are triggered by the L0Muon, Hlt1SingleMuonHighPT and Hlt2SingleMuonHighPT, and preselected by the StrippingZ02MuMuLine which ask for two muons in the LHCb acceptance, with transverse momentum greater than 3 GeV/c². In addition, the $Z \rightarrow \mu\mu$ events are required to fall in a mass window of $60 < M_{\mu\mu} < 120$ GeV/c² and the vertex quality $\chi^2_{vtx}/nDoF < 5$.

The contributions to the muon reconstruction efficiency uncertainties are discussed in the following sections and are summarized on Table 3.38. As no significant differences have been observed between 2011 and 2012 data or Monte Carlo simulation for $Z \rightarrow \mu\mu$ events, and motivated by the results of Ref. [48], the values obtained from the 2011 dataset are also used for 2012.

Table 3.38: Systematic contributions from the different step of the muon reconstruction efficiency.

	$m_{LLP} < 90$ GeV/c ²	$m_{LLP} > 90$ GeV/c ²
Trigger	3 %	3 %
Muon identification	3 %	2 %
Track reconstruction	1.5 %	1.5 %
Total	4.5 %	3.5 %

3.5.1.a Muon Trigger study by tag and probe

One of the two well identified muons, the “tag” is required to fire the trigger lines described above and to pass the conditions detailed on Table 3.39 (which are the preselection conditions of this analysis). The “probe” is selected by the same quality criteria. The distributions of the Z reconstructed mass and of the probe transverse momentum for 2011 data and simulated events are presented on Figure 3.41. The analysis described in Ref. [48] has demonstrated that the background contamination is negligible, less than 0.2 %. The trigger efficiency is defined by the ratio between the number of probe candidates passing the three trigger stages and the number of tag muons. On Figure 3.42, the muon trigger efficiency is shown for the 2011 data and Monte Carlo, for 14 p_T bins. The discrepancy between simulation and data is always less than 3 %. This value is taken as contribution to the uncertainty.

3.5. Detection efficiency and systematic effects

Table 3.39: Muon selections criteria for the tag and probe procedure.

Tag	Probe
Triggered	-
IsMuon	IsMuon
$p_T > 10 \text{ GeV}/c^2$	
$\sigma(P^\mu)/P^\mu < 0.1$	
$E(Ecal)/P^\mu + E(Hcal)/P^\mu < 0.04$	
$\chi^2/nDoF < 2$	
$2 < \eta < 4.5$	

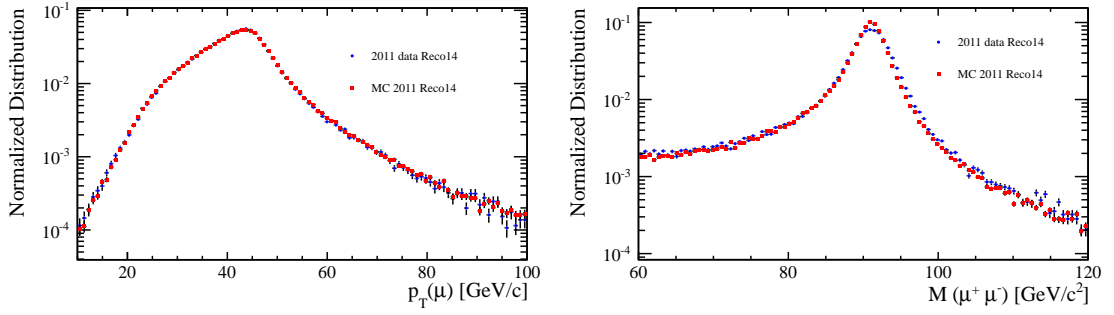


Figure 3.41: Left, transverse momentum of the probed muon and, right, dimuon mass for data and simulated events.

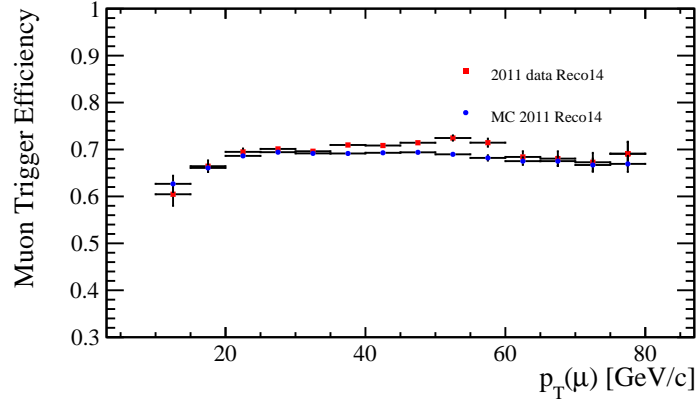


Figure 3.42: Trigger efficiency as a function of the muon transverse momentum determined by the tag and probe technique for data and simulated events.

3.5.1.b Muon identification efficiency

The muon identification efficiency has also been determined from the tag and probe procedure. The probe is a long track with the requirements given in Table 3.40. The identification efficiency

is the fraction of probes recognized as muons (by the "IsMuon" flag). On Figure 3.43, the muon identification efficiency is given for the 2011 dataset and simulated events, at different p_T bins. As already observed in Ref. [48], the efficiency drops for momentum below 40 GeV/c. A maximal discrepancy between simulation and data of 3 % is observed for low p_T . A 3 % systematic uncertainty is assumed for the neutralino mass of 38 GeV/c², and 2 % for higher masses.

Table 3.40: Selections criteria for the determination of the muon identification efficiency.

Tag	Probe
Long Track	Long Track
Triggered	-
IsMuon	-
$p_T > 10 \text{ GeV/c}^2$	
$\sigma(P^\mu)/P^\mu < 0.1$	
$E(Ecal)/P^\mu + E(Hcal)/P^\mu < 0.04$	
$\chi^2/nDoF < 2$	
$2 < \eta < 4.5$	

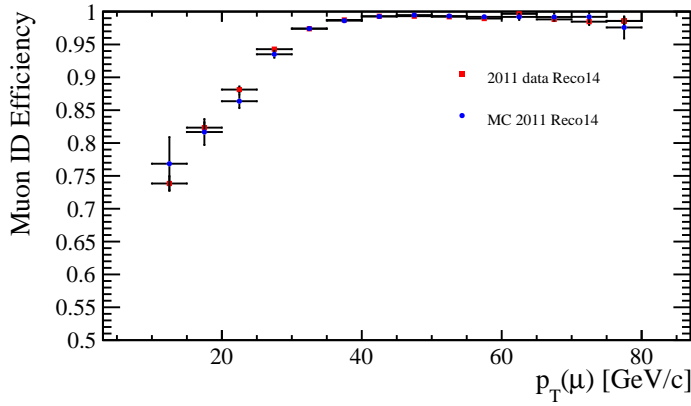


Figure 3.43: Muon identification efficiency as a function of the muon transverse momentum determined by the tag and probe technique, for data and simulated events.

3.5.1.c Muon track Reconstruction efficiency

The track reconstruction for low p_T and high p_T muons has been studied in LHCb with tag and probe analysis performed with $J/\psi \rightarrow \mu\mu$ and $Z \rightarrow \mu\mu$ respectively [49, 48]. From these results, a maximal systematic effect of 1.5% on the muon track reconstruction efficiency is assumed.

3.5.1.d Muon impact parameter

Muons with an impact parameter larger than 0.25 mm are selected at the stripping level. The systematic uncertainty has been determined by comparing the impact parameter distribution of high p_T muon in the simulation and in data for $Z \rightarrow \mu\mu$ events, Figure 3.44. The MC/data ratio is also shown. The data and MC distribution averages differ by less than $20 \mu\text{m}$ which correspond to a 9 % discrepancy. Therefore, the systematic uncertainty has been estimated by moving the muon IP cut by this amount. The results for the different models are summarized in Table 3.41.

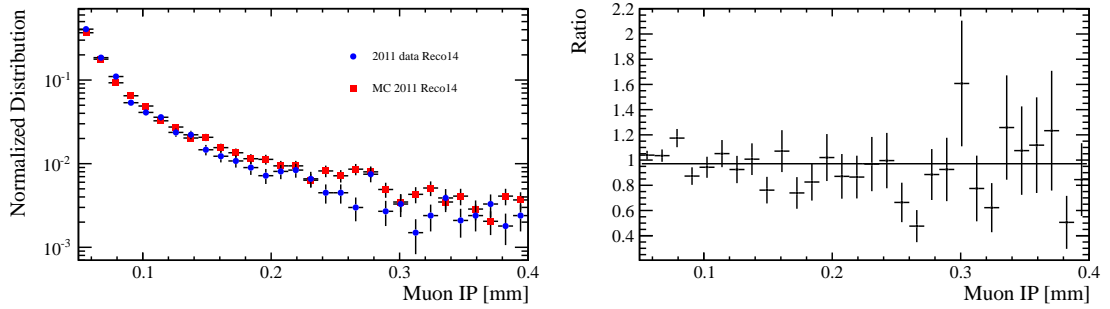


Figure 3.44: Left: muon impact parameter distribution in Monte Carlo and data for $Z \rightarrow \mu\mu$ events. Right: ratio Data/MC.

Table 3.41: Systematic contributions in percent associated to the impact parameter selection.

	2011	2012
LV38 , $\tau = 5 \text{ ps}$	1.6	1.6
LV38 , $\tau = 10 \text{ ps}$	0.9	1.1
LV38 , $\tau = 50 \text{ ps}$	0.5	0.5
LV98 , $\tau = 5 \text{ ps}$	1.1	1.0
LV98 , $\tau = 10 \text{ ps}$	0.5	0.4
LV98 , $\tau = 50 \text{ ps}$	0.4	0.2
LV198 , $\tau = 5 \text{ ps}$	0.7	0.6
LV198 , $\tau = 10 \text{ ps}$	0.6	0.5
LV198 , $\tau = 50 \text{ ps}$	0.4	0.6

3.5.1.e Muon transverse momentum

The mean of the transverse momentum distributions for data and simulation of Figure 3.41 for $Z \rightarrow \mu^+ \mu^-$ events differ by less than $900 \text{ MeV}/c$. From this comparison, a maximal contribution to uncertainty of 2 % is inferred. Figure 3.45 shows the ratio Data/MC.

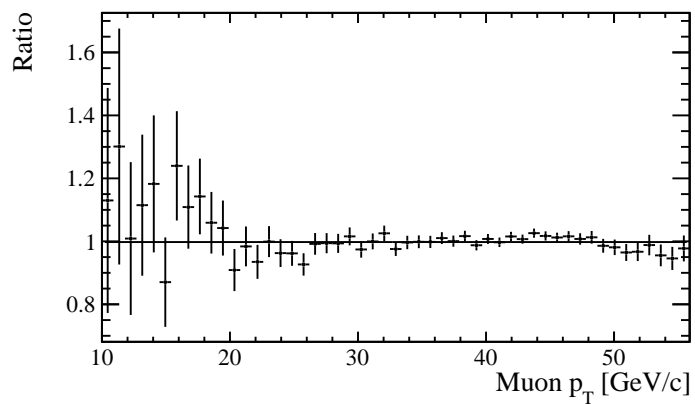


Figure 3.45: Data/MC ratio of the muon p_T distributions for $Z \rightarrow \mu\mu$ events.

3.5.2 Displaced vertex reconstruction

The vertex finding efficiency of the displaced vertex algorithm has been studied on well reconstructed $B^0 \rightarrow J/\psi K^{*0}$. A procedure similar to the one presented in the appendix of Ref. [5] has been adopted. This decay provides a large amount of candidates easily isolated from the combinatorial background. Furthermore, the B^0 gives rise to a vertex with four tracks through the decay of the J/ψ into muons and the K^{*0} into a charged kaon and a pion. The determination of the vertex finding efficiency has been made in two steps. First, B^0 candidates from the stripping line `BetaSBd2JpsiKstarDetachedLine` are selected with a minimal radial distance to the beam line of 0.2 mm and a maximal $\chi^2/nDoF < 5$ for the vertex fit ("decaytreefitter") with a PV constraint. In addition, events are required to pass `Hlt1DiMuonHighMass` and (`Hlt2DiMuonJPsi` or `Hlt2DiMuonDetachedJPsi`) trigger lines. These requirements aims to reduce the combinatorial background significantly and provides well reconstructed vertices with a very good quality. Then, the Displaced Vertex (DV) algorithm presented in section 3.3.2.b is applied to the exclusive B^0 candidates with the following tuning:

- the DV is reconstructed with exactly 4 tracks,
- at least one muon with $p_T > 100 \text{ MeV}/c$ is required,
- a minimal p_T of the B^0 candidates of $3 \text{ GeV}/c$ is required,
- the MV selection is active,
- The DV must have a minimal radial distance of 0.2 mm from the beam line.

The B^0 mass distributions for exclusive B^0 candidates and inclusive candidates reconstructed with the displaced vertex algorithm are presented on Figure 3.46 for the 2011 dataset and simulated events. The results for the 2012 dataset are presented on Figure 3.47 as well. The displaced vertex efficiency is subsequently defined by the number of inclusive signal candidates divided by the number of exclusive candidates. The number of signal candidates and the corresponding re-weighted kinematical distributions have been determined by the *sPlot* technique [50]. A double Gaussian with a common mean for the signal peak plus an exponential background have been used to model the $B^0 \rightarrow J/\psi K^{*0}$ mass distribution [51]. On Figures 3.48, 3.49, and 3.50, the data and Monte Carlo vertex finding efficiency are given as a function of η , p_T , R and number of primary vertices. A maximal discrepancy of 8% for the 2011 dataset, and 6% for the 2012 dataset, is observed and adopted as a contribution to systematics. As mentioned in [5], the losses in the vertex finding efficiency occurs mostly because tracks that belong to the "signal" vertex are erroneously assigned to another vertex. Note that the events chosen for this test provide the worst-case scenario, where the loss of only one track leads to a substantial efficiency drop. As the different LV signal models have a higher track multiplicity than $B^0 \rightarrow J/\psi K^{*0}$, the systematic uncertainty contribution on the signal efficiency of the vertex finding algorithm is therefore overestimated by this study.

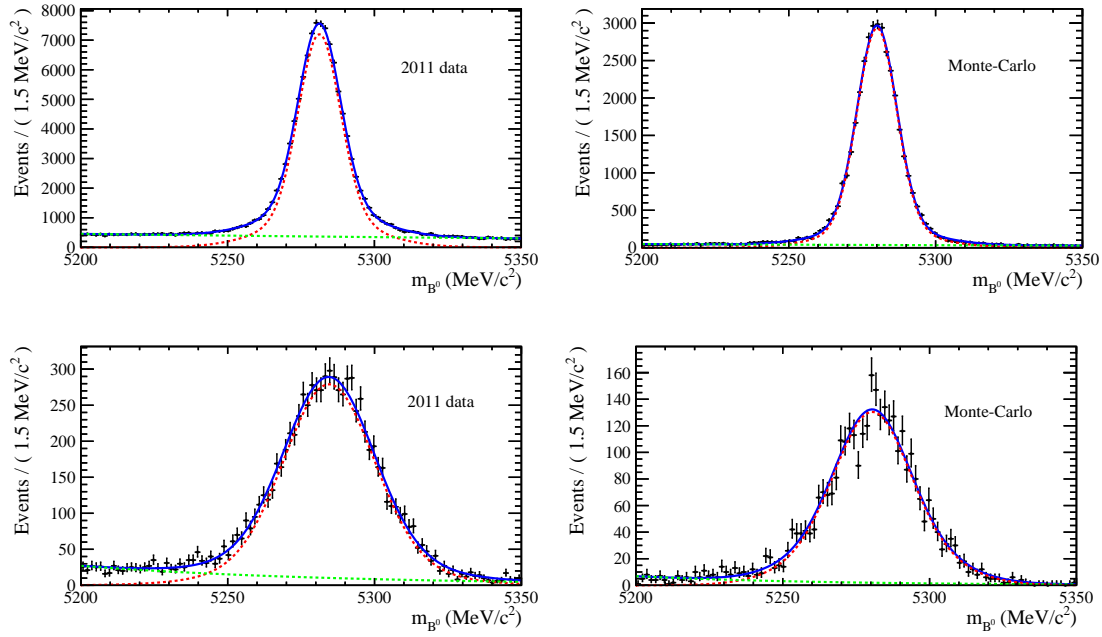


Figure 3.46: Top, mass fit of B^0 exclusive candidates and, bottom, inclusive candidates reconstructed with the displaced vertex algorithm. At the left, the 2011 data, at right the simulation. In green, the exponential shape which models the combinatorial background. In red, the signal peak modelled by two gaussian. In blue, the total fitted function.

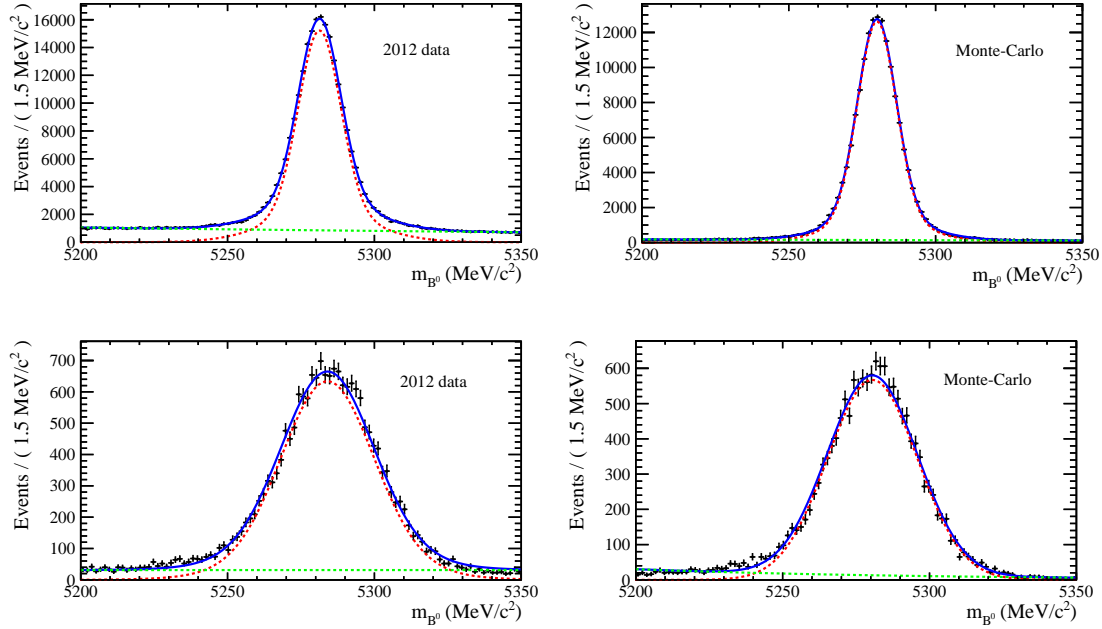


Figure 3.47: Like Figure 3.46, for the analysis of 2012 data.

3.5. Detection efficiency and systematic effects

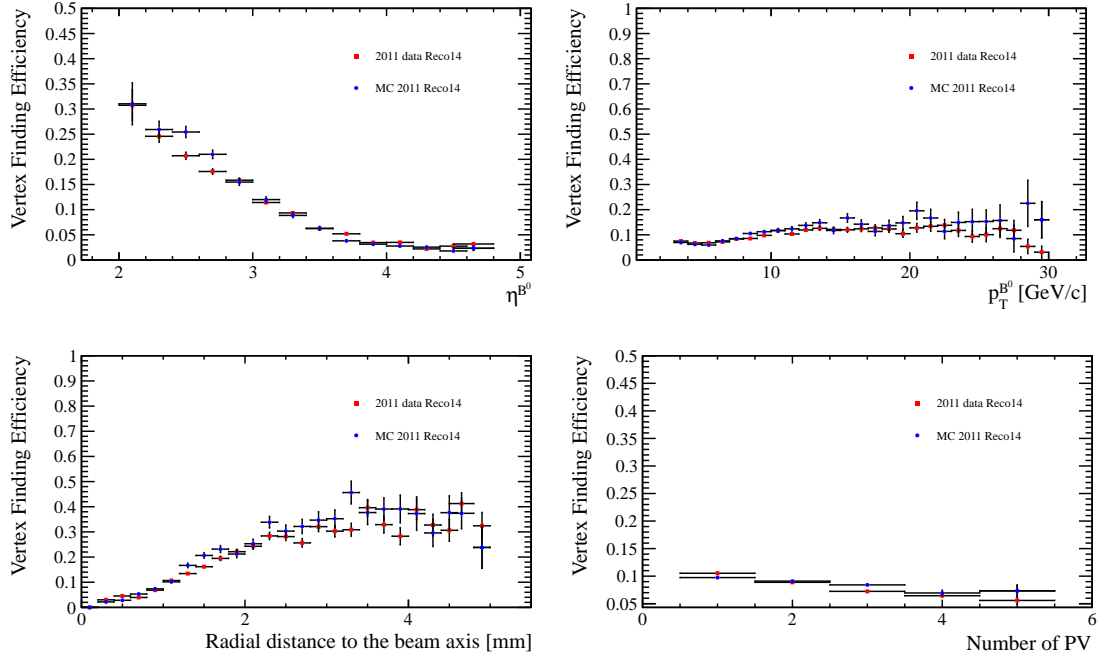


Figure 3.48: Comparison of the vertex finding efficiency for data and simulated events, from the analysis of B^0 candidates as a function of η (top left), p_T (top right), R distance to the beam axis (bottom left) and the number of primary vertices (bottom right). A reweighting procedure is performed to match the signal kinematics.

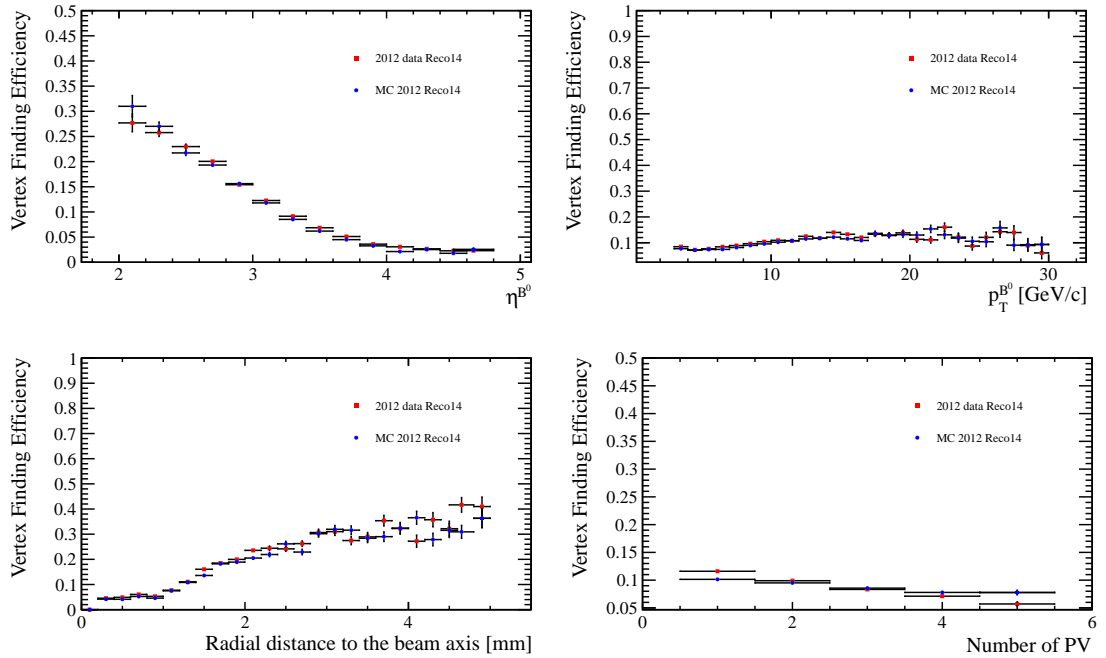


Figure 3.49: Like Figure 3.48 for the 2012 data analysis.

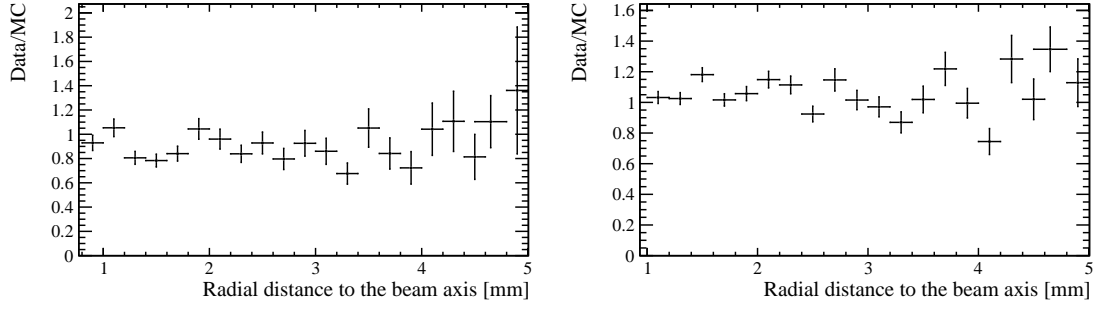


Figure 3.50: Data/MC ratio of the vertex finding efficiency as a function of the distance to the beam axis. 2011 data at left, and 2012 data at right.

3.5.2.a Radial dependency

A study about the efficiency to detect secondary vertices as a function of the radial distance can be found in the note Ref. [51], about the b-hadron lifetime measurement. The kaon track detection efficiency has been studied as a function of the DV radial distance for $B^+ \rightarrow J/\psi K^+$. In the note, the figures 46 and 51 show the efficiency for the data and simulation for online and offline reconstruction. The efficiency decreases by $\sim 30\%$ at $R = 5\text{ mm}$ for the online reconstruction, while the offline only losses 10% . Nevertheless the simulation agrees with the data within $\sim 3\%$ up to $4 - 5\text{ mm}$, as one can see from the plots on Figure 3.51, showing the MC/data ratio. A maximal discrepancy of 5% has been adopted into account to deal with the few events reconstructed above 5 mm . Integrating over the R distributions for the different LV models, the contribution of this source of systematics is totally negligible.

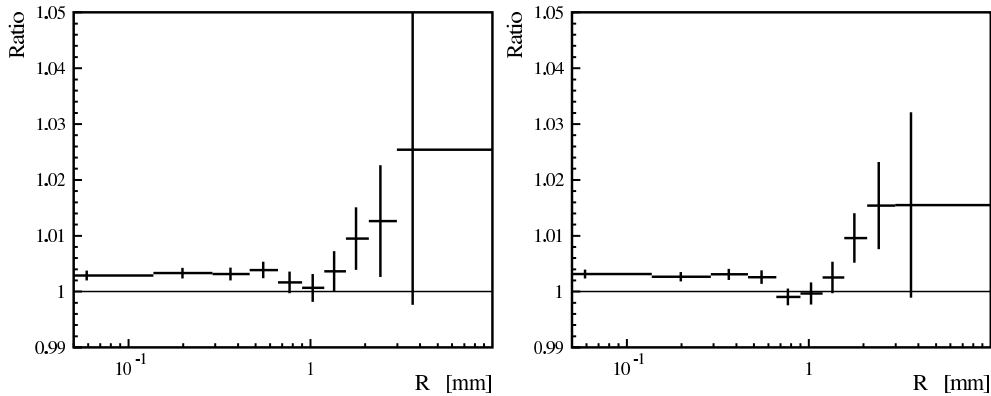


Figure 3.51: MC/data ratio of the reconstruction efficiency for kaon tracks reconstructed using the online (left plot) and offline (right plot) algorithms as a function of the radial distance R .

3.5.3 Neural Network Classifier

The imprecision of the models used to train the MLP is source of a contribution to the systematics uncertainties. The potential biases on the input variables are:

- the precision on the muon impact parameter is 9 %, and on the muon transverse momentum 2 %, as discussed in Section 3.5.1.d and 3.5.1.e respectively ,
- the precision on the σ_R , σ_Z and N_{tracks} variables: 3 %, 4 % and 5 % respectively are obtained by comparison of data and Monte Carlo distributions at the preselection stage (Section 3.3.4). These values are the same as in Ref. [6],
- for the radial distance to the beam axis R an uncertainty of 5 % is inferred from the study presented in Section 3.5.2.a.

In order to study the effect on the MLP selection, toy experiments are performed. At the MLP test stage each input variable is modified by a scale factor randomly selected in a Gaussian distribution of width equal to the corresponding bias. For each LV model, the effect is determined after the LLP mass fit, as explained in Section 3.4.1.a. The RMS of the signal efficiency distribution after the MLP filter is taken as systematic uncertainty as summarized in Table 3.42.

For illustration, the distribution of the different biases are presented on Figure 3.52 for the 2011 data and LV38 ($\tau = 5$ ps). The distribution of the difference between the signal efficiency $\epsilon_{MLP,true}$ determined without bias and the efficiency $\epsilon_{MLP,Toy}$ from a biased sample is shown on Figure 3.53. For this example, an uncertainty of 1.2 % has been estimated. In addition, the scatter plot of the difference in efficiency versus the bias introduced is shown for each variables on Figure 3.54, showing a considerable sensitivity of the MLP on the LLP number of tracks.

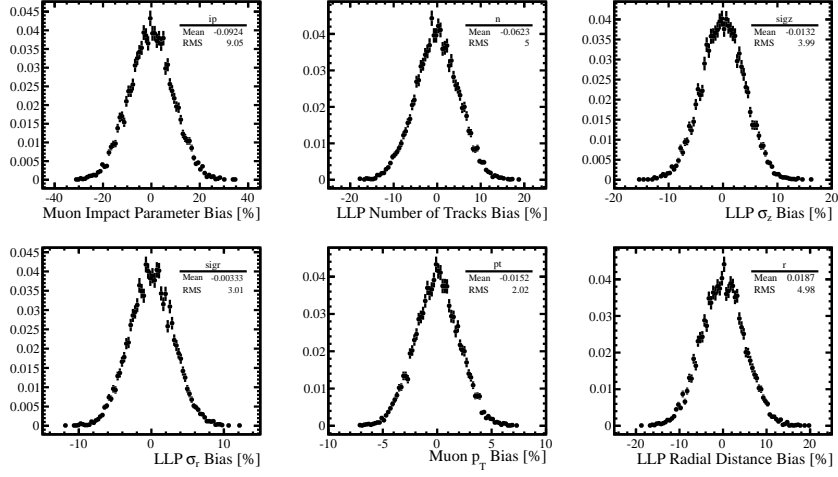


Figure 3.52: Biases introduced at the testing stage of the MLP, corresponding to each input variables. 10000 toy experiments have been generated.

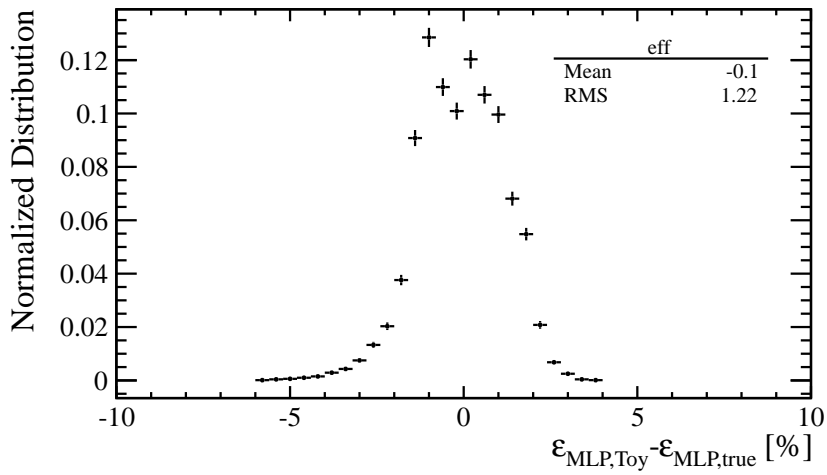


Figure 3.53: Difference between efficiency measured in the toy study and the efficiency obtained without any bias.

3.5. Detection efficiency and systematic effects

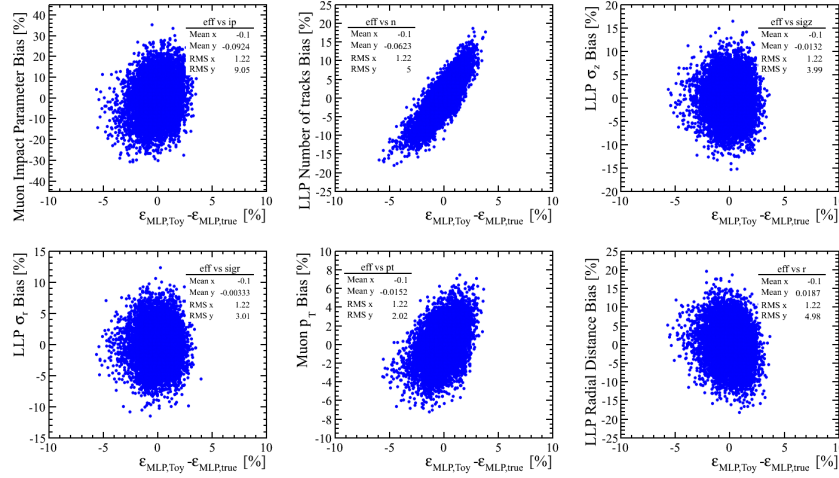


Figure 3.54: For each MLP input, the abscissa of the corresponding scatter plot is the difference between efficiency measured in the toy study with and without bias, for the bias factor given in the ordinate of the plot.

Table 3.42: Contribution to the systematic uncertainty in percent due to the MLP for the different signal models.

	2011	2012
LV38, $\tau = 5$ ps	1.2	1.7
LV38, $\tau = 10$ ps	1.4	2.9
LV38, $\tau = 50$ ps	1.4	2.9
LV98, $\tau = 5$ ps	1.6	3.3
LV98, $\tau = 10$ ps	1.8	3.2
LV98, $\tau = 50$ ps	1.6	2.5
LV198, $\tau = 5$ ps	2.1	3.8
LV198, $\tau = 10$ ps	1.3	4.9
LV198, $\tau = 50$ ps	1.6	2.2

3.5.4 Muon isolation and LLP reconstructed mass

The muon isolation and the LLP reconstructed mass are the variables relevant to both the LLP mass fit and the ABCD method. The systematic uncertainties on the signal efficiency induced by the imprecision on these two variables have been determined by studying the QCD background at the intermediate stage of the analysis. After the suppression of W and Z events and assuming a negligible amounts of signal events, only $b\bar{b}$ events survive, populating the low mass, larger isolation region.

On Figure 3.55, the muon isolation distribution is presented for the 2011 data and $b\bar{b}$ simulated

events. The mean of these two distributions differ by less than 0.1. We recall that the signal and sideband regions are defined by an isolation cut of 1.4. Thus, to estimate the systematic uncertainty induced by a cut on the muon isolation, the cut value is moved by ± 0.1 and the efficiency is compared to the nominal value. On Table 3.43, the variations for each signal model are given. The maximal variation for each couple of is considered as contribution to the systematic uncertainty.

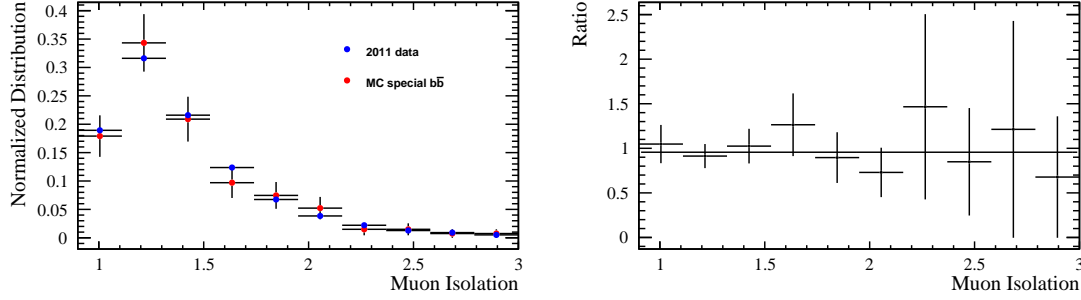


Figure 3.55: Left: Muon isolation distribution for 2011 data and $b\bar{b}$ simulated events. Right: ratio of the two distributions fitted by a constant.

Table 3.43: Systematic contributions in percent to the muon isolation selection for the different signal models computed by taking the difference in efficiencies induced by a cut variation of ± 0.1 for 2011 and 2012 analysis.

	2011	2012
LV38 , $\tau = 5 \text{ ps}$	(-3.5, +2.8)	(-4.3, +3.6)
LV38 , $\tau = 10 \text{ ps}$	(-3.0, +2.6)	(-3.6, +2.9)
LV38 , $\tau = 50 \text{ ps}$	(-3.1, +2.5)	(-3.5, +1.5)
LV98 , $\tau = 5 \text{ ps}$	(-1.1, +1)	(-1.5, +1.1)
LV98 , $\tau = 10 \text{ ps}$	(-1.0, +0.5)	(-1.4, +0.9)
LV98 , $\tau = 50 \text{ ps}$	(-1.2, +0.7)	(-1.5, +0.6)
LV198 , $\tau = 5 \text{ ps}$	(-0.8, +0.6)	(-0.7, +0.5)
LV198 , $\tau = 10 \text{ ps}$	(-1.0, +0.5)	(-1.1, +0.7)
LV198 , $\tau = 50 \text{ ps}$	(-1.1, +0.7)	(-1.0, +0.3)

The same procedure is used for the LLP mass. On Figure 3.56, the comparison and the ratio between the LLP reconstructed mass distribution for 2011 data and the $b\bar{b}$ Monte-Carlo sample are shown. We recall that at the preselection stage a minimal reconstructed mass of $4.5 \text{ GeV}/c^2$ is required. The MC and data distributions differ by less than $1 \text{ GeV}/c^2$. Therefore, the systematic uncertainty on the signal efficiency has been evaluated by varying the mass cut by this amount. The results are given on Table 3.44.

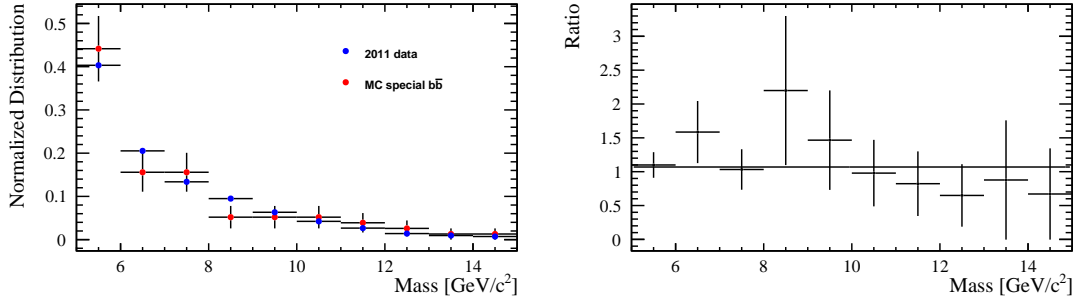


Figure 3.56: Left: LLP reconstructed mass distribution for 2011 data and the special $b\bar{b}$ Monte-Carlo sample. Right: ratio of the two distributions with a constant fit.

Table 3.44: Systematic contributions in percent on signal efficiency in percent caused by the LLP reconstructed mass cut for the different signal model estimated by taking the difference in efficiency induced by a mass cut variation of 1 GeV/c².

	2011	2012
LV38 , $\tau = 5$ ps	1.4	1.1
LV38 , $\tau = 10$ ps	2.0	1.5
LV38 , $\tau = 50$ ps	2.5	0.9
LV98 , $\tau = 5$ ps	1.2	0.9
LV98 , $\tau = 10$ ps	1.4	0.9
LV98 , $\tau = 50$ ps	1.3	1.4
LV198 , $\tau = 5$ ps	1.3	0.8
LV198 , $\tau = 10$ ps	1.3	0.8
LV198 , $\tau = 50$ ps	1.2	1.0

3.5.5 Beam line position

A 10 μm inaccuracy in the position of the beam line has been assumed as presented in Ref. [6]. On Table 3.45, the change in efficiency by moving the radial cut of the LLP by that amount is presented for each signal models.

Table 3.45: Systematic contributions on signal efficiency in percent caused by the beam line position by taking the difference in efficiency induced by a radial cut variation of $10 \mu m$.

	2011	2012
LV38 , $\tau = 5 ps$	0.2	0.2
LV38 , $\tau = 10 ps$	0.2	0.2
LV38 , $\tau = 50 ps$	0.1	0.2
LV98 , $\tau = 5 ps$	0.6	0.6
LV98 , $\tau = 10 ps$	0.5	0.4
LV98 , $\tau = 50 ps$	0.3	0.4
LV198 , $\tau = 5 ps$	0.8	1.0
LV198 , $\tau = 10 ps$	0.7	0.5
LV198 , $\tau = 50 ps$	0.5	0.3

3.5.6 Luminosity

Integrated luminosity of $0.98 fb^{-1}$ and $1.98 fb^{-1}$ have been analyzed in 2011 and 2012. The uncertainties on the integrated luminosities determined by a precision measurement presented in [52] are 1.7 % for 2011 dataset and 1.16 % for 2012 dataset.

3.6 Upper limit on production cross-section

The 95% CL upper limits on the production cross-sections, σ_{up} , has been computed from the results of the LLP mass fit for the different signal model considered in this analysis. The CL_s techniques has been applied to the results of the fit and to the ABCD results as well. This statistical test is using the profile likelihood ratio Q [53]:

$$Q = \frac{\mathcal{L}(\text{signal} + \text{background})}{\mathcal{L}(\text{background})}$$

where $\mathcal{L}(\text{background})$ denotes the likelihood corresponding to the background only hypothesis (alternative hypothesis) while $\mathcal{L}(\text{signal} + \text{background})$ is the likelihood of the null hypothesis where a signal component is needed to understand the data. The likelihood are computed for the fit results presented on Section 3.4.1.a. The ratio Q is scanned and evaluated for different values of the production cross-section σ where the statistical test is performed on pseudo-datasets generated from the background model (σ fixed at 0) and for the signal+background hypotheses (σ fixed to the evaluated value).

The consistency test for the background only hypothesis, CL_b , is defined as:

$$1 - CL_b = \int_{-\infty}^{Q_{obs}} P(Q' | \text{background}) dQ'$$

with Q_{obs} the observed profile likelihood ratio.

The background+signal consistency test, CL_{s+b} hypothesis, is defined as :

$$CL_{s+b} = \int_{Q_{obs}}^{+\infty} P(Q' | \text{signal} + \text{background}) dQ'$$

Therefore, the confidence level CL_s is :

$$CL_s = \frac{CL_{s+b}}{CL_b}$$

where $CL_s > 0.05$ corresponds to a 95 % confidence level.

The first steps of the algorithm implemented with the *RooStat* tools [54] are illustrated on Figure 3.57. The tool scans the production cross-section from zero and computes the profile likelihood ratio for background only hypothesis (BModel), for signal plus background hypothesis (SbModel) and the observed profile likelihood ratio. At each steps, the CL_s ratio is determined until it reaches 0.05 for a given value of σ defining the upper limit on the production cross-section, as it is shown on Figure 3.58, where the p-value for the different hypotheses is given as a function of the production cross-section. Statistical and systematic uncertainties on the signal efficiencies have been injected as nuisance parameters of the likelihood function, assuming Gaussian distributions.

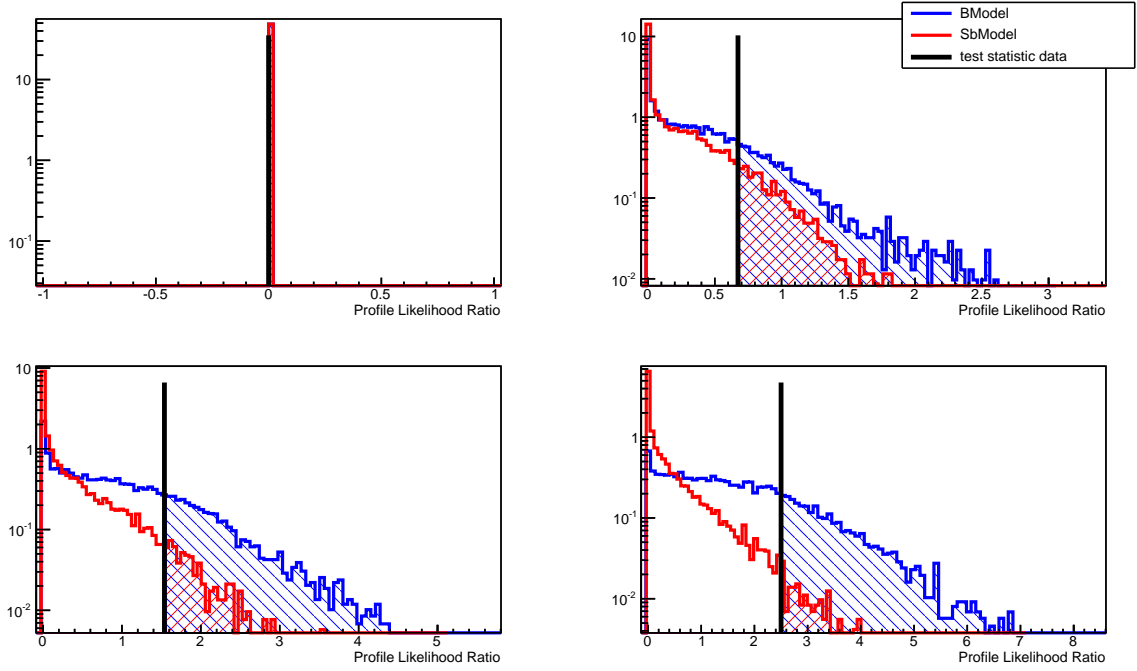


Figure 3.57: Illustration of the first steps of the CL_s algorithm. In blue: the profile likelihood ratio for background only hypothesis ($\sigma = 0$). In red: the profile likelihood ratio for signal plus background hypothesis for a given value of σ . In black: the observed profile likelihood ratio. Each bins contain the results from pseudo-datasets generated from the background model.

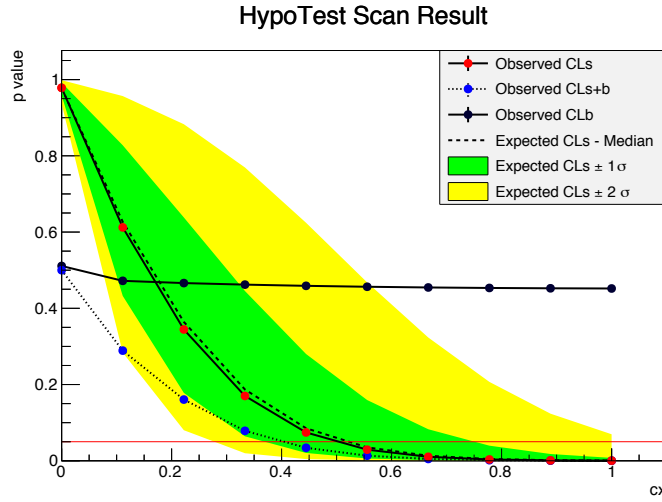


Figure 3.58: Frequentist scan of the CL_s algorithm for 2011 data analysis, and the LV38 ($\tau = 10$ ps) signal model. cx refers to the production cross-section in pb .

On Table 3.46 and 3.47, the upper limits on the production cross-sections computed from the fitting method and the CL_s procedure are presented for 2011 and 2012 data analysis, together

3.6. Upper limit on production cross-section

with the selection efficiency for each full simulated models.

Table 3.46: Detection efficiency and upper limit on the production cross-section, σ_{up} , from the 2011 dataset and for each signal model, computed from the LLP mass fit results. The uncertainties on the efficiency are statistical only.

Model	$\epsilon_{sel}[\%]$	$\sigma_{up}^{LHCb} [pb]$	$\sigma_{up}^{4\pi} [pb]$
LV38 , $\tau = 5 ps$	4.54 ± 0.10	0.63	5.69
LV38 , $\tau = 10 ps$	5.32 ± 0.11	0.50	4.51
LV38 , $\tau = 50 ps$	3.62 ± 0.09	0.54	4.79
LV98 , $\tau = 5 ps$	5.23 ± 0.12	0.14	1.27
LV98 , $\tau = 10 ps$	6.84 ± 0.12	0.13	1.15
LV98 , $\tau = 50 ps$	5.03 ± 0.11	0.17	1.53
LV198 , $\tau = 5 ps$	5.38 ± 0.11	0.11	0.99
LV198 , $\tau = 10 ps$	6.80 ± 0.12	0.09	0.81
LV198 , $\tau = 50 ps$	4.87 ± 0.13	0.12	1.08

Table 3.47: Like table 3.46, for the 2012 dataset.

Model	$\epsilon_{sel}(\%)$	$\sigma_{up}^{LHCb} [pb]$	$\sigma_{up}^{4\pi} [pb]$
LV38 , $\tau = 5 ps$	3.61 ± 0.09	0.51	4.20
LV38 , $\tau = 10 ps$	5.40 ± 0.11	0.31	2.54
LV38 , $\tau = 50 ps$	4.71 ± 0.11	0.34	2.76
LV98 , $\tau = 5 ps$	6.46 ± 0.13	0.09	0.74
LV98 , $\tau = 10 ps$	8.13 ± 0.14	0.07	0.58
LV98 , $\tau = 50 ps$	5.77 ± 0.12	0.11	0.90
LV198 , $\tau = 5 ps$	6.54 ± 0.13	0.04	0.33
LV198 , $\tau = 10 ps$	8.43 ± 0.14	0.06	0.49
LV198 , $\tau = 50 ps$	5.84 ± 0.12	0.09	0.76

For the ABCD method, the likelihood ratio has been build from the Poisson distribution for background only and for signal and background hypotheses. Indeed, the ABCD method can be considered as a counting experiment in the region C where an expected number of background and signal events are compared with an observed number of events in 2011 and 2012 data. Therefore, the likelihood ratio is defined in terms of probability P_{poiss} as follow:

$$Q = \frac{P_{poiss}(\text{data}|\text{signal} + \text{background})}{P_{poiss}(\text{data}|\text{background})}$$

Chapter 3. Search for long-lived particles decaying semileptonically

where $P_{\text{poiss}}(\text{data}|\text{signal} + \text{background})$ denotes the probability to observed N events of background in the data given N_s signal events plus N_{bkg} background events.

The consistency tests in terms of probabilities are:

$$1 - CL_b = P(Q \geq Q_{obs}|\text{background})$$

and

$$CL_{s+b} = P(Q \leq Q_{obs}|\text{signal} + \text{background})$$

As for the CL_s algorithm performed on the results of the fitting method, the nuisance parameters have been considered as Gaussian constraints.

On Table 3.48 and 3.49, the upper limits on the production cross-section in the LHCb forward region computed from the ABCD method and the CL_s procedure are presented for 2011 and 2012 data analysis together with the selection efficiency on each full simulated models.

Table 3.48: Detection efficiency and upper limits on the production cross-section, σ_{up} , from the 2011 dataset and for each signal model computed from the ABCD results. The errors on the efficiency are statistical only.

Model	$\epsilon_{sel}^{ABCD}(\%)$	$\sigma_{up} [pb]$
LV38 , $\tau = 5 \text{ ps}$	2.49 ± 0.08	0.34
LV38 , $\tau = 10 \text{ ps}$	2.95 ± 0.08	0.35
LV38 , $\tau = 50 \text{ ps}$	1.86 ± 0.07	0.46
LV98 , $\tau = 5 \text{ ps}$	3.80 ± 0.10	0.21
LV98 , $\tau = 10 \text{ ps}$	4.85 ± 0.10	0.18
LV98 , $\tau = 50 \text{ ps}$	3.50 ± 0.09	0.28
LV198 , $\tau = 5 \text{ ps}$	3.56 ± 0.09	0.15
LV198 , $\tau = 10 \text{ ps}$	4.59 ± 0.10	0.09
LV198 , $\tau = 50 \text{ ps}$	3.30 ± 0.09	0.20

3.6. Upper limit on production cross-section

Table 3.49: Like table 3.48 for the 2012 dataset

Model	$\epsilon_{sel}^{ABCD}(\%)$	$\sigma_{up} [pb]$
LV38 , $\tau = 5 \text{ ps}$	2.67 ± 0.08	0.35
LV38 , $\tau = 10 \text{ ps}$	2.96 ± 0.09	0.31
LV38 , $\tau = 50 \text{ ps}$	1.91 ± 0.07	0.44
LV98 , $\tau = 5 \text{ ps}$	4.70 ± 0.11	0.13
LV98 , $\tau = 10 \text{ ps}$	6.03 ± 0.12	0.08
LV98 , $\tau = 50 \text{ ps}$	4.70 ± 0.10	0.10
LV198 , $\tau = 5 \text{ ps}$	4.74 ± 0.11	0.08
LV198 , $\tau = 10 \text{ ps}$	6.00 ± 0.12	0.06
LV198 , $\tau = 50 \text{ ps}$	4.12 ± 0.10	0.08

4 Conclusion and Perspectives

This thesis work is dedicated to the search for neutralino decaying semileptonically into Standard Model particles. This decay can occur through R-parity violation in the mSUGRA theoretical framework. A displaced vertex reconstructed with several tracks accompanied by a muon is the signature of neutralinos decaying semileptonically, with lepton number violation. Although the LHCb detector has been build for the b or c -hadrons studies, the excellent vertex position resolution provided by the VELO as well as the p_T requirements of the muon trigger system allowed to study unexplored regions of the SUSY parameter space.

It has been observed that the background is dominated by $b\bar{b}$ events together with a small contribution of W and Z bosons decays close to the interaction point. A neural network classifier which takes as input variables the muon and the displaced vertex properties is used for the selection of candidates.

The signal is determined by a fit of the LLP mass distribution, and , as a cross-check by the ABCD method, based on the LLP mass and the muon isolation variable.

In both cases, in the absence of a sufficient amount of simulated background, a data driven approach is used to determine the background characteristics.

The procedure has been successfully tested on W and Z decays.

Data samples with a size of 0.98 fb^{-1} and 1.98 fb^{-1} collected at a center-of-mass energy of $\sqrt{s} = 7 \text{ TeV}$ and 8 TeV in 2011 and 2012 have been analyzed. The results are consistent with zero signal events for the set of models studied. Thereby, upper limits on the production cross sections from 0.06 to 0.46 pb were set for a total selection efficiency from 1.9 to 6.0 %.

A fast simulation is in preparation in order to cover and study a larger region of the mSUGRA parameter space as presented on Figure 4.1. This method is calibrated by the different results obtained in this thesis work and the same analysis techniques will be performed to set limits on the production cross section.

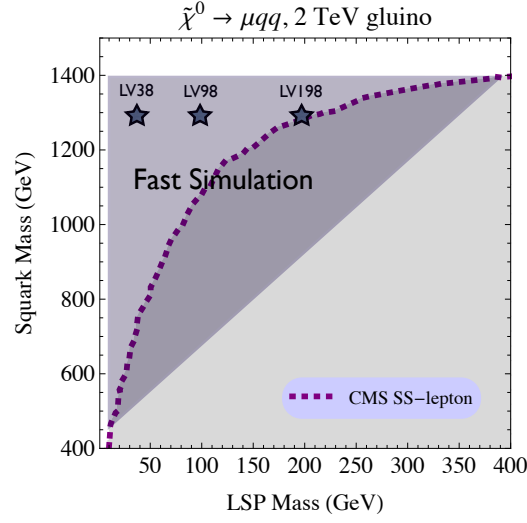


Figure 4.1: Graphs from models considered from the CMS results with the LV models studied in this analysis together with the region of the parameter space targeted by the the fast simulation.

Finally, motivated by the results of this analysis and the future recorded data at a center-of-mass energy of 13 and 14 TeV, it would be interesting to search for neutralino decaying semileptonically into quarks and electrons in addition to muons. The study of this decay channel would be very challenging and may allow to look at large unexplored regions of the parameter space [2].

A Appendix

A.1 Results of the fitting procedure with W and Z events as signal events for 2012 data

The results of the fitting procedure used for the determination of the production cross-sections of $W^+ \rightarrow \mu^+ \nu$ and $W^- \rightarrow \mu^- \nu$ for 2012 data are presented on Figure A.1

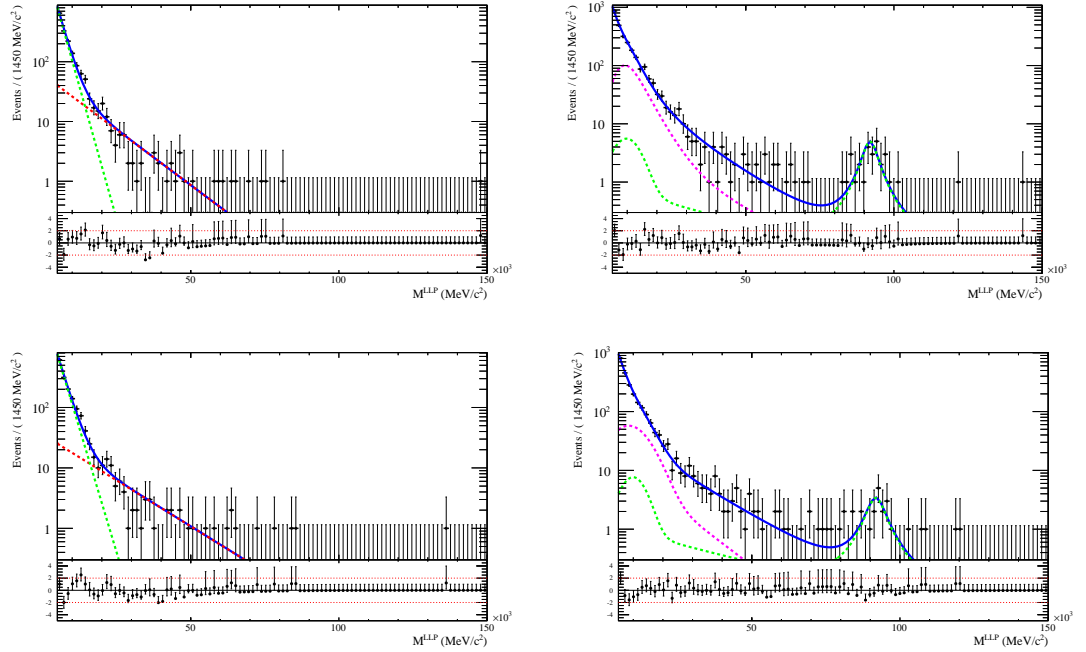


Figure A.1: Same as figure 3.37 for 2012 data.

A.2 Simultaneous fit parameters

The fit parameters of the signal and background model obtained from the simultaneous fit technique are listed for 2011 and 2012 data analysis for each signal models.

Table A.1: Fit parameters of the signal and background model for the analysis of 2011 data and LV38 models together with the $\chi^2/nDoF$.

	LV38 , $\tau = 5 \text{ ps}$	LV38 , $\tau = 10 \text{ ps}$	LV38 , $\tau = 50 \text{ ps}$
τ_{LV}	3769.6 ± 431.5	3346.8 ± 479.5	3310.1 ± 619.2
$\mu_{m_{LLP}, sig}$	14135.0 ± 375.7	15481.4 ± 271.0	14972.8 ± 432.4
$\sigma_{m_{LLP}, sig}$	6772.7 ± 304.2	7080.3 ± 305.6	8180.4 ± 253.4
$\tau_{m_{LLP}}$	7830.2 ± 723.8	7771.2 ± 534.2	7038.4 ± 684.2
r	6.97 ± 1.41	6.32 ± 1.32	7.08 ± 2.22
f_{QCD}	0.99 ± 0.03	0.97 ± 0.02	0.95 ± 0.08
$\chi^2/nDoF$	1.08	0.78	2.20

Table A.2: Same as Table A.1 for LV98 models.

	LV98 , $\tau = 5 \text{ ps}$	LV98 , $\tau = 10 \text{ ps}$	LV98 , $\tau = 50 \text{ ps}$
τ_{LV}	11337.7 ± 1772.5	8937.5 ± 2109.0	8698.4 ± 1987.8
$\mu_{m_{LLP}, sig}$	11982.9 ± 1718.6	12016.6 ± 1712.0	13778.2 ± 1732.4
$\sigma_{m_{LLP}, sig}$	22994.4 ± 1892.9	24778.9 ± 1646.3	27515.0 ± 1047.5
$\tau_{m_{LLP}}$	7971.0 ± 614.8	8279.8 ± 590.0	8049.4 ± 656.6
r	6.16 ± 1.10	4.49 ± 1.46	5.16 ± 3.22
f_{QCD}	0.99 ± 0.02	0.97 ± 0.10	0.96 ± 0.04
$\chi^2/nDoF$	1.56	0.69	0.78

Table A.3: Same as Table A.1 for LV198 models.

	LV198 , $\tau = 5 \text{ ps}$	LV198 , $\tau = 10 \text{ ps}$	LV198 , $\tau = 50 \text{ ps}$
τ_{LV}	36780.6 ± 984.2	34790.2 ± 945.9	32625.5 ± 1184.6
$\mu_{m_{LLP}, sig}$	6403.5 ± 747.4	5401.2 ± 1280.0	5215.9 ± 1182.1
$\sigma_{m_{LLP}, sig}$	5516.1 ± 1419.0	9911.4 ± 1850.5	11462.2 ± 2058.7
$\tau_{m_{LLP}}$	7123.5 ± 476.9	7507.0 ± 505.7	7698.9 ± 631.9
r	6.42 ± 1.12	9.32 ± 2.41	6.82 ± 1.43
f_{QCD}	0.98 ± 0.02	0.97 ± 0.10	0.96 ± 0.08
$\chi^2/nDoF$	0.85	1.26	0.89

A.2. Simultaneous fit parameters

Table A.4: Fit parameters of the signal and background model for the analysis of 2012 data and LV38 models together with the $\chi^2/nDoF$.

	LV38 , $\tau = 5 \text{ ps}$	LV38 , $\tau = 10 \text{ ps}$	LV38 , $\tau = 50 \text{ ps}$
τ_{LV}	4143.4 ± 384.4	4059.6 ± 372.2	3738.6 ± 511.0
$\mu_{m_{LLP},sig}$	14785.2 ± 375.3	14654.2 ± 363.7	15096.8 ± 499.7
$\sigma_{m_{LLP},sig}$	6551.0 ± 286.2	6476.3 ± 275.2	6607.6 ± 355.2
$\tau_{m_{LLP}}$	8534.0 ± 400.1	9076.3 ± 528.7	8883.2 ± 725.0
r	4.21 ± 2.58	6.28 ± 4.38	3.52 ± 2.33
f_{QCD}	0.99 ± 0.02	0.99 ± 0.01	0.96 ± 0.05
$\chi^2/nDoF$	1.84	1.61	2.32

Table A.5: Same as Table A.4 for LV98 models.

	LV98 , $\tau = 5 \text{ ps}$	LV98 , $\tau = 10 \text{ ps}$	LV98 , $\tau = 50 \text{ ps}$
τ_{LV}	11067.5 ± 1263.4	11582.6 ± 1059.6	10294.7 ± 1536.7
$\mu_{m_{LLP},sig}$	17957.0 ± 1146.0	17600.8 ± 978.3	13150.9 ± 1413.4
$\sigma_{m_{LLP},sig}$	20684.8 ± 1216.1	20278.2 ± 1071.6	21505.1 ± 1533.1
$\tau_{m_{LLP}}$	8790.3 ± 556.2	7529.1 ± 489.1	8314.0 ± 576.7
r	3.56 ± 0.96	3.94 ± 3.18	4.45 ± 2.68
f_{QCD}	0.98 ± 0.01	0.97 ± 0.04	0.98 ± 0.02
$\chi^2/nDoF$	2.05	1.87	2.05

Table A.6: Same as Table A.4 for LV198 models.

	LV198 , $\tau = 5 \text{ ps}$	LV198 , $\tau = 10 \text{ ps}$	LV198 , $\tau = 50 \text{ ps}$
τ_{LV}	33294.6 ± 3070.5	31552.6 ± 3253.6	33947.8 ± 3537.2
$\mu_{m_{LLP},sig}$	5823.5 ± 649.5	5395.5 ± 623.6	5305.3 ± 841.3
$\sigma_{m_{LLP},sig}$	4149.3 ± 561.2	5733.1 ± 891.7	4733.1 ± 898.2
$\tau_{m_{LLP}}$	7913.1 ± 645.1	7066.0 ± 419.9	8830.1 ± 580.6
r	8.01 ± 5.09	4.77 ± 1.34	3.94 ± 2.49
f_{QCD}	0.99 ± 0.01	0.99 ± 0.06	0.99 ± 0.02
$\chi^2/nDoF$	1.47	1.59	2.02

A.3 Multilayer Perceptron response

The overtraining checks and the selection applied on the neural network response of the multilayer perceptron of the different signal models are presented for 2011 and 2012 data analysis.

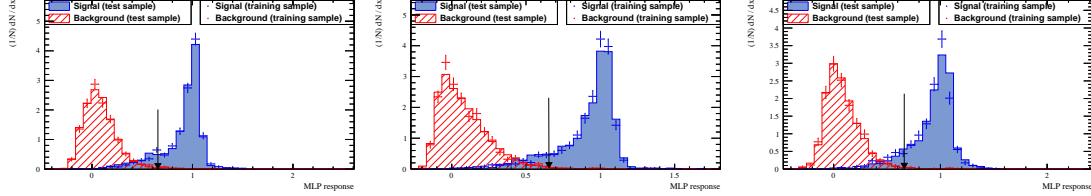


Figure A.2: Overtraining check of the MLP classifier for 2011 data and $LV38$ signal models together with the MLP response selection applied for the signal extraction techniques : $\tau = 5$ (left), 10 (center) and 50 ps (right).

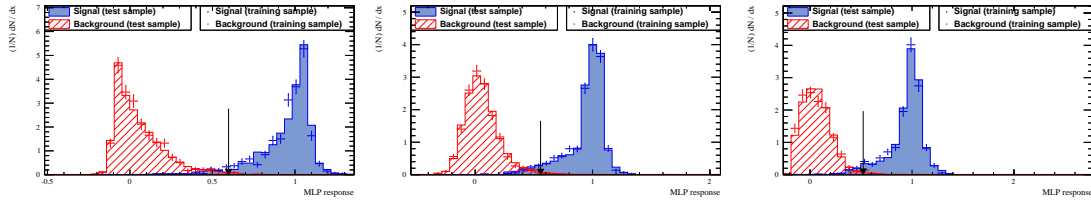


Figure A.3: Like Figure A.2 for $LV98$ models.

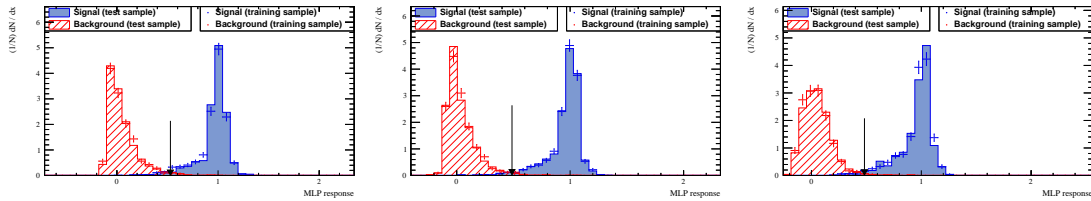


Figure A.4: Like Figure A.2 for $LV198$ models.

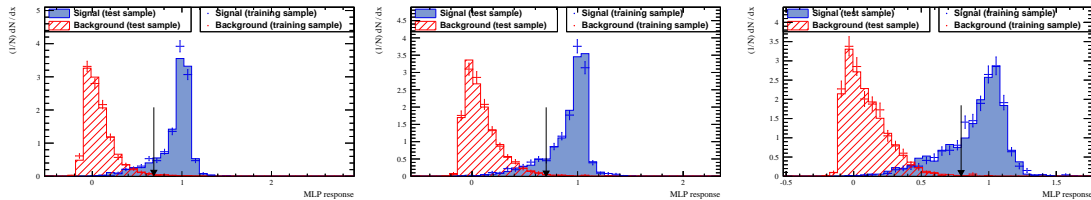


Figure A.5: Overtraining check of the MLP classifier for 2012 data and $LV38$ signal models together with the MLP response selection applied for the signal extraction techniques : $\tau = 5$ (left), 10 (center) and 50 ps (right).

A.3. Multilayer Perceptron response

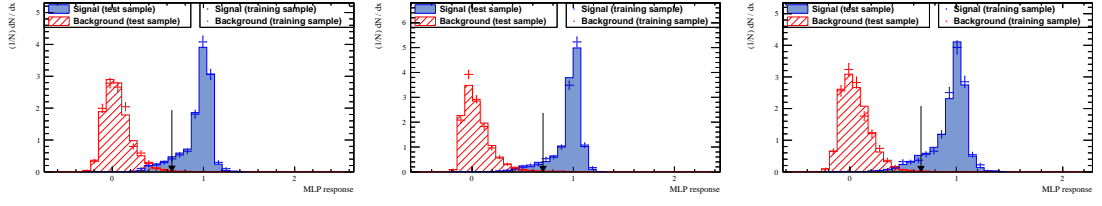


Figure A.6: Like Figure A.5 for LV98 models.

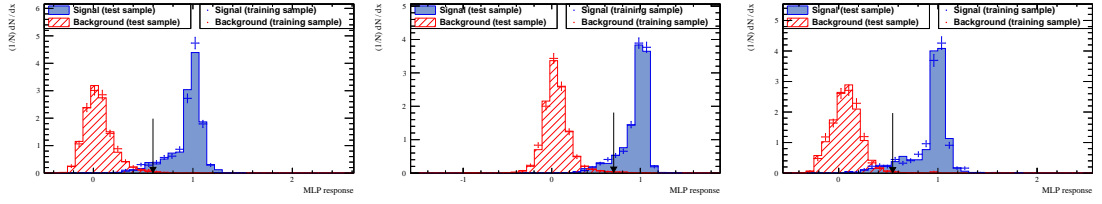


Figure A.7: Like Figure A.5 for LV198 models.

A.4 Neural Network classifier polluted by signal events

The efficiencies as a function of the MLP response for different fraction of signal events added to the background sample (data) at the training stage of the neural network together with the selection applied on each signal models are presented for 2011 and 2012 data analysis.

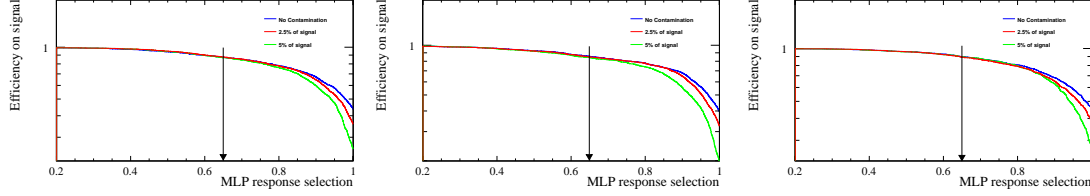


Figure A.8: Signal efficiency as a function of the MLP response selection for different fraction of signal events added to the background for 2011 data and *LV38* signal models : $\tau = 5$ (left), 10 (center) and 50 *ps* (right).

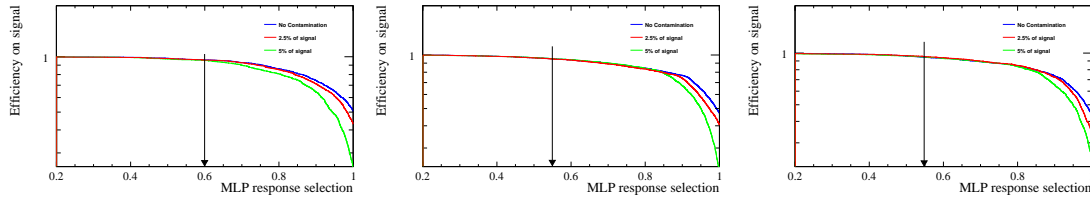


Figure A.9: Like Figure A.8 for *LV98* models.

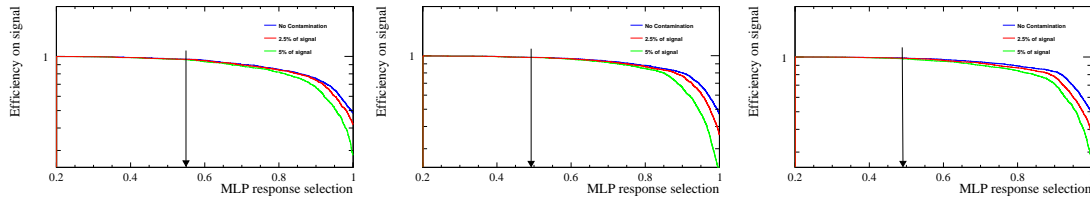


Figure A.10: Like Figure A.8 for *LV198* models.

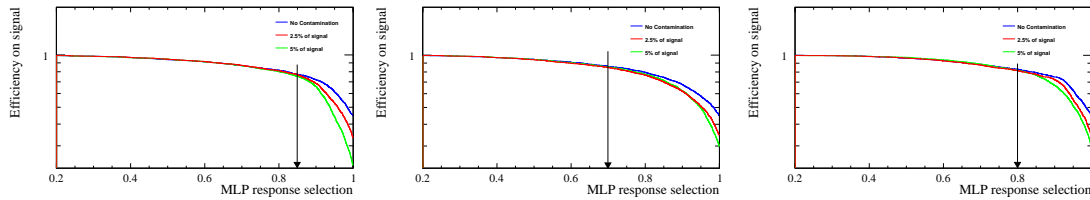


Figure A.11: Signal efficiency as a function of the MLP response selection for different fraction of signal events added to the background for 2012 data and *LV38* signal models : $\tau = 5$ (left), 10 (center) and 50 *ps* (right).

A.4. Neural Network classifier polluted by signal events

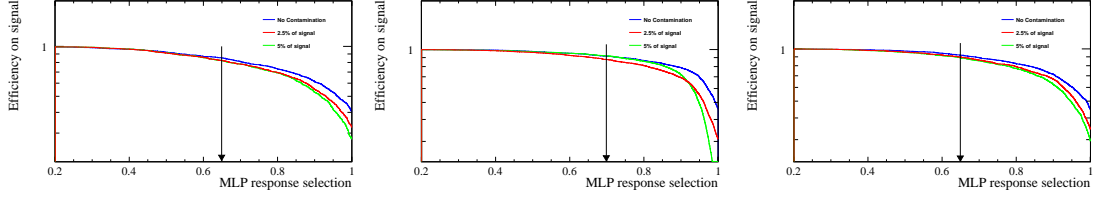


Figure A.12: Like Figure A.11 for *LV98* models.

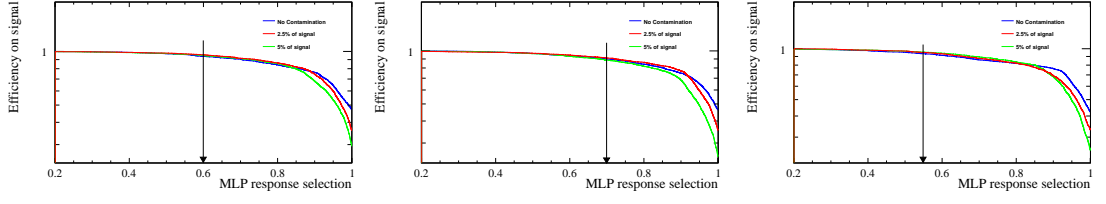


Figure A.13: Like Figure A.11 for *LV198* models.

A.5 Effects of the MLP on m_{LLP} and $1/Isolation$

On figure A.14 and A.15, $PDF(m_{LLP}, 1/Isolation)$ and separately $PDF(m_{LLP})$ and $PDF(1/Isolation)$ are presented for different values of the selection on the neural network response (MLP) (no cut, 0.2, 0.4 and 0.6) for $LV38$ ($\tau = 10$ ps) and 2011 dataset. It shows that the MLP tends to remove events with a small isolation and a low mass which corresponds mainly to the C region where the background is dominant with respect to signal events.

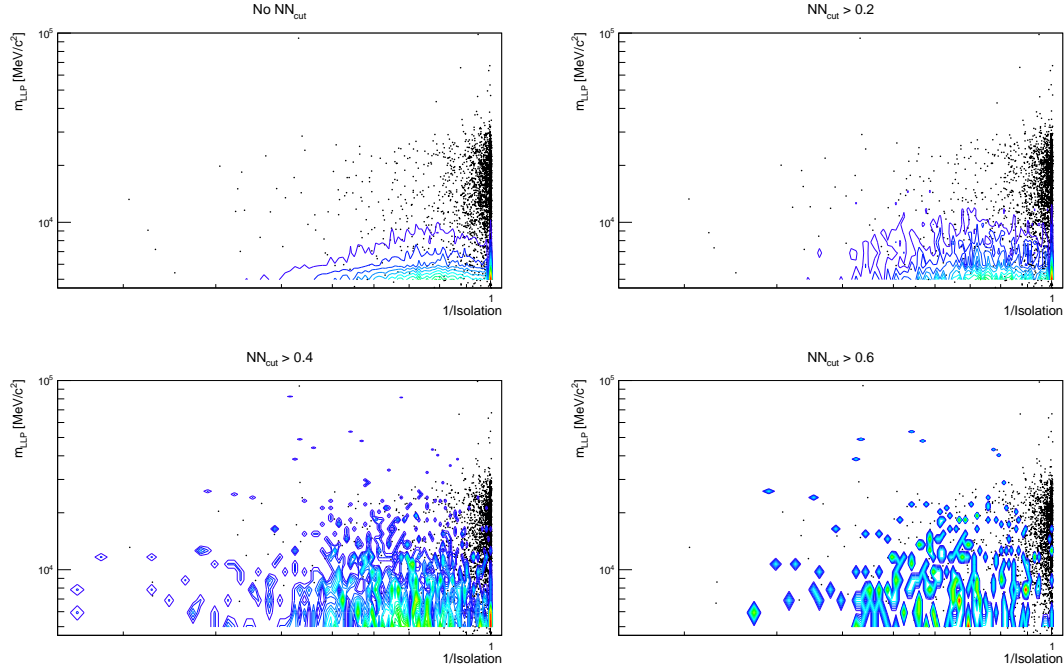


Figure A.14: Effect of NN_{cut} (MLP) on the bi-parametric distribution. The contour define 2011 data distribution in comparison with the signal $LV38$ ($\tau = 10$ ps) as an example (black dots).

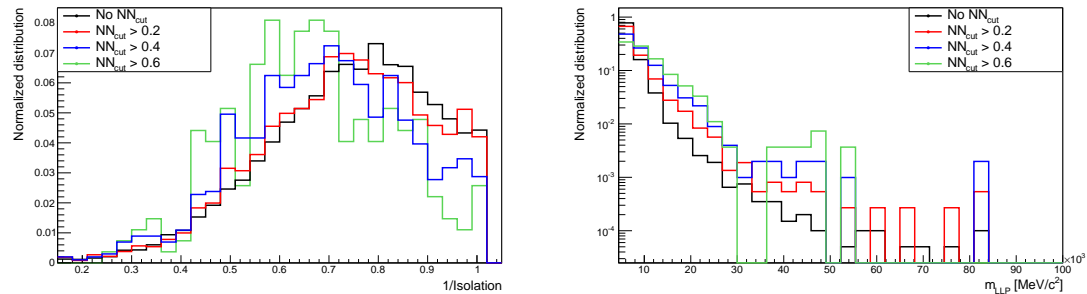


Figure A.15: Effect of NN_{cut} (MLP) on the distribution of the bi-parametric projections for 2011 data and $LV38$ ($\tau = 10$ ps) as an example. Inverse of the isolation (left) and reconstructed mass of the long-lived particle candidate (right).

A.6 Estimation of the effects from for each signal models and datasets

Table A.7: Results of 1000 toy experiments for the 2011 dataset. 200 events of background and 5 events of signal has been generated in the bi-parametric distributions and its projections. "Total" defines the average of the background plus signal events in each region, "signal" correspond to the average of the number of signal events.

Model	\hat{S}_D	\hat{B}_D	N_A	N_B	N_C	N_D
LV38 ($\tau = 5$ ps) (2D,total)	2.58 ± 2.53	3.56 ± 1.26	30.34 ± 5.08	149.31 ± 6.26	19.22 ± 4.18	6.14 ± 2.20
LV38 ($\tau = 5$ ps) (2D,signal)			0.97 ± 0.91	0.86 ± 0.86	1.24 ± 0.95	1.94 ± 1.09
LV38 ($\tau = 5$ ps) (Proj,total)	1.85 ± 2.52	3.86 ± 1.32	31.60 ± 5.27	147.81 ± 6.24	19.89 ± 4.11	5.70 ± 2.15
LV38 ($\tau = 5$ ps) (Proj,signal)			1.12 ± 0.92	0.72 ± 0.75	1.28 ± 0.95	1.88 ± 1.09
LV38 ($\tau = 10$ ps) (2D,total)	2.64 ± 2.92	4.58 ± 1.48	29.00 ± 4.92	144.16 ± 6.48	24.62 ± 4.76	7.22 ± 2.52
LV38 ($\tau = 10$ ps) (2D,signal)			0.94 ± 0.88	0.83 ± 0.84	1.25 ± 0.95	1.98 ± 1.09
LV38 ($\tau = 10$ ps) (Proj,total)	1.96 ± 2.97	4.99 ± 1.58	30.59 ± 5.12	142.25 ± 6.22	25.21 ± 4.69	6.95 ± 2.52
LV38 ($\tau = 10$ ps) (Proj,signal)			1.04 ± 0.91	0.70 ± 0.75	1.32 ± 0.97	1.94 ± 1.10
LV38 ($\tau = 50$ ps) (2D,total)	3.15 ± 2.92	4.12 ± 1.35	26.67 ± 4.79	146.26 ± 6.41	24.79 ± 4.60	7.27 ± 2.58
LV38 ($\tau = 50$ ps) (2D,signal)			0.80 ± 0.80	0.70 ± 0.76	1.61 ± 1.00	1.90 ± 1.06
LV38 ($\tau = 50$ ps) (Proj,total)	2.01 ± 2.82	4.68 ± 1.51	29.02 ± 4.98	143.97 ± 6.58	25.32 ± 4.75	6.68 ± 2.38
LV38 ($\tau = 50$ ps) (Proj,signal)			0.85 ± 0.85	0.65 ± 0.77	1.53 ± 1.04	1.97 ± 1.07
LV98 ($\tau = 5$ ps) (2D,total)	3.72 ± 2.02	2.04 ± 0.86	29.68 ± 4.93	157.62 ± 5.62	11.93 ± 3.31	5.77 ± 1.83
LV98 ($\tau = 5$ ps) (2D,signal)			0.63 ± 0.71	0.40 ± 0.62	0.87 ± 0.80	3.10 ± 1.06
LV98 ($\tau = 5$ ps) (Proj,total)	3.30 ± 2.04	2.19 ± 0.94	31.43 ± 5.14	156.00 ± 5.74	12.08 ± 3.37	5.50 ± 1.81
LV98 ($\tau = 5$ ps) (Proj,signal)			0.82 ± 0.89	0.25 ± 0.49	0.92 ± 0.86	3.00 ± 1.12
LV98 ($\tau = 10$ ps) (2D,total)	3.30 ± 2.40	3.06 ± 1.13	30.51 ± 5.05	151.59 ± 6.27	16.54 ± 3.93	6.36 ± 2.11
LV98 ($\tau = 10$ ps) (2D,signal)			0.66 ± 0.74	0.40 ± 0.60	1.03 ± 0.91	2.92 ± 1.14
LV98 ($\tau = 10$ ps) (Proj,total)	3.11 ± 2.30	3.20 ± 1.17	31.64 ± 5.12	150.49 ± 5.99	16.56 ± 3.88	6.31 ± 1.98
LV98 ($\tau = 10$ ps) (Proj,signal)			0.77 ± 0.81	0.26 ± 0.51	0.99 ± 0.91	2.98 ± 1.13
LV98 ($\tau = 50$ ps) (2D,total)	2.74 ± 2.39	3.57 ± 1.27	31.07 ± 5.33	149.14 ± 6.25	18.49 ± 4.18	6.30 ± 2.02
LV98 ($\tau = 50$ ps) (2D,signal)			0.63 ± 0.73	0.37 ± 0.59	1.06 ± 0.91	2.94 ± 1.08
LV98 ($\tau = 50$ ps) (Proj,total)	2.98 ± 2.47	3.51 ± 1.26	31.98 ± 5.39	148.73 ± 6.58	17.80 ± 4.00	6.49 ± 2.12
LV98 ($\tau = 50$ ps) (Proj,signal)			0.79 ± 0.81	0.27 ± 0.52	1.08 ± 0.95	2.86 ± 1.11
LV198 ($\tau = 5$ ps) (2D,total)	3.54 ± 1.32	0.78 ± 0.39	11.01 ± 3.18	175.47 ± 4.53	14.21 ± 3.58	4.32 ± 1.26
LV198 ($\tau = 5$ ps) (2D,signal)			0.51 ± 0.64	0.39 ± 0.58	1.18 ± 0.98	2.92 ± 1.14
LV198 ($\tau = 5$ ps) (Proj,total)	3.58 ± 1.36	0.82 ± 0.41	11.55 ± 3.16	174.88 ± 4.93	14.17 ± 3.78	4.40 ± 1.29
LV198 ($\tau = 5$ ps) (Proj,signal)			0.59 ± 0.72	0.29 ± 0.52	1.16 ± 0.91	2.96 ± 1.07
LV198 ($\tau = 10$ ps) (2D,total)	3.28 ± 1.36	0.97 ± 0.46	12.85 ± 3.44	173.10 ± 4.59	14.80 ± 3.49	4.25 ± 1.28
LV198 ($\tau = 10$ ps) (2D,signal)			0.60 ± 0.72	0.38 ± 0.60	1.15 ± 0.98	2.88 ± 1.10
LV198 ($\tau = 10$ ps) (Proj,total)	3.48 ± 1.39	0.97 ± 0.46	12.77 ± 3.37	172.77 ± 4.87	15.01 ± 3.56	4.45 ± 1.31
LV198 ($\tau = 10$ ps) (Proj,signal)			0.66 ± 0.73	0.25 ± 0.48	1.15 ± 0.94	2.94 ± 1.06
LV198 ($\tau = 50$ ps) (2D,total)	3.52 ± 1.71	1.48 ± 0.62	14.16 ± 3.61	166.67 ± 5.34	19.17 ± 4.11	5.00 ± 1.59
LV198 ($\tau = 50$ ps) (2D,signal)			0.45 ± 0.62	0.39 ± 0.61	1.29 ± 1.03	2.88 ± 1.11
LV198 ($\tau = 50$ ps) (Proj,total)	3.37 ± 1.69	1.52 ± 0.65	14.63 ± 3.77	166.27 ± 5.28	19.22 ± 4.01	4.88 ± 1.56
LV198 ($\tau = 50$ ps) (Proj,signal)			0.62 ± 0.75	0.28 ± 0.53	1.25 ± 0.98	2.86 ± 1.11

Table A.8: Same as table A.7 for the 2012 dataset.

Model	\hat{S}_D	\hat{B}_D	N_A	N_B	N_C	N_D
LV38 ($\tau = 5$ ps) (2D,total)	4.25 ± 3.36	5.15 ± 1.73	42.81 ± 5.87	135.12 ± 6.97	17.67 ± 3.89	9.40 ± 2.88
LV38 ($\tau = 5$ ps) (2D,signal)			1.17 ± 0.91	0.82 ± 0.81	1.05 ± 0.88	1.96 ± 1.11
LV38 ($\tau = 5$ ps) (Proj,total)	1.80 ± 3.19	5.87 ± 1.90	44.61 ± 5.86	133.61 ± 6.64	19.10 ± 4.03	7.67 ± 2.57
LV38 ($\tau = 5$ ps) (Proj,signal)			1.28 ± 0.97	0.72 ± 0.77	1.12 ± 0.94	1.88 ± 1.05
LV38 ($\tau = 10$ ps) (2D,total)	4.55 ± 3.98	7.24 ± 2.19	43.21 ± 5.85	127.15 ± 6.78	22.84 ± 4.47	11.79 ± 3.32
LV38 ($\tau = 10$ ps) (2D,signal)			1.04 ± 0.91	0.80 ± 0.84	1.16 ± 0.96	2.01 ± 1.10
LV38 ($\tau = 10$ ps) (Proj,total)	2.07 ± 3.90	8.29 ± 2.38	45.40 ± 6.02	124.79 ± 6.96	24.45 ± 4.43	10.36 ± 3.09
LV38 ($\tau = 10$ ps) (Proj,signal)			1.11 ± 0.92	0.67 ± 0.77	1.21 ± 0.95	2.01 ± 1.10
LV38 ($\tau = 50$ ps) (2D,total)	4.22 ± 3.95	7.40 ± 2.19	44.69 ± 5.66	126.23 ± 6.80	22.48 ± 4.30	11.61 ± 3.28
LV38 ($\tau = 50$ ps) (2D,signal)			0.83 ± 0.82	0.73 ± 0.78	1.31 ± 0.99	2.12 ± 1.12
LV38 ($\tau = 50$ ps) (Proj,total)	2.09 ± 4.09	8.67 ± 2.56	47.88 ± 6.07	122.51 ± 6.84	23.85 ± 4.58	10.76 ± 3.19
LV38 ($\tau = 50$ ps) (Proj,signal)			0.97 ± 0.87	0.63 ± 0.76	1.32 ± 0.99	2.08 ± 1.13
LV98 ($\tau = 5$ ps) (2D,total)	3.77 ± 3.00	4.71 ± 1.67	45.11 ± 5.88	136.16 ± 6.65	15.25 ± 3.78	8.48 ± 2.50
LV98 ($\tau = 5$ ps) (2D,signal)			0.95 ± 0.88	0.28 ± 0.51	0.77 ± 0.79	3.00 ± 1.08
LV98 ($\tau = 5$ ps) (Proj,total)	3.11 ± 3.00	5.03 ± 1.75	46.66 ± 6.16	134.63 ± 6.69	15.56 ± 3.74	8.15 ± 2.44
LV98 ($\tau = 5$ ps) (Proj,signal)			0.91 ± 0.86	0.26 ± 0.48	0.78 ± 0.81	3.06 ± 1.04
LV98 ($\tau = 10$ ps) (2D,total)	3.18 ± 2.90	5.12 ± 1.67	41.67 ± 5.85	137.14 ± 6.62	17.89 ± 3.96	8.30 ± 2.37
LV98 ($\tau = 10$ ps) (2D,signal)			0.82 ± 0.85	0.28 ± 0.51	0.75 ± 0.80	3.15 ± 1.11
LV98 ($\tau = 10$ ps) (Proj,total)	3.10 ± 3.03	5.29 ± 1.73	42.36 ± 5.85	136.18 ± 6.86	18.07 ± 4.06	8.39 ± 2.49
LV98 ($\tau = 10$ ps) (Proj,signal)			0.90 ± 0.83	0.21 ± 0.46	0.72 ± 0.79	3.17 ± 1.09
LV98 ($\tau = 50$ ps) (2D,total)	3.24 ± 3.19	5.62 ± 1.83	46.47 ± 5.82	132.54 ± 6.44	17.12 ± 3.83	8.87 ± 2.61
LV98 ($\tau = 50$ ps) (2D,signal)			0.63 ± 0.74	0.41 ± 0.61	0.92 ± 0.83	3.04 ± 1.05
LV98 ($\tau = 50$ ps) (Proj,total)	3.03 ± 3.28	5.77 ± 1.93	47.14 ± 6.10	131.69 ± 6.66	17.37 ± 3.94	8.80 ± 2.65
LV98 ($\tau = 50$ ps) (Proj,signal)			0.79 ± 0.83	0.28 ± 0.50	1.01 ± 0.88	2.91 ± 1.07
LV198 ($\tau = 5$ ps) (2D,total)	3.48 ± 2.02	2.54 ± 0.91	19.11 ± 4.16	157.45 ± 5.62	22.42 ± 4.37	6.02 ± 1.80
LV198 ($\tau = 5$ ps) (2D,signal)			0.44 ± 0.63	0.28 ± 0.53	1.00 ± 0.89	3.28 ± 1.08
LV198 ($\tau = 5$ ps) (Proj,total)	3.34 ± 2.17	2.65 ± 0.93	20.45 ± 4.16	156.62 ± 5.76	21.94 ± 4.28	5.99 ± 1.96
LV198 ($\tau = 5$ ps) (Proj,signal)			0.60 ± 0.69	0.21 ± 0.45	1.04 ± 0.93	3.15 ± 1.07
LV198 ($\tau = 10$ ps) (2D,total)	2.89 ± 1.86	2.32 ± 0.90	15.68 ± 3.96	158.59 ± 5.90	25.51 ± 4.66	5.21 ± 1.63
LV198 ($\tau = 10$ ps) (2D,signal)			0.63 ± 0.72	0.30 ± 0.53	1.07 ± 0.93	3.01 ± 1.10
LV198 ($\tau = 10$ ps) (Proj,total)	3.24 ± 1.95	2.47 ± 0.93	16.79 ± 3.91	157.41 ± 5.85	25.10 ± 4.85	5.70 ± 1.71
LV198 ($\tau = 10$ ps) (Proj,signal)			0.69 ± 0.76	0.25 ± 0.48	1.01 ± 0.85	3.05 ± 1.04
LV198 ($\tau = 50$ ps) (2D,total)	4.13 ± 2.00	1.92 ± 0.77	19.25 ± 4.28	161.92 ± 5.59	17.77 ± 4.04	6.06 ± 1.84
LV198 ($\tau = 50$ ps) (2D,signal)			0.51 ± 0.66	0.28 ± 0.52	1.18 ± 0.94	3.03 ± 1.08
LV198 ($\tau = 50$ ps) (Proj,total)	3.24 ± 1.90	2.19 ± 0.83	21.22 ± 4.29	160.20 ± 5.45	18.15 ± 3.93	5.43 ± 1.71
LV198 ($\tau = 50$ ps) (Proj,signal)			0.64 ± 0.74	0.25 ± 0.51	1.15 ± 0.95	2.97 ± 1.12

A.7 Test of the ABCD method with $b\bar{b}$ MC events at the intermediate selections stage

The optimization for LV signals made with toy MC experiments has been tested with $b\bar{b}$ events at the intermediate stage of the selection where no selection are made on the MLP response. 5 LV38 ($\tau = 10$ ps) events are generated for each experiment plus 200 $b\bar{b}$ background events. In a second test, the same number of signal events are generated per experiment, but the distributions from the data itself is used as background model. In both cases sets of 1000 experiments are generated and the significance computed by varying the boundaries on the

A.7. Test of the ABCD method with $b\bar{b}$ MC events at the intermediate selections stage

(m_{LLP} , $1/\text{Isolation}$) plane. On figure A.16, an example of toy experiment is given for illustration.

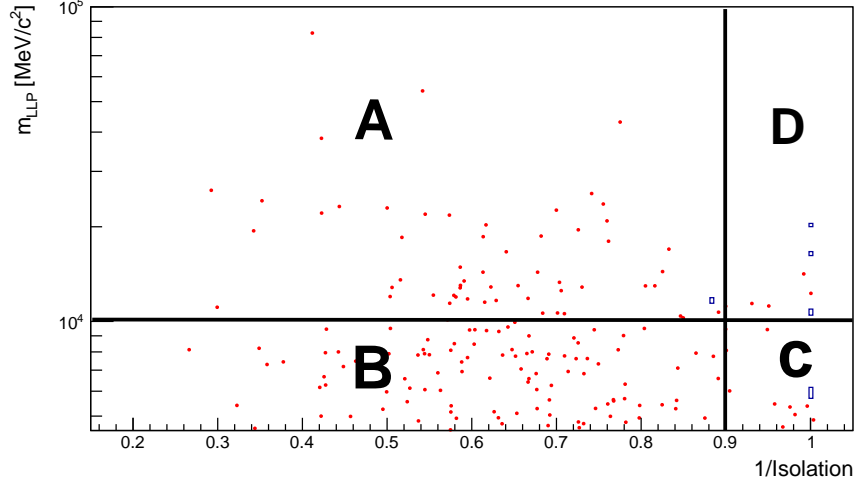


Figure A.16: Example of toy experiment with 200 background events (red) and 5 signal events based on LV38 ($\tau = 10$ ps) (blue boxes). Most of the signal is in the D regions. A, B, and C are the sidebands used to estimate the background in D.

Both tests give about the same result: the best significance values are 1.19 and 1.23 for the first and second test respectively, obtained with boundaries set at $m_{LLP} = 12.5$ GeV/ c^2 and $Iso^{-1} = 0.9$. On the table A.9, the results of the 1000 toy experiments for MC $b\bar{b}$ and 2011 are presented.

With this choice of boundaries, the average number of events expected in D is 2. The two tests give equivalent results: the estimated number of signal events in D is 1.66 ± 2.00 for the $b\bar{b}$ based toys and 2.30 ± 1.96 for the data based toys. A correction can be applied to take into account the presence of signal in the A, B, C region. After this correction the average number of events is 1.83 ± 2.12 and 2.46 ± 2.10 for the two tests, both compatible with the 2 ± 1 events expected in D. It is found that the number of events in each region are very close by comparing the results obtained from the bi-parametric and the projections distributions which indicates a very low correlation level. The bias estimated from the data is $2.51 - 2.30 = 0.21$ with the statistical uncertainty of the same magnitude.

Appendix A. Appendix

Table A.9: Results of 1000 toy experiments for MC events and 2011 data with $m_{LLP} = 12.5 \text{ GeV}/c^2$ and $Iso^{-1} = 0.9$ for 200 events of background and 5 events of signal. "Total" defines the mean of the sum of background and signal events in each region and "signal" correspond to the mean of the number of signal only. "2D" and "Proj" are referring to the toys based on the bi-parametric $PDF(m_{LLP}, 1/Isolation)$ and the two projections $PDF(m_{LLP}) \times PDF(1/Isolation)$ respectively. The errors are RMS.

	\tilde{S}_D	\tilde{B}_D	N_A	N_B	N_C	N_D
MC $b\bar{b}$ (total, 2D)	1.66 ± 2.00	1.40 ± 0.80	7.78 ± 2.76	164.53 ± 6.05	29.63 ± 5.28	3.06 ± 1.20
MC $b\bar{b}$ (signal, 2D)			0.64 ± 0.72	0.90 ± 0.90	1.50 ± 1.08	1.96 ± 1.12
Data (total, 2D)	2.30 ± 1.96	1.06 ± 0.63	5.58 ± 2.25	164.75 ± 5.36	31.31 ± 5.11	3.36 ± 1.32
Data (signal, 2D)			0.61 ± 0.77	0.75 ± 0.75	1.67 ± 1.09	1.97 ± 1.11
MC $b\bar{b}$ (total, Proj)	2.37 ± 1.99	1.07 ± 0.64	6.16 ± 2.43	164.41 ± 5.18	28.98 ± 4.92	3.44 ± 1.36
MC $b\bar{b}$ (signal, Proj)			0.74 ± 0.79	0.66 ± 0.78	1.68 ± 1.06	1.90 ± 1.12
Data (total, Proj)	2.51 ± 1.88	0.96 ± 0.57	5.07 ± 2.05	164.97 ± 5.38	31.55 ± 4.98	3.47 ± 1.30
Data (signal, Proj)			0.74 ± 0.74	0.65 ± 0.76	1.57 ± 1.00	2.03 ± 1.08

Bibliography

- [1] G. Bellini, L. Ludhova, G. Ranucci, and F.L. Villante. Neutrino oscillations. *Adv.High Energy Phys.*, 2014:191960, 2014.
- [2] Peter W. Graham, Surjeet Rajendran, and Prashant Saraswat. Supersymmetric Crevices: Missing Signatures of RPV at the LHC. 2014.
- [3] M. Adinolfi, G. Aglieri Rinella, E. Albrecht, T. Bellunato, S. Benson, T. Blake, et al. Performance of the LHCb RICH detector at the LHC. *European Physical Journal C*, 73:2431, May 2013.
- [4] Jr. Alves, A.A., L. Anderlini, M. Anelli, R. Antunes Nobrega, G. Auriemma, et al. Performance of the LHCb muon system. *JINST*, 8:P02022, 2013.
- [5] A Bay, V Coco, P David, V Heijne, W Hulsbergen, M Martinelli, B Muster, J Rouvinet, and S Tourneur. Search for exotic massive long-lived particles in 0.67 fb^{-1} at LHCb. (LHCb-ANA-2014-006).
- [6] J Rouvinet, A Bay, V Coco, P David, V Heijne, W Hulsbergen, M Martinelli, B Muster, and S Tourneur. Search for Higgs-like bosons decaying into a pair of long-lived exotic particles in 0.91 fb^{-1} at $\sqrt{s} = 7 \text{ TeV}$. (LHCb-ANA-2014-058).
- [7] Thi Viet Nga La, Bay Aurelio, and Minh Tâm Tran. A search for heavy long-lived staus in the LHCb detector in proton-proton collisions at $\sqrt{s} = 7$ and $\sqrt{s} = 8 \text{ TeV}$. (LHCb-ANA-2014-006).
- [8] Paul Langacker. Introduction to the Standard Model and Electroweak Physics. pages 3–48, 2009.
- [9] Sean M. Carroll. Lecture notes on general relativity. 1997.
- [10] J. Beringer et al. (*Particle Data Group*). *Phys. Rev. D* 86, 010001, 2012.
- [11] M. Kobayashi and T. Maskawa. *Prog. Theor. Phys.* 49, 652. (1973).
- [12] N. Cabibbo. *Phys. Rev. Lett.* 10, 531. (1963).
- [13] M. Gomez-Bock, M. Mondragon, M. Muhlleitner, M. Spira, and P.M. Zerwas. Concepts of Electroweak Symmetry Breaking and Higgs Physics. pages 177–238, 2007.

Bibliography

- [14] Georges Aad et al. Observation of a new particle in the search for the Standard Model Higgs boson with the ATLAS detector at the LHC. *Phys.Lett.*, B716:1–29, 2012.
- [15] Nima Arkani-Hamed, Savas Dimopoulos, and G.R. Dvali. The Hierarchy problem and new dimensions at a millimeter. *Phys.Lett.*, B429:263–272, 1998.
- [16] Katherine Garrett and Gintaras Duda. Dark Matter: A Primer. *Adv.Astron.*, 2011:968283, 2011.
- [17] Werner Bernreuther. CP violation and baryogenesis. *Lect.Notes Phys.*, 591:237–293, 2002.
- [18] Michael J. Mortonson, David H. Weinberg, and Martin White. Dark Energy: A Short Review. 2013.
- [19] Ian J.R. Aitchison. Supersymmetry and the MSSM: An Elementary introduction. 2005.
- [20] G.F. Giudice and R. Rattazzi. Theories with gauge mediated supersymmetry breaking. *Phys.Rept.*, 322:419–499, 1999.
- [21] R. Barbier, C. Berat, M. Besancon, M. Chemtob, A. Deandrea, et al. R-parity violating supersymmetry. *Phys.Rept.*, 420:1–202, 2005.
- [22] A.G. Akeroyd, Eung Jin Chun, M.A. Diaz, and Dong-Won Jung. Neutrino masses, baryogenesis and bilinear R parity violation. *Phys.Lett.*, B582:64–72, 2004.
- [23] B.C. Allanach, A. Dedes, and H.K. Dreiner. R parity violating minimal supergravity model. *Phys.Rev.*, D69:115002, 2004.
- [24] Peter W. Graham, David E. Kaplan, Surjeet Rajendran, and Prashant Saraswat. Displaced Supersymmetry. *JHEP*, 1207:149, 2012.
- [25] F. de Campos, O.J.P. Eboli, M.B. Magro, and D. Restrepo. Searching supersymmetry at the LHCb with displaced vertices. *Phys.Rev.*, D79:055008, 2009.
- [26] The ATLAS Collaboration. Search for long-lived, heavy particles in final states with a muon and a multi-track displaced vertex in proton-proton collisions at $\sqrt{s} = 8 \text{ TeV}$ with the ATLAS detector. *ATLAS-CONF-2013-092*.
- [27] Serguei Chatrchyan et al. Search in leptonic channels for heavy resonances decaying to long-lived neutral particles. *JHEP*, 1302:085, 2013.
- [28] V.M. Abazov et al. Search for neutral, long-lived particles decaying into two muons in $p\bar{p}$ collisions at $\sqrt{s} = 1.96\text{-TeV}$. *Phys.Rev.Lett.*, 97:161802, 2006.
- [29] M et al. Banner. Observation of single isolated electrons of high transverse momentum in events with missing transverse energy at the CERN $\bar{p}p$ collider. *Phys. Lett. B*, 122(CERN-EP-83-25):476–485. 15 p, Feb 1983.

-
- [30] Geoffrey T J et al. Arnison. Experimental observation of isolated large transverse energy electrons with associated missing energy at $\sqrt{s} = 540 \text{ GeV}$. *Phys. Lett. B*, 122(CERN-EP-83-13):103–116. 31 p, Jan 1983.
 - [31] Oliver Sim Bruening, Paul Collier, P Lebrun, Stephen Myers, Ranko Ostojic, John Poole, and Paul Proudlock. *LHC Design Report*. CERN, Geneva, 2004.
 - [32] V. Berardi et al. TOTEM: Technical design report. Total cross section, elastic scattering and diffraction dissociation at the Large Hadron Collider at CERN. 2004.
 - [33] O Adriani, L Bonechi, M Bongi, R D’Alessandro, D A Faus, M Haguenauer, Y Itow, K Kasahara, K Masuda, Y Matsubara, H Menjo, Y Muraki, P Papini, T Sako, T Tamura, S Torii, A Tricomi, W C Turner, J Velasco, and K Yoshida. *LHCf experiment: Technical Design Report*. Technical Design Report LHCf. CERN, Geneva, 2006.
 - [34] G. Aad et al. The ATLAS Experiment at the CERN Large Hadron Collider. *JINST*, 3:S08003, 2008.
 - [35] S. Chatrchyan et al. The CMS experiment at the CERN LHC. *JINST*, 3:S08004, 2008.
 - [36] K. Aamodt et al. The ALICE experiment at the CERN LHC. *JINST*, 3:S08002, 2008.
 - [37] A. Beuret, A. Blas, J. Borburgh, H. Burkhardt, C. Carli, et al. The LHC Lead Ion Injector Chain. 2004.
 - [38] The LHCb Collaboration. The lhcb detector at the lhcb. *Journal of Instrumentation*, 3(08):S08005, 2008.
 - [39] R. Aaij, J. Albrecht, F. Alessio, S. Amato, E. Aslanides, I. Belyaev, et al. The LHCb trigger and its performance in 2011. *Journal of Instrumentation*, 8:4022P, April 2013.
 - [40] G. Barrand, I. Belyaev, P. Binko, M. Cattaneo, R. Chytrcek, et al. GAUDI - A software architecture and framework for building HEP data processing applications. *Comput.Phys.Commun.*, 140:45–55, 2001.
 - [41] Measurement of the forward w boson cross-section in pp collisions at $\sqrt{s} = 7 \text{ tev}$. (LHCb-CONF-2014-002).
 - [42] R. Aaij et al. Measurement of J/ψ production in pp collisions at $\sqrt{s} = 7 \text{ TeV}$. *Eur. Phys. J.*, C71:1645, 2011.
 - [43] S Bifani. Measurement of the W production cross-section in pp collisions at $\sqrt{s} = 7 \text{ TeV}$ with the 2011 data. Aug 2014. Linked to LHCb-PAPER-2014-033.
 - [44] P Kucharczyk, R Morawski, and M Witek. Updated Primary Vertex Reconstruction. (Tech. Rep. LHCb-INT-2012-006. CERN-LHCb-INT-2012-006, CERN, Geneva, Feb, 2012).

Bibliography

- [45] A. Hoecker, P. Speckmayer, J. Stelzer, J. Therhaag, E. von Toerne, H. Voss, M. Backes, T. Carli, O. Cohen, A. Christov, D. Dannheim, K. Danielowski, S. Henrot-Versille, M. Jachowski, K. Kraszewski, A. Krasznahorkay, Jr., M. Kruk, Y. Mahalalel, R. Ospanov, X. Prudent, A. Robert, D. Schouten, F. Tegenfeldt, A. Voigt, K. Voss, M. Wolter, and A. Zemla. TMVA - Toolkit for Multivariate Data Analysis. *ArXiv Physics e-prints*, March 2007.
- [46] W. Verkerke and D. Kirkby. The RooFit toolkit for data modeling. *ArXiv Physics e-prints*, June 2003.
- [47] J. Alwall, R. Frederix, S. Frixione, V. Hirschi, F. Maltoni, et al. The automated computation of tree-level and next-to-leading order differential cross sections, and their matching to parton shower simulations. *JHEP*, 1407:079, 2014.
- [48] N. Chiapolini S.Farry. A measurement of high- p_t muon reconstruction efficiencies in 2011 and 2012 data. (LHCb-INT-2014-030).
- [49] Roel Aaij et al. Measurement of the track reconstruction efficiency at LHCb. 2014.
- [50] M. Pivk and F. R. Le Diberder. Plots: A statistical tool to unfold data distributions. *Nuclear Instruments and Methods in Physics Research A*, 555:356–369, December 2005.
- [51] Y Amhis, G Cowan, F Dordei, S Hansmann-Menzemer, R Maerki, and T Nikodem. b-hadrons absolute lifetime measurements. Feb 2014. Linked to LHCb-PAPER-2013-065.
- [52] Roel Aaij et al. Precision luminosity measurements at LHCb. 2014.
- [53] Alexander L. Read. Presentation of search results: The CL(s) technique. *J.Phys.*, G28:2693–2704, 2002.
- [54] Lorenzo Moneta, Kevin Belasco, Kyle S. Cranmer, S. Kreiss, Alfio Lazzaro, et al. The RooStats Project. *PoS*, ACAT2010:057, 2010.

Acronyms

BP Back Propagation

CP Charge Parity

DOCA Distance of Closest Approach

DV Displaced Vertex

ECAL Electromagnetic Calorimeter

EWSB Electro-Weak Symmetry Breaking

GUT Grand Unified Theory

HCAL Hadronic Calorimeter

HLT High-Level Trigger

IP Impact Parameter

LLP Long-Lived Particles

LSP Lightest Superpartner

LV Lepton Violation

L0 Level-0 Trigger

MC Monte Carlo

mGMSB Minimal Gauge-Mediated Supersymmetry Breaking

MLP Multilayer Perceptron

mSUGRA Minimal Supergravity

MSSM Minimal Supersymmetric Standard Model

MV Matter Veto

NLO Next-to-leading Order

Appendix A. Acronyms

POCA Point of Closest Approach

PV Primary Vertex

QCD Quantum chromodynamics

RMS Root Mean Square

RPV R-parity violation

RV Reconstructed Vertices

SM Standard Model

SUSY Supersymmetry

VELO VERTex LOcator

Bastien Muster

27 years old, swiss citizen
Chemin de la Forêt 4b
1018 Lausanne, VD

☎ +41 76 570 87 93

✉ bastien.muster@gmail.com



Experienced in data analysis, statistics, programming and data mining, I am a quick learner with a strong adaptability and team spirit looking for a position as analyst.

EXPERIENCE AND PROJECTS

Ph. D. Thesis – EPFL and CERN

2011-2015

- **Large data set analysis** with complex **statistical** and **computational** methods to determine signal significance and background estimation, and to set confidence level on theoretical predictions
- **Algorithms development** for the **modeling** of physical processes using Monte-Carlo **numerical simulations**
- **Data mining** with artificial neural networks and boosted decision trees
- **Reporting** of results in various documents and conferences

Junior and Senior teaching assistant – EPFL

2007-2015

- Teaching duties covering a large range of topics and practical works in nuclear physics at Bachelor and Master levels

EDUCATION

Ph. D. In physics (Docteur ès sciences) (March 2015)

EPFL and CERN 2011-2015

- **Thesis:** *Search for exotic massive long-lived particles decaying semileptonically in the LHCb detector*

Master of Science in Physics (Dipl. EPF)

EPFL 2009-2011

- Numerical simulation, statistical analysis using Matlab, nuclear physics, plasma physics

Bachelor of Science in Physics

EPFL 2006-2009

- Mathematics, general physics, programming, statistics

LANGUAGES AND IT SKILLS

Languages

French: mother tongue

English: full professional proficiency, worked 5+ years in english (C1)

German: good knowledge (B2)

Computer

Programming: Matlab, SQL, C++/C#, Python, Bash, Perl, Mathematica

Operating systems: Windows, MacOSX and Unix/Linux

Software: Microsoft Office, LaTeX, ROOT (CERN version of R)

MISCELLANEOUS

Rowing (national level), tennis, ice hockey, floorball, economic literature, new technologies

